OPTICAL PROPERTIES OF ZINC OXIDE NANOTIPS AND THEIR DEVICE APPLICATIONS

by

JIAN ZHONG

A Dissertation submitted to the

Graduate School-New Brunswick

Rutgers, The State University of New Jersey

in partial fulfillment of the requirements

for the degree of

Doctor of Philosophy

Graduate Program in Electrical and Computer Engineering

Written under the direction of

Professor Yicheng Lu

And approved by

_____

_____

_____

_____

_____

New Brunswick, New Jersey

October, 2007

ABSTRACT OF THE DISSERTATION

OPTICAL PROPERTIES OF ZINC OXIDE NANOTIPS AND THEIR DEVICE APPLICATIONS

by JIAN ZHONG

Dissertation Director:

Professor Yicheng Lu

Zinc oxide (ZnO) nanostructures are emerging as the key building blocks for nanoscale optoelectronic and electronic devices. ZnO has a large exciton binding energy (~ 60 meV), which makes its nanotips ideal for studying excitonic emissions in one-dimensional systems even at room temperature. ZnO nanowires show a strong exciton-polariton interaction, promising for fabricating UV nanolasers. The large and fast photoconductivity in high quality ZnO is suitable for making UV photodetectors. ZnO nanotips can be grown on various substrates, including glass, Si, and GaN, at low growth temperature (~ 400°C) by metal-organic chemical vapor deposition *(*MOCVD) that provides the potential of the integration of ZnO nanotips with Si based microelectronics and GaN based optoelectronics devices. To date, most of the research has been focused either on ZnO films, or on “pick-and-place” manipulation of randomly dispersed ZnO nanowires to study their physical properties.

In this dissertation work *in-situ* n-type doping of ZnO nanotips during MOCVD is studied, including the doping effects on optical properties and electrical conductivity. Nanoscale tunneling current-voltage characteristics of the ZnO nanotips show the conductivity enhancement due to Ga doping at the proper range of doping concentration. At low or moderate doping levels, the increase in photoluminescence (PL) intensity from Ga doping is attributed to the increase of Ga donor related impurity emission.

The excitonic emissions of ZnO nanotips are investigated using temperature-dependent PL spectroscopy. The sharp free exciton and donor-bound exciton peaks are observed at 4.4K, confirming high optical quality of the ZnO nanotips. Free exciton emission dominates at temperatures above 50K. The thermal dissociation of these bound excitons forms free excitons and neutral donors. Temperature-dependent free A exciton peak emission is fitted to the Varshni's equation to study the variation of energy bandgap versus temperature.

A prototype of ZnO nanotips/GaN light emitting devices has been demonstrated using an n-ZnO nanotips/p-GaN heterostructure. The electroluminescence with a peak wavelength of 406nm is primarily due to radiative recombination from electron injection from n-type ZnO nanotips into p-type GaN. A novel integrated ZnO nanotips/GaN LED has been fabricated for enhanced light emission efficiency. A Ga-doped ZnO transparent conductive oxide (GZO) film and ZnO nanotips are sequentially grown on top of a GaN LED, serving as the transparent electrode and the light extraction layer, respectively. Compared with the conventional Ni/Au p-metal LED, light output power from the ZnO nanotips/GZO/GaN LED is improved by 1.7 times. The enhanced light extraction is attributed to the increased light scattering and transmission in the ZnO/GaN multilayer.

Dedicated to

my family:

Mom, Dad, Yong & Kang

ACKNOWLEDGEMENTS

I would like to express my sincere gratitude to my advisor, Prof. Yicheng Lu. Only with his insight inspiration, encouragement, and invaluable guidance, I could have successfully completed my research and thesis. He is also a great mentor for the buildup of my future professional career. I learn from him not only knowledge in science and technology, but also the merits as a scientific researcher and faith in the life.

I would like to greatly thank my thesis committee: Prof. S. McAfee, Prof. Wei Jiang, Prof. Kuang Sheng, Dr. H. Shen, and Dr. H. M. Ng, for devoting their valuable time and expertise in reviewing the dissertation. I thank Dr. H. M. Ng, for providing me with the opportunity to work in Bell Laboratories, Murray Hill, NJ, and conduct PL characterizations. His constant help on PL characterizations and data analysis for last five years is invaluable. I thank Dr. H. Shen, for his guidance and help throughout my Ph. D. study on many optical topics, such as optical measurement setup, and providing light extraction analysis and time-resolved PL measurement. I feel lucky to have the opportunities to work with Dr. Shen and Dr. Ng, whom I also view as good mentors of mine. I thank Dr. K. P. Cheung for many valuable technical discussions. Dr. Mackie at Army Research Lab helped me in the light scattering analysis.

I would like to thank the people in Prof. Lu's research group who have helped me during the past years: Dr. Haifeng Sheng, Dr. Sriram Muthukumar, Dr. Pan Wu, Dr. Yimin Chen, Gaurav Saraf, Hanhong Chen, and Jun Zhu. It is a pleasure to work in a team. I also thank our collaborators Dr. C. K. Choi and Dr. J. J. Song at ZN Technology, and Dr. D. Lee

and Dr. E. A. Armour at Veeco Turbodisk Inc. Financial supports from NSF, US Army, and AFOSR are highly appreciated.

TABLE OF CONTENTS

ABSTRACT ii

Acknowledgements v

Table of Contents vii

List of Illustrations x

List of Tables xvi

Chapter 1. Introduction 1

1.1. Motivation 1

1.2. Scope of Work 4

1.3. Organization of Dissertation 5

Chapter 2. Technical Background 6

2.1. ZnO Nanostructures 6

2.2. Optical Properties of ZnO Nanostructures 10

2.2.1 Intrinsic Optical Transitions 11

2.2.2 Extrinsic Optical Transitions 17

2.2.3 Photoluminescence of ZnO Nanostructures 19

2.3. ZnO Nanostructure-based Devices 22

2.4. Summary 25

Chapter 3. Properties of Ga-doped ZnO Nanotips 26

3.1. MOCVD Growth and Characterizations of ZnO Nanotips 27

3.1.1 ZnO Nanotips on Glass 28

3.1.2 ZnO Nanotips on Si 33

3.1.3 ZnO Nanotips on GaN 35
3.2. *In-situ* Ga Doping 42
3.2.1 Growth and Structural Characterizations 42
3.2.2 Optical Characterizations 45
3.2.3 Electrical Characterization 52
3.3. Summary 54
Chapter 4. Temperature Dependent Photoluminescence Studies of ZnO Nanotips 55
4.1 Temperature Dependent Steady-state Photoluminescence 55
4.2 Time-resolved Photoluminescence 66
4.3 Summary 73
Chapter 5. Vertical n-ZnO Nanotips/p-GaN Heterojunction Light Emitting Diodes 74
5.1 Introduction 74
5.2 Processing Development Based on n-ZnO Nanotips/p-Si Heterostructure 76
5.3 Hybrid n-ZnO Nanotips/p-GaN Heterojunction Light Emitting Diode 88
5.4 Summary 93
Chapter 6. Integration of ZnO Nanotips and GaN Light Emitting Diodes for Enhanced Emission Efficiency 102
6.1 Introduction 102
6.2 Integrated ZnO Nanotips/GZO/GaN LED 103

6.3 Light Extraction Analysis 106

6.4 Summary 110

Chapter 7. Conclusions and Future Work 120

7.1 Conclusions 120

7.2 Suggestions for Future Work 121

References 124

Curriculum Vita 133

LIST OF ILLUSTRATIONS

Figure 2.1.Splitting of the valence band in hexagonal ZnO by crystal-field splitting and spin-orbit coupling……13

Figure 2.2. Band structure and symmetries of hexagonal ZnO…….. 14

Figure 3.1. FESEM image of ZnO nanotips grown on glass……...29

Figure 3.2. XRD data of ZnO nanotips grown on glass……...30

Figure 3.3. (a) Room temperature and (b) 77K PL spectra of undoped ZnO nanotips grown on glass. Black curve is the measurement result; red curve is the least-square curve fitting result based on the Lorentzian line shape. Green curves show individual Lorentzian peaks…….....32

Figure 3.4. FESEM image of ZnO nanotips grown on Si substrate……34

Figure 3.5. XRD pattern of ZnO nanotips grown on Si substrate……34

Figure 3.6. (a) Room temperature and (b) 77K PL spectra of ZnO nanotips grown on Si…….....36

Figure 3.7. FESEM image of ZnO nanotips grown on an epitaxial GaN/c-sapphire substrate. Inset is a high resolution TEM image of a single crystalline ZnO nanotip showing lattice fringes. The c-axis of ZnO is aligned normal to the substrate surface, along the vertical direction…….....39

Figure 3.8. XRD patterns of (a) θ-2θ scan of ZnO nanotips on an epitaxial GaN/c-sapphire substrate; (b) in-plane φ scan carried out

along {10-13} family of planes for ZnO……40

Figure 3.9. (a) Room temperature and (b) 77K PL spectra of
ZnO nanotips grown on GaN…….41

Figure 3.10. (a) Measured resistivity of Ga-doped epitaxial ZnO films
versus Ga/Zn mole ratios. FESEM images of Ga-doped
ZnO nanotips grown on fused silica substrate
(b) cross-sectional view, and (c) top view…….....43

Figure 3.11. (a) Selected area diffraction pattern of a single Ga-doped
ZnO nanotip along the $[2\bar{1}\bar{1}0]$ zone axis; (b) an image
of a single crystalline tip from high-resolution
transmission electron microscope (HRTEM); and
(c) dark field TEM image of a single Ga-doped ZnO nanotip.……..44

Figure 3.12. (a) Room temperature PL spectra of undoped and Ga-doped
ZnO nanotips. (b) 77K PL spectra of undoped and Ga-doped
ZnO nanotips. Curve 1 is for the undoped ZnO nanotips with
a reference resistivity, ρ_{ref}, of 40 Ωcm, curves 2, 3 and 4
correspond to Ga-doped ZnO nanotips with ρ_{ref} of 0.58 Ωcm,
4.0×10^{-3} Ωcm and 3.0×10^{-3} Ωcm, respectively……..46

Figure 3.13. Room temperature normalized photoluminescence (left side)
and absorption spectra (right side) of Ga doped ZnO nanotips.
Curves 1, 2 and 3 are Ga-doped ZnO nanotips with ρ_{ref} of
0.58 Ωcm, 4.0×10^{-3} Ωcm and 3.0×10^{-3} Ωcm, respectively……49

Figure 3.14. Current-voltage spectra for the undoped and Ga-doped ZnO

nanotips, where curves 1, 2, and 3 correspond to the spectra of undoped and Ga-doped ZnO nanotips with a reference resistivity of 40 Ωcm (undoped), 0.58 Ωcm (Ga-doped), 4.0×10^{-3} Ωcm (Ga-doped), respectively……53

Figure 4.1. Schematic diagram of a UV temperature dependent PL setup…….....57

Figure 4.2. PL spectrum of ZnO nanotips measured at 4.4K in logarithmic scale. The free exciton emission is clearly seen at 3.380 eV (X_A). Two sharp bound exciton emissions are observed at 3.369 eV (D^0X1) and 3.364 eV (D^0X2), respectively……58

Figure 4.3. Temperature dependent PL spectra of ZnO nanotips. The PL intensity of each curve is plotted in logarithmic scale……...60

Figure 4.4. Arrhenius plots of PL intensities as a function of inverse temperature for D^0X1, D^0X2, and X_A emissions. The solid lines show the curve fitting results from Eq. (4.3)…….....64

Figure 4.5. Plot of PL peak position of free A excitonic emission (X_A) as a function of temperature. The solid line is the curve fitting result according to Eq. (4.7)…….69

Figure 4.6. Plot of free and bound exciton peak position versus temperature ……70

Figure 4.7. Relative internal quantum efficiency versus temperature, assuming internal quantum efficiency is 100% at 6 K……...71

Figure 4.8. (a) Room temperature time resolved photoluminescence spectrum of ZnO nanotips grown on GaN. The red curve in (a) is the instrumental response function (IRF) of the TRPL system.

The red curve in (b) shows the curve fitting result based on
a biexponential decay function……..72
Figure 5.1. Schematic diagram of idea atomic arrangement at
the ZnO/GaN interface…….....75
Figure 5.2. X-ray photoelectron spectroscopy (XPS) spectra of ZnO
nanotips/Si interface (sample B2). With HF surface treatment
and minimized oxygen pre-exposure, sample B2 has minimized
interfacial SiO_2 thickness……...82
Figure 5.3. Schematic diagram of a hybrid n-ZnO nanotips/p-Si
heterojunction p-n diode……83
Figure 5.4. I-V characteristics of Al contact to (a) p-Si
and (b) undoped ZnO nanotips……..84
Figure 5.5. Top view of an n-ZnO nanotips/p-Si heterojunction diode under
an optical microscope……85
Figure 5.6. I-V characteristic of an n-ZnO nanotips/p-Si heterojunction diode
with minimized SiO_2 layer thickness
at the ZnO/Si interface……...86
Figure 5.7. Energy band diagram of n-ZnO nanotips/p-Si heterostructure
in an idea case without considering spontaneous and piezoelectric
polarizations at the interface…..….....87
Figure 5.8. Schematic diagram of an n-ZnO nanotips/p-GaN heterojunction LED……94
Figure 5.9. Room temperature PL spectra of p-GaN (black curve) and
ZnO nanotips (red curve)……...95

Figure 5.10. Top view of an n-ZnO nanotips/p-GaN heterostructure diode under an optical microscope……..96
Figure 5.11. I-V characteristics of Ni/Au contact to p-GaN……97
Figure 5.12. I-V characteristic of an n-ZnO nanotips/p-GaN heterostructure…….....98
Figure 5.13. Blue light emission from an n-ZnO nanotips/p-GaN heterojunction LED under forward current injection…….99
Figure 5.14. Electroluminescence spectra of an n-ZnO nanotips/p-GaN heterostructure light emitting diode under different forward injection currents……100
Figure 5.15. Energy band diagram of n-ZnO nanotips/p-GaN heterostructure in an idea case without considering spontaneous and piezoelectric polarizations at the interface……101
Figure 6.1. Schematic cross-sectional diagram of an integrated ZnO nanotips/GZO/GaN LED…….....111
Figure 6.2. FESEM image of ZnO nanotips/GZO/GaN (perspective view)……..112
Figure 6.3. FESEM image of ZnO nanotips/GZO/GaN (top view)……...113
Figure 6.4. XRD θ-2θ scan of ZnO nanotips grown on a GZO/GaN/c-Al_2O_3 …….....114
Figure 6.5. Room temperature PL spectrum of ZnO nanotips/GZO/GaN…….....115
Figure 6.6. Light output power versus forward injection current for Ni/Au and ZnO nanotips/GZO/GaN LED; inset is EL spectra of Ni/Au p-contact GaN LED and ZnO nanotips/GZO/GaN LED at a forward current of 20mA……..116

Figure 6.7. Two-dimensional Fourier transformation of top view of ZnO nanotips grown on a GZO/GaN template (shown in figure 6.3)……..117

Figure 6.8. (a) Effective refractive index for ZnO nanotips/GZO/GaN LED structure, assuming a uniformly distributed nanotip layer; (b) illustration of the variation of effective refractive index in a randomly distributed ZnO nanotips layer 50nm away from the interface; (c) photon trajectories in a ZnO nanotips structure. Light extraction is enhanced by surface roughening (not shown) and scattering events caused by non-uniform dielectric……..118

Figure 6.9. Simulated angular distribution of transmitted light with ZnO nanotips on top of GaN. For comparison, optical transmission of a standard GaN layer without top ZnO nanotips layer is also shown in red curve.……..119

LIST OF TABLES

Table 2.1 Band structure related properties of wurtzite ZnO…….....15

Table 2.2 Summary of intrinsic exciton transitions in bulk ZnO……17

Table 2.3. Summary of bound exciton transitions in bulk ZnO……...19

Table 3.1 FWHM of room temperature PL spectra for Ga-doped ZnO nanotips at different doping levels……...50

Table 5.1 Crystal structure and lattice parameters of ZnO, GaN, and sapphire……..74

Table 5.2 Peak atomic percentage of SiO_2 at the ZnO/Si interface by XPS depth profile……...78

Chapter 1. Introduction

1.1 Motivation

Zinc oxide (ZnO) is a wide bandgap semiconductor that is currently undergoing a renaissance because of its many exciting properties. The earliest work on ZnO can be dated back to 1930's, particularly optical characterizations in 1950s and 60s [1-3]. Recently, several physical characteristics and device-related properties of ZnO have been explored, showing that ZnO provide a potentially superior material for the optoelectronic and microelectronic devices. ZnO has the following advantages: [4] (1) a 60-meV exciton binding energy for more efficient optical emission and detection (much higher than 25 meV of GaN, 4 meV of GaAs), which is 2.4 times the thermal energy at room temperature; (2) a commercially available native substrate; (3) better radiation resistance (one order higher than that of GaN); (4) lower cost for the basic materials; (5) wet-chemical processing is feasible; and (6) high-quality epitaxial films and nanostructures can be grown at a low temperature (~ 400°C). A high saturation velocity has been predicted to be ~ 3×10^7 cm/s, [5] potentially leading to fast electronic devices. ZnO has a large photoconductivity, making it suitable for UV photodetectors [6, 7].

An interesting topic in the solid-state electronics is the fabrication of low dimensional material systems to introduce quantum confinement effect. The electron-hole oscillator strength will have orders of magnitude enhancement in a nanostructure, due to the dramatically increased joint density of states near the van Hove singularity. Nanostructured optoelectronic and electronics devices have attracted much interest due to improved device performance in comparison with their counterparts without nanostructures. For instance, low lasing threshold, low temperature sensitivity, high

differential gain and high modulation bandwidth have been obtained in infrared semiconductor laser when quantum dots layer is used as the active layer [8]. A Si photoconductive photodetector with nanostructured grating in the active region has shown increased responsivity, higher internal quantum efficiency and faster photoresponse [9]. In addition, miniaturized single nanowire devices are the building blocks for the integrated electronics and photonics of next generation.

Among various nanoscale materials, ZnO nanostructure has been placed among the most prosperous candidates, which stimulates a lot of research interests. Bulk ZnO has a small exciton Bohr radius in a range of 1.8-2.3 nm [10-12]. Therefore, the quantum confinement effect in ZnO nanowires should be observable at the scale of an exciton Bohr radius. The well-width dependent PL blue shift has been observed in ZnO/MgZnO MQW epitaxial nanorods, [13, 14] with the ZnO well-widths ranging from 1 to 5 nm. Quantum size effect also caused a blue shift in free excitonic emission in ZnO nanorods with diameters smaller than 10nm [15]. The extremely giant oscillator strengths of free exciton and biexciton emission lead to a thermally stable low threshold lasing in ZnO nanowires. ZnO is a polar semiconductor. It shows strong exciton-polariton interactions and has been identified as the *most suitable* semiconductor for a room temperature polariton laser [16]. In a polariton laser, no population inversion is required to achieve optical amplifier. The strong light-matter coupling in a resonant microcavity produces coherent light amplification due to bose condensation of exciton polaritons, forming the basis of a theoretically zero threshold and spin-polarization conserved stimulated emission.

Compared with bulk materials, another significant characteristic of nanostructures is the high surface-to-volume ratio. ZnO nanowires have the same lattice constants and crystal structure of bulk, confirmed by powder XRD and TEM data [17-19]. Therefore, many bulk properties are still preserved. Furthermore, doping and energy band engineering can be made in the ZnO nanotips, which are supported by the epitaxial MOCVD growth technique. The Zn-O bond is half ionic and half covalent. Doping in ZnO is much easier compared with other covalent-bond wide bandgap semiconductors, such as GaN. By appropriate doping, the electrical conductivity of ZnO can be tailored from semiconducting to semi-metal, keeping high optical transparency to the visible and UV wavelength. An important consideration for space communication applications is that the material should be radiation hard, resistant against high energy particle bombardment. ZnO nanotips are attractive for field emission due to anti-oxidization, low emission barrier, high saturation velocity and high aspect ratio. These make ZnO an ideal candidate among transparent conducting oxides (TCOs) for field emission displays and transparent electronics.

UV light sources are of strong research interest because of their broad applications, including non-line of sight covert communication, bio agent detection, high-density optical storage and UV photonics. ZnO is closely lattice matched with GaN. Therefore, when integrated with mainstream GaN light emitting diode (LED) and laser diode (LD) technology, ZnO nanostructure can be used for high efficient solid-state light source, such as a high light extraction efficient UV/blue nanoLED. We have reported that single crystalline and highly oriented ZnO nanotips can be grown on Si and GaN substrates by a catalyst-free growth process, providing a potential integration of ZnO

nanotip arrays with Si and GaN devices [20, 21]. Because of the diversified choices of the substrate materials for ZnO nanotips, including glass, metals, Si, and GaN, novel vertical nanotips based devices can be developed, which are significant in both scientific research and engineering application.

1.2 Scope of Work

The objectives of this research are to develop *in-situ* n-type doping of ZnO nanotips, and conduct feasibility studies on the prototype of n-ZnO nanotips/p-GaN light emitting devices. Two types of ZnO nanotips/GaN LEDs will be fabricated, including: (i) n-ZnO nanotips/p-GaN heterojunction devices and (ii) ZnO nanotips/TCO/GaN LEDs. In type (i) device, ZnO nanotips are grown on top of p-GaN to form p-n junction, and serve as an active layer. In type (ii) device, ZnO transparent conductive oxide (TCO) and ZnO nanotips are directly grown on top of a GaN LED, and act as a transparent conductive and a passive light extraction layer, respectively.

In addition, the excitonic emission properties of ZnO nanotips will be studied. The scope of work covers:

- Optical studies of ZnO nanotips using temperature dependent photoluminescence (PL) spectroscopy.
- Studies of optical and electrical properties of *in-situ* n-type doping of ZnO nanotips using MOCVD technique.
- Fabrication and characterizations of integrated ZnO nanotips/TCO/GaN LEDs for higher external quantum efficiency; explore the possible light extraction enhancement mechanism.

- Fabrication and characterizations of prototype vertical n-ZnO nanotips/p-GaN heterojunction LEDs.

1.3 Organization of the Dissertation

After establishing the motivation and importance of the related work in Chapter 1, a technical background of the growth and characterizations of ZnO nanostructures, including optical properties, are reviewed in Chapter 2. Also reviewed in Chapter 2 is current develop status of ZnO nanostructure based devices. In Chapter 3, *in-situ* n-type doping of ZnO nanotips and their structural, optical, and electrical characterizations are presented. The temperature-dependent excitonic emission dynamics for bound and free excitons are discussed in Chapter 4. In Chapter 5, a prototype hybrid n-ZnO nanotips/p-GaN heterojunction light emitting diode is fabricated. Integrated ZnO nanotips/TCO/GaN LEDs for enhanced light extraction efficiency are described in Chapter 6. Light extraction enhancement mechanisms are investigated and analyzed, and compared with the electroluminescence (EL) testing results from a conventional Ni/Au p-contacting GaN LED. Finally, Chapter 7 summarizes the work accomplished and proposes future investigations in the related areas.

Chapter 2. Technical Background

2.1 ZnO Nanostructures

The growth of ZnO 1-D nanostructures are mostly based on bottom-up approaches using self-assembly or directed assembly of template. As compared with top-down techniques, the bottom-up techniques do not require nanolithography but are still capable of producing nanosize features. A self-assembly growth could be a self-limited process spatially defined by the template, or a self-ordering process established upon a dynamic balance of two opposite physical or chemical interactions, such as attractive and repulsive forces, diffusion and dissolution.

A wide variety of growth techniques have been used in the synthesis of ZnO nanostructures, from simple thermal evaporation to more sophisticated epitaxial growth techniques, for instance, vapor phase transport, thermal evaporation, chemical vapor transport and condensation (CVTC), sputtering and pulse laser deposition (PLD), molecular beam epitaxy (MBE), chemical vapor deposition (CVD) and metal-organic chemical vapor deposition (MOCVD) [22-26]. Other growth techniques include template-assisted growth [27] and solution-based synthesis [28-30].

The growth mechanisms for ZnO nanowires have been attributed to vapor-liquid-solid (VLS), screw dislocation growth, catalyst-free self-nucleation growth, and vapor-solid (VS) mechanism. During a VLS process, a liquid phase is formed initially, due to formation of a eutectic phase. Upon supersaturation of the liquid alloy, a nucleation center forms, and serves as a preferred site for the axial growth of a nanowire. The adsorbed gas reactants are then diffused through the liquid phase to the solid-liquid interface, and the growth of the solid phase proceeds. Due to the much larger

accommodation coefficient of the reactants in the liquid, growth is much faster at the solid-liquid interface as compared to the solid-vapor interface [31-33]. The screw dislocation growth is a structural defect evolved process to usually form nanowhiskers [34, 35]. When the line of a screw dislocation is parallel to the growth axis of the nanowire, e.g. c-axis of ZnO nanowires, the spiral plane perpendicular to the screw dislocation line possesses a low-energy step, which acts as a site for sequential growth. Thus, the growth rate along the dislocation line is much faster compared to that of the radial direction. This results in the formation of a 1-D nanostructure [36, 37]. Typically, the end tip of the nanowires obtained from this mechanism is conical with a spiral honeycomb-like morphology. A characteristic of screw dislocation growth is the presence of axial screw dislocations that is often evident from TEM.

The formation of ZnO nanowires with sharp prismatic tips from MOCVD can be attributed to catalyst-free, near-equilibrium self-nucleation growth. ZnO nucleates on the surface of the substrate as a result of the reaction between adsorbed oxygen and zinc from Diethyl Zinc, similar to ZnO epitaxial growth. The nucleation can be enhanced by the presence of impurities, high temperature, or presence of a secondary phase, which reduce the nucleation energy. As-formed ZnO nuclei could follow an epitaxial relationship with a lattice-matched substrate. The nuclei thus formed then reach a critical size, and begin to grow in all directions. The growth habit of the nuclei depends on the relative growth rates of the different crystal faces bounding the nuclei. The growth rate (R) relationship for different ZnO crystal faces is $R_{<001>} > R_{<101>} > R_{<100>} > R_{<00\text{-}1>}$. Thus growth along the c-axis [0001] has the highest growth rate, while the negative c-axis $[000\bar{1}]$ has the lowest growth rate [38]. As the growth rate is much more favored along the c-axis and it is the

direction of free growth without size limitation, it grows into nanowires with sharp prismatic tips. These nanowires not only grow in height but also increase in width. The aspect ratio of the nanowires can be adjusted by control of the growth conditions [36, 39].

The vapor-solid (VS) mechanism is another catalyst-free process. In a VS process, the solid is directly vaporized at a higher temperature and deposited onto a substrate to form nanostructures [40]. According to Sear's model, the atoms are impinged onto a whisker side surface, adsorbed onto the surface, and diffused along the lateral surface into an atomic sink at the tip of the whisker. Those atoms not reaching the tip are removed by re-evaporation because of their unstable energies [41]. As a result, 1-D crystal growth occurs at the tip of the nanowire, where an enormous atomic sink exists. The sequential growth is a diffusion-limited process. Unlike VLS, VS-governed growth proceeds at the vapor and solid crystal interface.

ZnO nanowire growth based on a chemical vapor transport and condensation (CVTC) method has been reported [42-44]. A CVTC growth may use Zn vapors in an oxygen ambience. Zn evaporated over the substrate reacts with oxygen to form ZnO, which then condensed onto the substrate surface. The growth temperatures reported for vapor transport systems are typically higher than 900°C. CVTC growth requires a few hours of pre-annealing if Au pre-deposition onto the substrate surface is involved. Pre-annealing of Au results in the formation of small Au islands, which act as nucleation centers for the subsequent growth of ZnO nanowires. The size of the ZnO nanowires obtained depends greatly on the size (diameter and thickness) of these Au islands. The growth mechanism of CVTC is mostly due to VLS that needs the metal catalyst.

Thermal evaporation is used to synthesize 1-D ZnO nanostructure [45-47]. ZnO powders are heated and vaporized at a high temperature; mostly in the range of 1100°C ~ 1400°C. Deposition of ZnO nanostructures occurs on the substrate placed in the downstream of the carrier gas. Certain growth directions and surface planes are exhibited. The formation of nanobelt is ascribed to a vapor-solid process. The morphology and optical properties of nanostructures greatly depend on the specific substrate temperature as well as the carrier gas species. Other approaches reported to prepare single-crystal ZnO nanowires include wet oxidation of a zinc and selenium mixture in a heating furnace [48], where Se serves as a liquid-forming agent in VLS growth, or thermal evaporation of zinc and carbon mixture in oxygen ambient. Zn or Zn suboxides are proposed to be the nucleation center for nanowire growth via a VLS-like mechanism.

MOCVD growth follows catalyst-free growth mechanism, which is preferred to reduce the impurity incorporation. It is a process based on pyrolytic reactions, which uses metalorganic precursors as the reactant species. These metalorganics have only one dangling bond and can be easily converted to chemical vapors. This allows the use of a low growth temperature, depending on the vapor pressure of the precursor. The precursor compound used in the MOCVD system has a reasonable vapor pressure and a low melting point. A carrier gas transports the vapors of the reacting species. The reaction then proceeds on the substrate surface heated at the growth temperature. The MOCVD technique has several advantages, such as chemical and thermodynamic dependent growth, low growth temperature, control at the atomic level, large area deposition for mass production, and high growth rate. It also provides the flexibility of *in-situ* doping processes. Energy band engineering can be realized by appropriately choosing reactant

species and growth conditions. Moreover, the MOCVD technique is compatible with well-developed semiconductor processing technology due to the low growth temperatures. The catalyst-free nature of MOCVD growth of ZnO nanowire eases the post-growth purification process.

ZnO nanorod or nanotip growth on various substrates, such as c-plane sapphire, fused silica, metals, Si and GaN using MOCVD was reported [20, 21, 49]. The nanotip growth mechanism is attributed to a catalyst-free self-nucleation process and a layer-by-layer growth mode. The columnar growth is a result of the highest growth rate along the ZnO c-axis. ZnO is a polar semiconductor, with (0001) planes being Zn-terminated and $(000\bar{1})$ being O-terminated. These two crystallographic planes have opposite polarity, hence have different surface relaxation energies, resulting in the highest growth rate along the c-axis. Therefore, by controlling the ZnO growth parameters, ZnO nanotips with c-axis perpendicular to the substrate and with a high aspect ratio can be grown on various substrates.

2.2 Optical Properties of ZnO Nanostructures

The optical transitions in ZnO consist of intrinsic and extrinsic optical transitions. Intrinsic transitions are radiative recombination of electrons in the conduction band and holes in the valence band, and free excitonic emission (FX). Extrinsic transitions are radiative recombination involving defects and impurities, such as emissions from bound exciton (BE), donor-acceptor pair (DAP), free-to-bound (e.g. eA), or broad yellow/green/blue mid-bandgap luminescence.

2.2.1 Intrinsic Optical Transitions

ZnO has the wurtzite crystal structure, belonging to point group C_{6v}^4. In contrast with the cubic structure, the lower symmetry of the wurtzite structure leads to anisotropy in the electronic and optical properties of ZnO along c-axis and perpendicular to c-axis. The energy band structure of ZnO has an s-like lowest conduction band (Γ_7 symmetry) and three p-like valence bands. Direct interband transition occurs at Brillouin zone center ($\mathbf{k} = 0$).

(a) Spin-orbit coupling (Δ_{so})

An electron moving through an electric field, such as that the periodic potential of the crystal lattice, experiences a potential proportional to the scalar product of its velocity and the electric field. This additional interaction is referred to as the spin-orbit coupling. Spin-orbit coupling tends to remove the degeneracy of states with the same wave function and opposite spin. Spin-orbit coupling leads to a partial lifting of the valence band degeneracy, the formerly six fold degenerate valence band is split into a fourfold (j = 3/2) and a twofold (j = 1/2) band. In ZnO, the spin-orbit coupling is negative due to the negative contribution from the zinc *d* band in the valence band, which results in the j = 1/2 band to be at a higher energy than the j = 3/2 band [50, 51].

(b) Crystal field splitting (Δ_{cf})

Another type of perturbation occurs due to the interaction of the inner electron shells (d-shell in Zn) with the non-negligible electric field of the surrounding crystal lattice, which does not have a spherical symmetry but the symmetry of the crystalline site at which the ion is located. This perturbation is known as the Crystal Field Splitting, and

results in the splitting of the valance band into Γ_5 and Γ_1 states [52] (in the absence of spin-orbit coupling).

The p-like valence bands are split by the spin-orbit and crystal-field interactions, shown in figure 2.1 [53]. In figure 2.1, a negative spin-orbit splitting is used for illustration. Figure 2.2 shows the band structure and symmetries of hexagonal ZnO [54]. Table 2.1 summarizes the band structure related properties of wurtzite ZnO [54].

The valence band ordering of ZnO has been in controversy for decades. Thomas et al. assigned the three valence bands as A-Γ_7^v, B-Γ_9^v and C-Γ_7^v in the order of increasing transition energy to the conduction band [55], whereas Park et al. assigned the order as A-Γ_9^v, B-Γ_7^v, and C-Γ_7^v [56]. The difference arises from the interpretation of the spectral line, which Thomas assigned to intrinsic ground-state A-exciton transition, while Park interpreted as an ionized donor-bound exciton complex transition. Recently, Reynolds et al. concluded the valence-band symmetry ordering of A-Γ_9^v, B-Γ_7^v, and C-Γ_7^v using polarized magnetoluminescence measurement [57]. However, Lambrecht et al. conducted the first-principles band structure calculations and suggested the first assignment [58].

The transition selection rules in hexagonal ZnO are predicted as follows: transition between A (B) valence band and the conduction band is mainly allowed for the light polarization **E** perpendicular to c-axis (**E** $\perp$ c), where **E** is the electric field component of the incident light, while transition between C valence band and the conduction band is mainly allowed for the light polarization **E** parallel to the c-axis (**E** // c). The transitions between the conduction band and valence bands can be represented using the group theory [59, 60]:

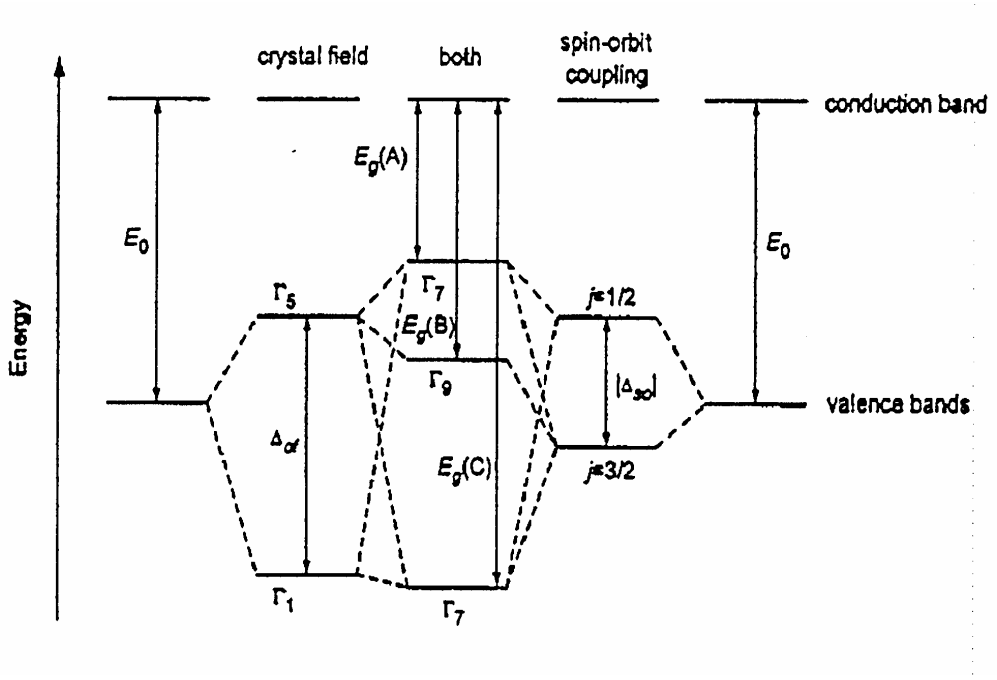

Figure 2.1. Splitting of the valence band in hexagonal ZnO by crystal-field splitting and spin-orbit coupling [53]. The figure is not drawn to scale.

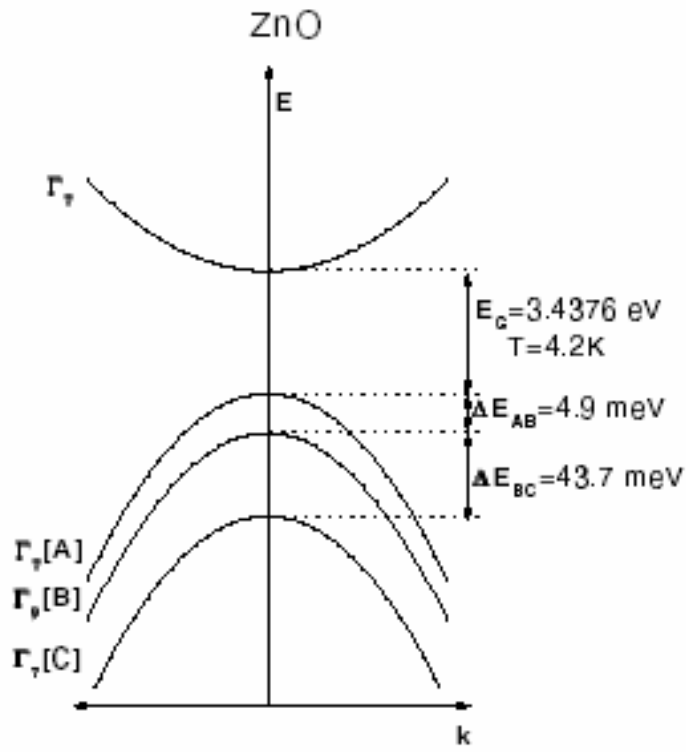

Figure 2.2. Band structure and symmetries of hexagonal ZnO [54].

Table 2.1: Band structure related properties of wurtzite ZnO [54]

E_{gA}	3.437 eV	(T = 1.6 K)
E_{AB}	4.9 meV	
E_{BC}	43.7 mev	
E_{gB}	3.4425 eV	
E_{gC}	3.4813 eV	
Temperature dependence of the band gap up to 300 K		
$E_g(T) = E_g(T=0) \frac{5.05 \cdot 10^{-4} \cdot T^2}{900 - T}$		
Dielectric constants		
$\varepsilon(0) \perp c$	7.8	
$\varepsilon(0) \parallel c$	8.75	
$\varepsilon(\infty) \perp c$	3.7	
$\varepsilon(\infty) \parallel c$	3.75	
Electron effective (polaron) mass in units of m_0		
$m_e^* \parallel$	0.28	
$m_e^* \perp$	0.24	
Hole effective mass in units of m_0		
$m_h^*(A)$	0.59 $\parallel = \perp$	
$m_h^*(B)$	0.59 $\parallel = \perp$	
Crystal field splitting in meV		
Δ_{cf}	41.7	
Spin orbit splitting in meV		
Δ_{so}	−8.0	
Electron g-values		
$g_e^{\parallel}$	1.956 – 1.958	
$g_e^{\perp}$	1.955 – 1.956	
Hole g-values		
$g_A^{\parallel}$	−2.45	
$g_A^{\perp}$	0.09	
$g_B^{\parallel}$	1.5	
$g_B^{\perp}$	0	
$g_C^{\parallel}$	1.95	
$g_C^{\perp}$	1.91	
Landé g-factors for the hole participating in the 1S exitons		
$g_A^{\parallel}(1S)$	−1.32	
$g_B^{\parallel}(1S)$	3.04	
$g_C^{\parallel}(1S)$	1.06	
Phonon modes at T = 300 K in cm^{-1}		
E_2^{low}	101	
E_2^{high}	437	
TO (A_1)	380	
LO (A_1)	574	
TO (E_1)	591	

$$\Gamma_7^v \rightarrow \Gamma_7^c : \Gamma_7 \times \Gamma_7 = \Gamma_1 + \Gamma_2 + \Gamma_5 \quad (2.1)$$

$$\Gamma_9^v \rightarrow \Gamma_7^c : \Gamma_9 \times \Gamma_7 = \Gamma_5 + \Gamma_6 \quad (2.2)$$

where Γ_2 and Γ_6 states are transition forbidden; Γ_1 and Γ_5 states are the eigen-states corresponding to light polarization parallel (**E** // c) and perpendicular **(E** $\perp$ c) to the c-axis, respectively. Therefore, all three fundamental ground-state excitons of ZnO are allowed in the σ polarization (**E** $\perp$ c and **k** $\perp$ c), but the c exciton is very weak in terms of the oscillator strength. The c exciton is strong in the π polarization (**E** // c and **k** $\perp$ c), but A and B excitons are weak in this configuration. All three excitons are allowed in the α polarization (**E** $\perp$ c and **k** // c).

The additional features of intrinsic exciton states include exciton excited states, exciton-polariton longitudinal-transverse splitting, electron-hole exchange interaction, and rotation states, etc. ZnO is a strongly polar material, therefore, its free excitons can significantly couple with photons to form polaritons (i. e. upper polariton branch (UPB) and lower polariton branch (LPB)). Strong exciton-longitudinal optical phonon coupling also occurs, leading to exciton scattering and relaxation. The intrinsic excitonic emissions of ZnO occur in the spectral range of 3.376 - 3.472 eV [61-64]. The energy separation between the A and B free exciton is in the range of 9-15 meV [65, 66].

In theory, the exciton Rydberg energy of ZnO (i. e. $Ry^* = 13.6eV*\mu/(m_0*\varepsilon^2)$) is 60 meV [67]. A. Teke et al. have shown that the ground-state free A exciton and its first excited state in high-quality bulk ZnO have an energy separation of 45meV. Based on the hydrogen-like effective mass model, a free A exciton binding energy of 60meV was calculated, giving the energy bandgap of 3.4372 eV at 10K in bulk ZnO [68]. Another approach is to artificially generate the higher order exciton states due to exciton-exciton

scattering using a high optical excitation. Through the identification of so-called P-band in ZnO, the energy difference between the first-excited state and the ground state of the free exciton are determined. Sun et al. have experimentally found that the exciton binding energy in epitaxial ZnO films is ~ 60meV [69].

Table 2.2 lists the peak positions of intrinsic exciton emissions observed in bulk ZnO single crystals.

Table 2.2: Summary of intrinsic exciton transitions in bulk ZnO [64, 68]

	$FX_A^{n=1}(\Gamma_5)$	$FX_A^{n=1}(\Gamma_6)$	$FX_A^{n=2}(\Gamma_5)$	$FX_A^{n=2}(\Gamma_6)$	LPB_A	UPB_A	$FX_B^{n=1}$	$FX_B^{n=2}$	$FX_C^{n=1}$	$FX_C^{n=2}$
Teke *et al.*	3.3771	3.3757	3.4220	3.4206	3.3740	3.3810	3.3898			
Reynolds *et al.*	3.3773	3.3756	3.4221	3.4209			3.3895			
Reynolds *et al.*	3.3793	3.3775			3.3743	3.3829				
Hamby *et al.*	3.378				3.374		3.385			
Muth *et al.*	3.40						3.45		3.55	
	(295 K)						(295 K)		(295 K)	
	3.455						3.516		3.60	
	(77 K)						(77 K)		(77 K)	
Chichibu *et al.*			3.4231		3.3768	3.3783		3.4290		3.4679
Park *et al.*	3.3931		3.4243				3.4331		3.4696	
Thomas	3.3768						3.3828		3.4208	
Liang andYoffe	3.3781		3.4282				3.3856	3.4324	3.4264	3.4722

2.2.2 Extrinsic Optical Transitions

When the free excitons are localized by defects and impurities in ZnO, bound excitons (BE) are formed. Free exciton can bound to neutral or charged donors and acceptors in ZnO, where a strong coupling of the quasi-particles in the bound exciton states is assumed. For donor bound excitons, the two electrons in the BE states pair of and form a two-electron complex with zero spin, while a hole is weakly bounded. In as-grown ZnO nanotips, the neutral donor bound exciton (DX) emissions are always the most intense because of shallow-donor-like point defects and unintentional dopants. DX

often give the sharpest lines in the spectrum (< 1-2 meV in half width), suggesting these bound excitons may not have any degree of freedom for translational motion. Significantly, strong acceptor bound exciton (AX) emissions can also be observed in ZnO when Group V elements are incorporated for p-type doping (such as a nitrogen acceptor related AX peak at 3.232eV [70]), as compared to the broad DAP recombination in the PL of p-type GaN [71, 72].

The sharp bound excitonic emissions of ZnO occur in the spectral range of 3.348 - 3.374 eV, giving the exciton-to-donor binding energies of 10-20 meV [73-75]. Among these emissions, the acceptor-bound excitons often occupy on the low-energy side (3.356 – 3.348eV) [76-78], due to higher ionization energies of the acceptors compared with that of the shallow donors. The additional fine features of bound exciton states in ZnO include excited states and excited rotator states, locating at the high-energy side of the ground states. Other fine structures may show two-electron satellite (TES) transitions, which is the radiative recombination of a donor bound exciton emission with the donor left in the excited state. TES has been observed in the spectral range of 3.32 -3.34 eV [79, 80].

The exciton binding energy is found proportional to the donor bind energy, where the Haynes constant in bulk ZnO is experimentally found to be ~ 2 [81]. Table 2.3 lists bound exciton transitions observed in bulk ZnO, though the chemical origins of most donors and acceptors are still unknown and currently under extensive investigations.

Table 2.3: Summary of bound exciton transitions in bulk ZnO [64]

	Neutral acceptor bound excitons			A excitons bound to neutral or ionized donors						Rotator states		B excitons bound to neutral donor
Present work	3.3481	3.3530	3.3564	3.3598	3.3605	3.3618	3.3634	3.3650	3.3664	3.3686	3.3702	3.3724
							3.3643					
Reynolds *et al.*			3.3562	3.3594	3.3602	3.3610	3.3624	3.3652		3.3670	3.3702	
							3.3634			3.3664	3.3714	
Alves *et al.*			3.358		3.361	3.362		3.364				
Thonke *et al.*			3.3566	3.3597	3.3606	3.3620	3.3628	3.364				
Boemare *et al.*				3.3592			3.3622	3.3653	3.3693	3.3693	3.3741	3.3707
							3.3632			3.3707	3.3754	3.3741
												3.3754
												3.3772

Donor acceptor pair (DAP) emission and its LO phonon replicas are other types of extrinsic emission commonly observed in ZnO. DAP luminescence results from the radiative transition of a donor state to an acceptor state in the bandgap if their wavefunctions overlap. A characteristic feature of DAP emission is that, when increasing the pump intensity, the emission maximum of the pair-band shifts to higher energy due to the decrease in average distance between the donor and acceptor centers. Another radiative process in ZnO is free-to-bound transition. In ZnO, only the recombination of a free electron with a neutral acceptor has been observed (denoted by eA), because of the easier thermal ionization of a shallow donor. Free-to-bound emission of ZnO occurs at the high energy side of the corresponding DAP peak, whose energy separation has been reported in an order of tens of meV [82, 83].

2.2.3 Photoluminescence of ZnO Nanostructures

As reviewed in sections 2.2.1 and 2.2.2, most optical studies of ZnO have been conducted on bulk ZnO. Optical properties of ZnO have been characterized using optical

absorption, transmission, reflection, spectroscopic ellipsometry, photoreflectance, photoluminescence (PL), cathodoluminescence, and magnetoluminescence, etc. Among these techniques, PL is a convenient and powerful tool, and has been most widely utilized to characterize the crystalline quality and the point defects in ZnO. However, the assignments of specific excitonic emissions and their chemical origins in ZnO are still the subject of controversy, because the concentration of defects and impurities highly relies on the specific samples and growth runs, particularly, for ZnO nanotips which have been mostly heteroepitaxially grown on a lattice mismatched substrate.

Free excitonic emission was observed at 10K in ZnO nanowires grown on c-Al_2O_3 using MOVPE [84]. The near band edge emission of these nanowires consists of four peaks at 3.359, 3.360, 3.364, and 3.376 eV with full width at half maximum (FWHM) of 1–3 meV, respectively. The PL peak at 3.376 eV is assigned to a free exciton peak. The peaks at 3.359–3.364 are attributed to neutral-donor bound exciton peaks (I_2). The observation of the free exciton peak for ZnO nanorods at 10 K was suggested resulting from the catalyst-free growth.

Temperature dependent PL spectra of ZnO nanowires grown on sapphire and Si substrates by an Au catalytic VPT process were reported [85]. The intense emission at 3.6 eV was attributed to a free-to-bound transition with a binding energy of 124 meV for the bound state. B. P. Zhang et al. studied the excitation power dependence of PL spectra of ZnO rods [86, 87]. The biexciton emission was observed in these rods, shown by the appearance of the superlinear power dependence M band (3.3599eV). The biexciton is found to have a binding energy of 17.3meV and an effective temperature of 35K. The PL line at 3.315eV was assigned to DAP emission with an acceptor binding energy of ~

107meV. Y. Gu et al. reported the thin quantum confinement effects in thin colloidal-synthesized ZnO nanorods with radius of ~ 1nm [88]. The exciton binding energy was found significantly enhanced, giving a specific enhancement factor ($\gamma = E_B$ (1D)/ E_B (3D)) of > 6.

Stimulated emission was demonstrated in ZnO nanowire arrays at room temperature [89-92]. The nanowire array was grown on an Au-patterned a-sapphire substrate via a VLS growth mechanism. The nanowires have diameters of 20-150 nm and lengths up to 40 μm with high area density of 10^{10} cm^{-2}. The samples are pumped by the fourth harmonic of an Nd: YAG laser at room temperature. Light emission was collected along the c-axis of the nanowire. Surface-emitting lasing was observed at 385 nm, with FWHM less than 0.3 nm, much narrower than that of spontaneous emission pumped by a He-Cd laser. The stimulated emission has a low lasing threshold of ~ 40 $KWcm^{-2}$, one order lower than that of bulk and epitaxial ZnO thin films (~ 240 $kWcm^{-2}$) [93]. The low lasing threshold has been attributed to an enhanced photon and carrier confinement in the ZnO nanowires. The nanowires are single-crystalline and well-facetted, therefore serves as individual self-contained Fabry-Perot resonance cavities. This cavity-like lasing mechanism is further proved by measuring near-field scanning optical microscope (NSOM) for a single nanowire [93].

The emission dynamics was also evaluated in ZnO nanowires. Yang et al. measured time-resolved PL spectrum of ZnO nanowires grown on a-sapphire by an Au catalytic CVTC process [94]. The relaxation process of the radiative recombination in ZnO nanowires consists of a fast component (70 ps) and a slow component (350 ps), as compared to 200 ps in ZnO thin films. The long lifetime has been attributed to reduced

defects and impurities in ZnO nanowires, such as zinc vacancy complexes, leading to reduced electron or hole traps that generate nonradiative recombination channels.

2.3 ZnO Nanostructure-based Devices

Most work on ZnO nanostructure devices has been carried out using the "pick-and-place" manipulation of randomly dispersed ZnO nanowires. ZnO nanowires are usually scratched from the growth substrate, then sonicated in an organic liquid drop and dispersed onto a template. After picking up an appropriate single nanowire, metal contacts are deposited on both ends of the nanowire using nanolithography. Therefore, most devices are randomly located and horizontally lying on the template surface. By utilizing such geometry, many physical properties of ZnO nanowires have been characterized and studied [95-97]. For instance, large photoconductivity of a single ZnO nanowire was reported [98]. The ZnO nanowires with diameters ranging from 50 to 300 nm were dispersed on pre-fabricated gold electrodes. Electrical resistivities without and with UV light irradiation were measured in a four-terminal configuration. The conductivity of ZnO nanowire under UV irradiation increases by 4 to 6 orders of magnitude compared with the dark current, with a response time in the order of seconds. The photoresponse has a cutoff wavelength of ~ 370nm. Recently, Z. Fan et al. studied photocurrent temporal response, showing that the photoconductivity of ZnO nanowires was strongly polarization dependent [99].

There have been only several reports on the vertical ZnO nanowire devices, including nanowire LEDs and single nanowire FETs [100, 101]. Konenkamp et al. fabricated vertical ZnO nanowire LED, showing white-color electroluminescence [100].

ZnO nanowires were grown on fluorine-doped SnO_2-coated glass substrates by electrodeposition from aqueous solutions. The ZnO columns have diameters of 100-200nm, and 2 μm in length. The space between the nanowires was filled using polystyrene. A 0.5-1.5 μm coating of poly (3, 4-ethylenedioxythiophene) provided a p-type contact to the nanowire tips, and a 100nm Au deposition formed a Schottky contact for hole injection. The EL was observed at a threshold of 10V with a current density of 100mA/cm^2 at the nanowire tips. A defect band centered at 620nm is observed in the EL spectrum.

Ng. et al. demonstrated a single ZnO nanowire vertical surround-gate field-effect transistor [101]. Both n- and p- channel FETs were fabricated. The vertical aligned ZnO nanowires were grown on close-lattice matched SiC substrates by Au catalyst-assisted carbothermal reduction deposition at a growth temperature of 925°. The nanopatterned Au islands determine the growth sites of the nanowires. The ZnO nanowires have diameters of ~ 40nm and lengths of ~1um, spacing 1um apart. The underlying P^+-SiC serves as the bottom source contact for the single nanowire. Conformal CVD deposition of 20nm thick SiO_2 was used to encapsulate the nanowires, then chemical mechanical polishing (CMP) was used to remove SiO_2 at the nanowire tip and expose Cr surround-gate electrode. A selective wet etching of Cr was performed to form ~ 30nm recess. The recess was filled by SiO_2 CVD, followed by another CMP to expose the tips, and finally a 100nm top Cr was deposited for the drain contact. The n-FET is normally on and turn off at a threshold voltage V_{gs} = -3.5V, while p-FET has a threshold voltage of 0.25V. The transconductance per nanowire is 50ns and 25ns at $|V_{ds}|$ = 1V for n-channel and p-channel, respectively.

Despite a few groups reported the heterojunction devices of n-ZnO/p-Si and n-ZnO/p-GaN, all the work has been done on ZnO epitaxial or polycrystalline films. There have been few reports on n-ZnO nanotips/p-Si and n-ZnO nanotips/p-GaN devices.

Alivov et al. observed 430nm electroluminescence from an n-ZnO/p-GaN heterojunction LED under a forward bias of 3V [102]. The LED layer structure consists of 1μm Mg-doped GaN film grown on c-sapphire and 1μm Ga-doped ZnO film on the top. By comparing CL and EL emission spectra, they suggested that the EL emission of the n-ZnO/p-GaN hereojunction primarily origin from the electron injection from n-ZnO to the p-GaN side. EL emission from an n-ZnO/p-AlGaN heterojuntion LED was also demonstrated with a peak wavelength near 389nm [103]. This LED has a 0.8μm Mg-doped $Al_{0.12}Ga_{0.88}N$ film grown on a 6H-SiC substrate with another 1μm Ga-doped ZnO film on top of p-AlGaN. The diode showed a threshold voltage ~ 3.2V and low leakage current ~ 10^{-7} A, which was ascribed to the improved lattice match in the n-ZnO/p-AlGaN/SiC structure. PL and EL studies show that the predominant hole injection from p-$Al_{0.12}Ga_{0.88}N$ region into n-ZnO region lead to the UV luminescence. The emission is found thermally stable at temperatures up to 500K, suggesting its excitonic nature.

Spectral response and quantum efficiency of an n-ZnO/p-Si photodiode were characterized [104]. The photodiode exhibited a cutoff at 380nm at near UV, with a maximum quantum efficiency of 70% at 650nm and a minimum of 10% at 420nm. However, the p-n diode didn't show a good rectifying junction under dark, possibly due to defect mediated ZnO/Si heterointerface and bulk material.

2.4 Summary

The scope of the thesis work is among the highly active research frontier. Most optical studies of ZnO have been conducted on bulk ZnO. However, the assignments of specific excitonic emissions and their chemical origins in ZnO are still in wide controversy, where the peak identifications highly rely on the specific samples and growth runs. Particularly, ZnO nanotips have been mostly heteroepitaxially grown on lattice-mismatched substrates. Therefore, the excitonic emissions of ZnO nanotips need to be studied. We will investigate *in-situ* n-type doping of ZnO nanotips and study the doping effects on optical and electrical properties of ZnO nanotips. In terms of ZnO related devices, most of the work has been done either on making heterojunctions on ZnO films or using randomly dispersed ZnO nanowires to study their physical properties. In this dissertation work we will investigate the feasibility to fabricate vertical n-ZnO nanotips/p-GaN heterojunction light emitting devices. Finally, a novel integrated ZnO nanotips/TCO/GaN LED will be explored, in which ZnO nanotips serve as a passive light extraction layer for enhanced external quantum efficiency.

Chapter 3. Properties of Ga-doped ZnO Nanotips

Controllable *in-situ* doping is critical for realizing nanoscale electrical and optical devices. Under most growth conditions, undoped ZnO is intrinsically n-type due to the presence of low energy native point defects such as oxygen vacancies (V_o) and Zn interstitials (Zn_i), and shallow donors from impurities such as hydrogen. Theoretical investigation suggests that Zn_i as a native shallow donor have ionization energy of ~ 30-50 meV [105]. First principles calculations based on density functional theory and spectroscopic analysis confirm that interstitial hydrogen at a bond-centered site behaves as a shallow donor in ZnO with ionization energy of ~ 30 meV [106, 107]. Hydrogen can also be bound to native defects forming a hydrogen-complex donor. Other extended structural defects, such as native defects, extended defects or defect complexes are responsible for the n-type background in undoped ZnO. However, the unipolar conductivity resulting from defects and unintentional impurities is not controllable for practical device applications.

To achieve n-type doping, group-III elements Al, Ga, and In as substitutional elements for Zn and group-VII elements F, Cl and I as substitutional elements for O can be used as n-type dopants. Trivalent cations Al^{3+}, Ga^{3+}, and In^{3+} have higher valence state than Zn^{2+}, which contribute to an electron carrier. Among group III elements Al, Ga and In, we choose Ga as an n-type dopant in ZnO films. Compared with Al, Ga is less reactive and more resistive to oxidation, leading to a better growth control. Near-band-edge (NBE) PL emission of Al doped ZnO films can only be observed at low temperature. Ga has a high solid solubility (>2 at. %) and low activation energy of 50meV in ZnO [108]. The covalent bond lengths of Ga-O and Zn-O are reported to be ~ 1.92 and 1.97 Å,

respectively [109]. This slightly smaller Ga-O bond length makes the deformation of ZnO lattice small even for high Ga doping concentration.

3.1 MOCVD Growth and Characterizations of ZnO Nanotips

ZnO nanotips have been grown on various substrates, including GaN, Si, and glass, using a MOCVD technique. The MOCVD chamber is an axisymmetric rotating-disk vertical flow reactor. The positions of metalorganic and O_2 injectors are designed to minimize gas phase reactions in the chamber. During the nanotips growth the substrate temperature was maintained at ~480°C with typical growth rate of 1-2μm/hr. Metalorganic DiethylZinc (DEZn) and ultra high purity oxygen gas (99.999%) were used as the zinc source and the oxidizer, respectively, while high purity Ar (99.999%) was used as the carrier gas. A Leo-Zeiss field emission scanning electron microscope (FESEM) was used to characterize the morphology of the films and a Topcon 002B transmission electron microscope (TEM) was used to perform detailed structural characterizations. High-resolution x-ray diffraction (HRXRD) analysis using a Bruker D8-Discover four-circle x-ray diffractometer with four bounce Ge (220)-monochromated Cu $K\alpha_1$ radiation. In-plane registry was evaluated by x-ray φ-scans using a general-purpose four-circle diffractometer. PL measurements were performed using a 20 mW He-Cd laser with an excitation wavelength of 325nm. A liquid nitrogen pourfilled optical cryostat through a quartz window was used for the 77K measurements. Absorption spectra were measured by using a double-source DU530 UV/visible spectrometer. It has an interface connected to a computer, and measures a wavelength range from 190nm to

1700nm. Normal incidence transmittance and absorbance of ZnO nanotips samples were recorded. ZnO film thickness was measured by an Alpha-stepper profiler.

Under certain growth conditions, ZnO grown on various substrates shows a columnar structure with rods ending in tips. Columnar growth is a result of the highest growth rate along the c-axis of ZnO. ZnO is a polar semiconductor, with (0001) planes being Zn-terminated and $(000\bar{1})$ planes being O-terminated. These two crystallographic planes have opposite polarity, hence have different surface energies. The (0001) planes in ZnO have the maximum surface energy amongst the low-index planes. The crystals are elongated along the [0001] direction and the prismatic sides of these crystals are usually the $\{10\bar{1}0\}$ or $\{11\bar{2}0\}$ planes, implying that the (0001) plane has the highest energy. The growth rate relationship for different ZnO crystal faces is R<0001> > R<10$\bar{1}$1> > R<10$\bar{1}$0>, where R is the growth rate. As a result, the growth rate along the c-axis is the highest, and oriented nanowires are formed in the c-direction.

3.1.1 ZnO Nanotips Grown on Glass

ZnO nuclei can be formed randomly on amorphous substrate such as SiO_2. Due to the fastest growth rate along [0001] direction compared to the lateral direction, ZnO nanostructures can be grown on amorphous substrates with preferred [0001] orientation. Figure 3.1 shows the FESEM image of the MOCVD grown ZnO nanotips on glass substrate. The as-grown ZnO nanotips are about 500 nm in height, 40-60 nm in diameter, giving an aspect ration of ~ 1:10. Figure 3.2 shows the θ-2θ scan of x-ray diffraction pattern of MOCVD grown ZnO nanotips on glass substrate. The XRD pattern of ZnO

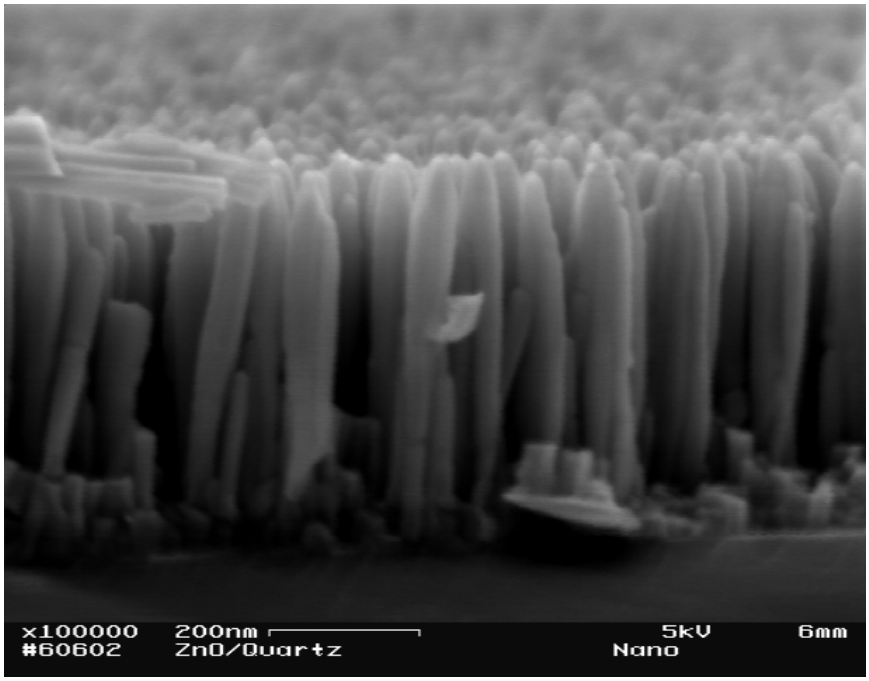

Figure 3.1. FESEM image of ZnO nanotips grown on glass.

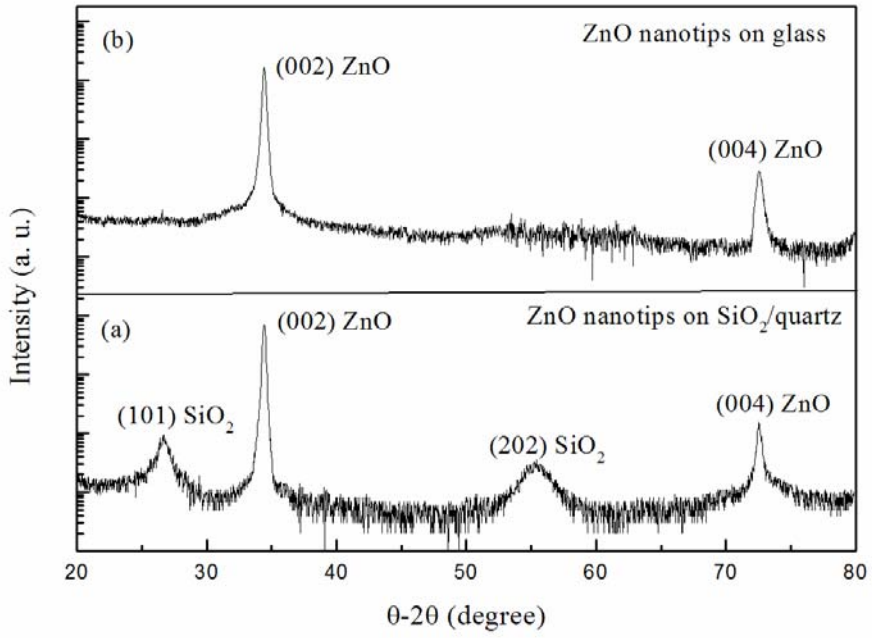

Figure 3.2. XRD data of ZnO nanotips grown on glass.

nanotips grown on amorphous glass substrate only shows (002) and (004) ZnO double peaks. This confirms that the ZnO nanotips have a preferred c-axis (00l) orientation even grown on an amorphous SiO_2 template. As the fused silica layer is amorphous, the initial ZnO crystals that nucleate on the fused silica surface presumably also do not have a specific epitaxial arrangement. A columnar structure may result from either competitive blocking of all crystallites (by other crystallites) whose c-axis is pointing away from the surface normal, or a preferential orientation of the ZnO nuclei on the relatively flat SiO_2 surface once they reach some critical size.

Figure 3.3 (a) and figure 3.3 (b) are room temperature and 77K PL spectra of ZnO nanotips grown on glass, respectively. At room temperature, strong NBE PL emission is observed at 3.277eV. The dominant peak at 3.277eV can be primarily attributed to recombination of donor-acceptor-pair (DAP). No deep level emission is present, showing good optical quality of the nanotips grown on amorphous glass. To determine the peak position and halfwidth, a nonlinear least-square curve fitting is performed to deconvolve the 77K PL spectrum into individual Lorentzian peaks. Shown in figure 3.3 (b), black curve is the measurement result, and red curve is the least-square curve fitting result based on the Lorentzian lineshape. The PL peak at 3.367 eV can be attributed to bound-exciton emission involving neutral-donor. Transition at 3.349 eV may result from the bound exciton emission. We assign the PL line at 3.318 eV to zero phonon line of donor-acceptor-pair (DAP) emission. The DAP emission is accompanied by the first order LO phonon replica at 3.245 eV. The results indicate that the undoped ZnO nanostructures grown on glass have good morphology and crystallinity.

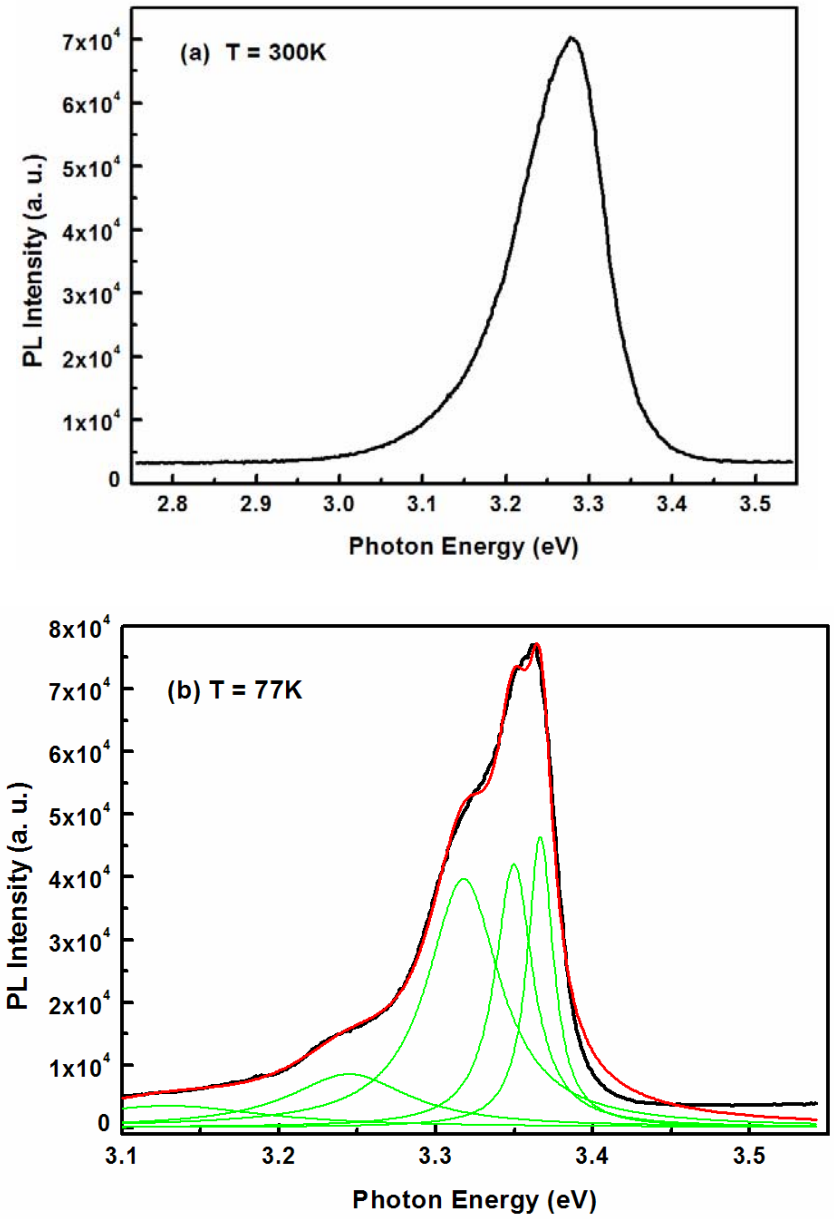

Figure 3.3. (a) Room temperature and (b) 77K PL spectra of undoped ZnO nanotips grown on glass. Black curve is the measurement result; red curve is the least-square curve fitting result based on the Lorentzian line shape. Green curves show individual Lorentzian peaks.

3.1.2 ZnO Nanotips Grown on Si

ZnO nanotips can be grown on Si via a catalyst-free self-nucleation process. A thin SiO_2 layer is formed at the Si and ZnO interface during the initial growth. The ZnO crystals nucleate on the amorphous SiO_2 layer. As the growth rate is more favored along the c-axis, the self-assembled nanotips growth proceeds. Figure 3.4 shows a FESEM picture of ZnO nanotips grown on (100) Si substrate. ZnO nanotips are very dense and predominatingly oriented along the c-axis with uniform size. The diameter of the bottom of nanotips is in the range of 40-60nm and the length is ~ 500nm, giving an aspect ratio of ~10:1. XRD measurement is employed to characterize the crystalline orientation of the ZnO nanotips grown on Si substrate. Shown in figure 3.5, only (0001) ZnO peak is present in the θ-2θ x-ray scan, indicating a preferred c-axis orientation.

Figure 3.6 (a) and figure 3.6 (b) are room temperature and 77K PL spectrum of ZnO nanotips grown on Si substrate, respectively. At room temperature, ZnO nanotips exhibit strong near band edge emission at 3.29eV with negligible deep level emission. The PL peak at 3.29eV can be primarily attributed to the free exciton emission, though recombination from DAP also contributes to the peak formation. Shown in figure 3.6 (b), the 77K PL spectrum of the undoped ZnO nanotips has a dominant NBE emission around 3.37 eV, which is due to the free excitonic transition. For ZnO nanowires, the dominance of free exciton emission is rarely observed in a low temperature PL spectrum [80, 87]. The quench of free excitonic emission has been ascribed to localization of free exciton by intrinsic defects and impurities. Bound-exciton transitions, mostly donor-related, dominate the emission spectra, which

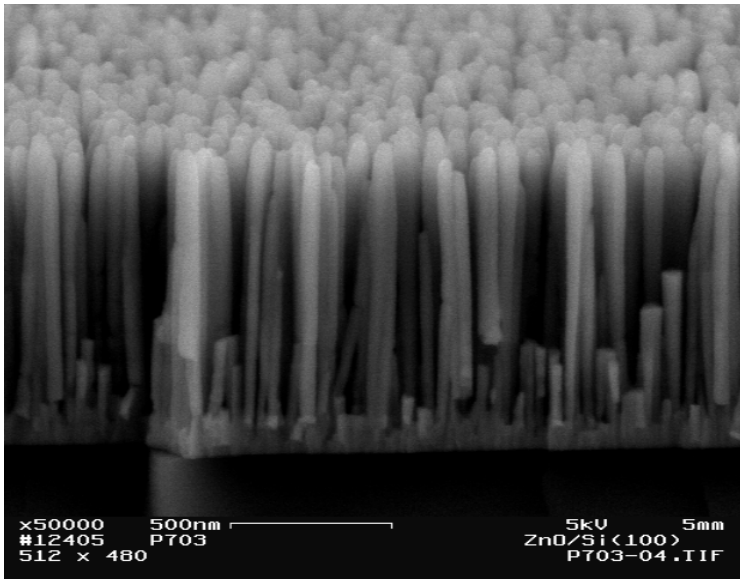

Figure 3.4. FESEM image of ZnO nanotips grown on Si substrate.

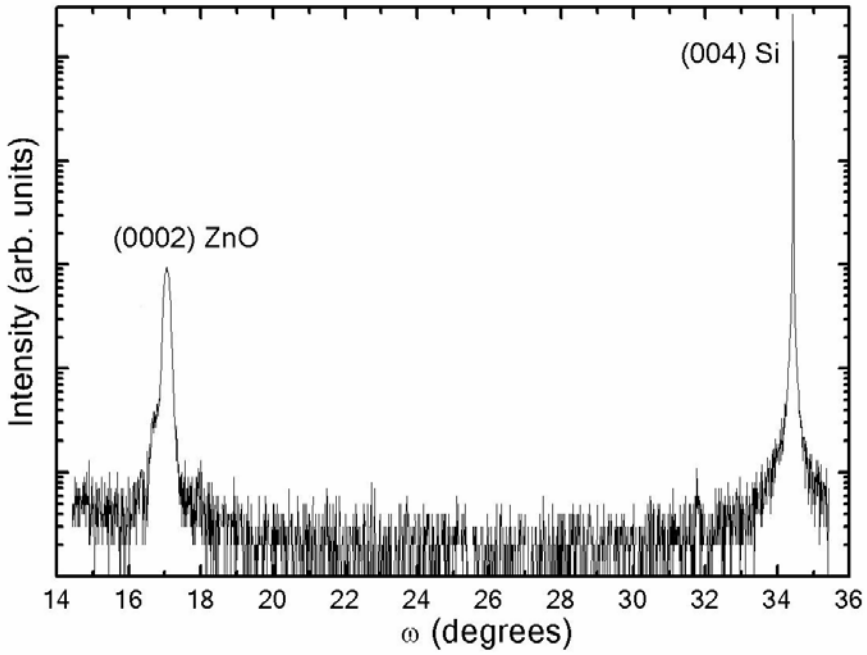

Figure 3.5. XRD pattern of ZnO nanotips grown on Si substrate.

primarily result from a high background carrier concentration. The presence of the dominant free excitonic emission confirms high purity and a low defect density of ZnO nanotips grown on Si substrate using MOCVD.

In figure 3.6 (b), a second strong peak occurs around 3.36 eV, which has a slightly lower energy than free exciton emission. It is related to bound-exciton emission involving neutral-donor-like complex. Additionally, a PL transition at 3.32 eV is observed. It could be assigned to the bound-exciton emission from donor-acceptor pair (DAP). It is also noted that up to three LO-phonon replicas exhibit at the low energy tail of the 3.32 eV peak. The results indicate that the undoped ZnO nanostructures grown on Si have good morphology and crystallinity.

3.1.3 ZnO Nanotips Grown on GaN

ZnO nanotips can be grown on crystalline GaN/c-plane sapphire substrate following an epitaxial relationship. The GaN/c-sapphire template was prepared by depositing a GaN epitaxial film (1-2μm thick) using MOCVD on a c-Al_2O_3 substrate with a conventional low temperature GaN buffer layer followed by high temperature (1080°C) bulk GaN growth. Prior to the ZnO nanotip growth, the GaN template was ultrasonically cleaned in acetone, methanol and a diluted 1:1 HCl solution, and then rinsed with deionized water. We reduced the oxygen gas exposure time before the growth in order to reduce the surface oxidation at the ZnO/GaN interface. Figure 3.7 shows a FESEM image of ZnO nanotips grown on GaN/c-Al_2O_3 template. The ZnO nanotips are

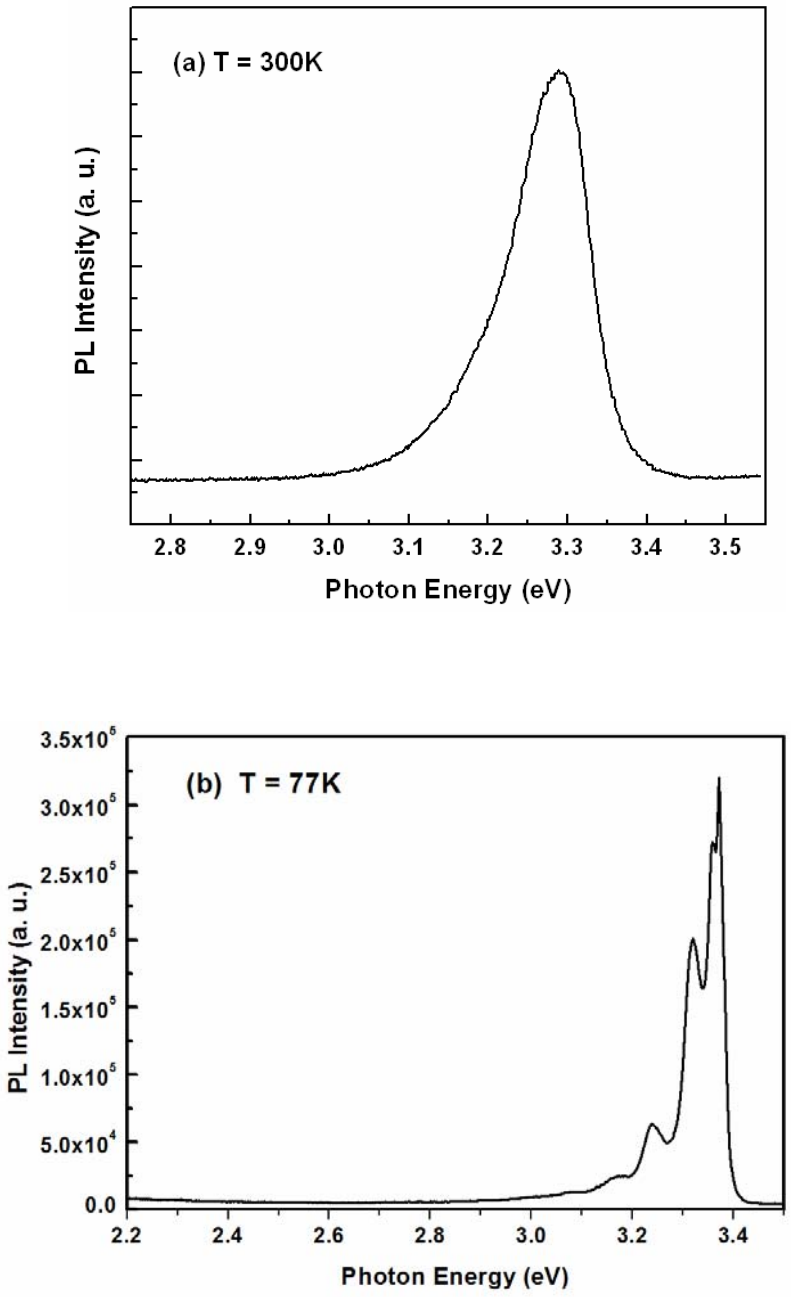

Figure 3.6. (a) Room temperature and (b) 77K PL spectra of ZnO nanotips grown on Si.

uniformly distributed over the entire substrate surface. These nanotips were found to be well oriented with the c-axis normal to the substrate surface. The nanotips have a diameter of 40-60nm at the bottom and a height of ~ 620nm. Inset of figure 3.7 shows a high resolution TEM image of a single crystalline ZnO nanotip.

To determine the epitaxial relationship between ZnO nanotips and GaN, XRD θ-2θ and φ scans were investigated. Figure 3.8 (a) shows a θ-2θ scan of ZnO nanotips grown on GaN/c-Al_2O_3. Only ZnO (0002) and GaN (0002) peaks are observed, indicating that these nanotips are preferentially oriented along the c-axis, normal to the basal plane of the GaN/c-sapphire template. Figure 3.8 (b) shows the in-plane φ scan carried out along {10-13} family of planes for ZnO. The hexagonal symmetry of ZnO can be seen from three equally spaced (60° apart) peaks in the φ scan from 0° to 180°. The XRD patterns confirm that (10-13) ZnO || (10-13) GaN, resulting in an epitaxial relationship between ZnO and GaN of (0002) ZnO || (0002) GaN and (10-10) ZnO || (10-10) GaN. The formation of well-aligned ZnO nanotips on (0001) GaN substrates results from a 1-D growth governed by the growth habit of ZnO. ZnO and GaN are closely lattice-matched and both have the wurtzite-type structure. During the initial MOCVD growth, ZnO nuclei are epitaxially grown on the GaN film. Subsequent columnar growth of ZnO nanotips is a self-assembling process. The growth rate along the c-axis is the highest due to the difference in surface relaxation energies between (0001) and (000-1) planes.

Figure 3.9 (a) and figure 3.9 (b) are room temperature and 77K PL spectrum of ZnO nanotips grow on GaN, respectively. It is noted that PL spectra of ZnO nanotips grown on GaN has essentially identical shape and peak position as those grown on Si (figure 3.8). At room temperature, ZnO nanotips exhibit strong NBE free excitonic

emission at 3.29eV with negligible deep level emission. A free excitonic peak around 3.37 eV is observed in the 77K PL spectrum. The presence of free excitonic emission at room temperature and 77K confirms a low defect density of ZnO nanotips grown on GaN substrate. A second strongest peak at 3.36 eV can be attributed to neutral-donor bound-exciton emission. Additionally, the peak at 3.32 eV could be assigned to the recombination from DAP. It is also noted that three LO-phonon replicas exhibit at the low energy tail of the 3.32 eV peak. The results indicate that ZnO nanotips grown on GaN have good morphology and crystallinity.

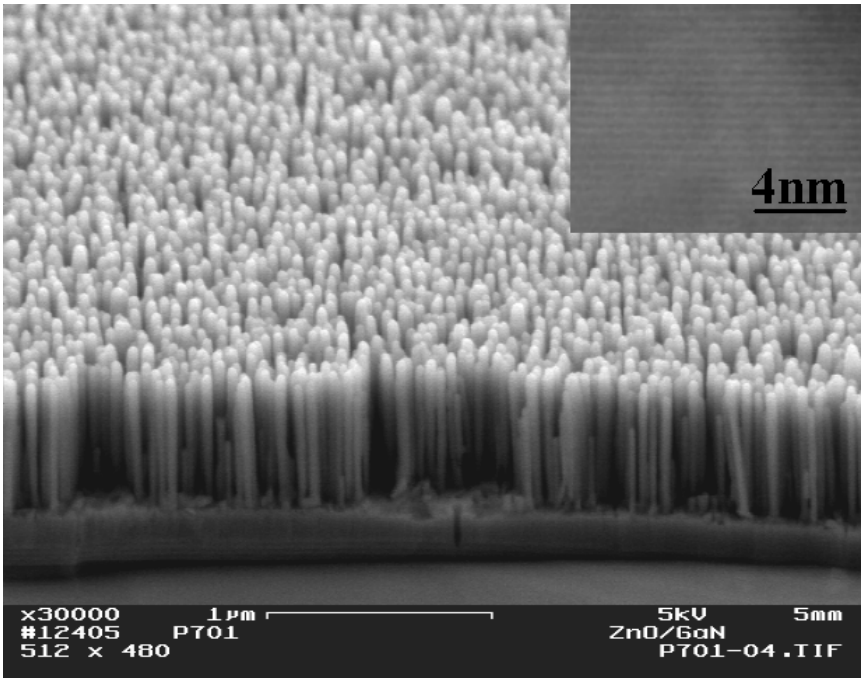

Figure 3.7. FESEM image of ZnO nanotips grown on an epitaxial GaN/c-sapphire substrate. Inset is a high resolution TEM image of a single crystalline ZnO nanotip showing lattice fringes. The c-axis of ZnO is aligned normal to the substrate surface, along the vertical direction.

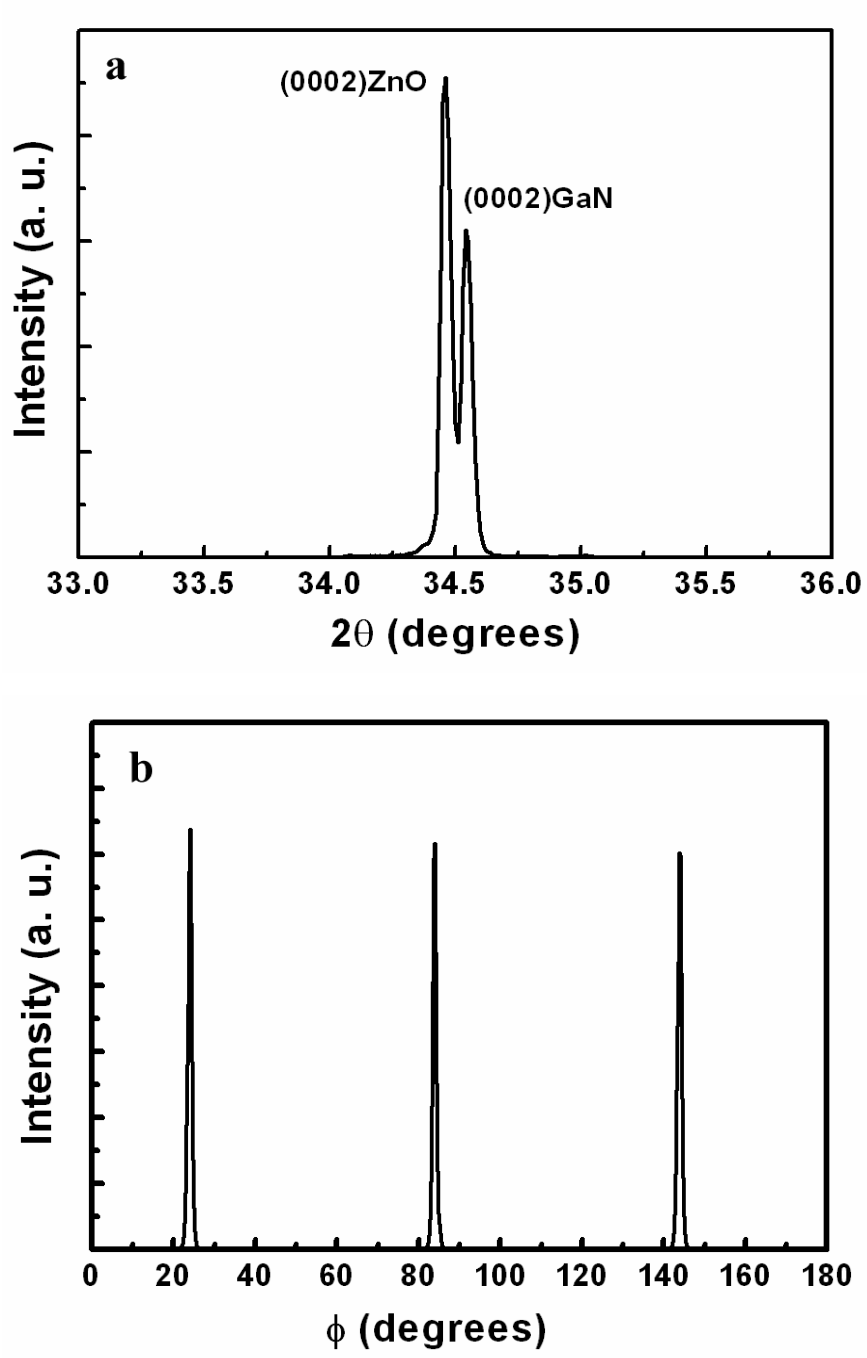

Figure 3.8. XRD patterns of (a) θ-2θ scan of ZnO nanotips on an epitaxial GaN/c-sapphire substrate; (b) in-plane φ scan carried out along {10-13} family of planes for ZnO.

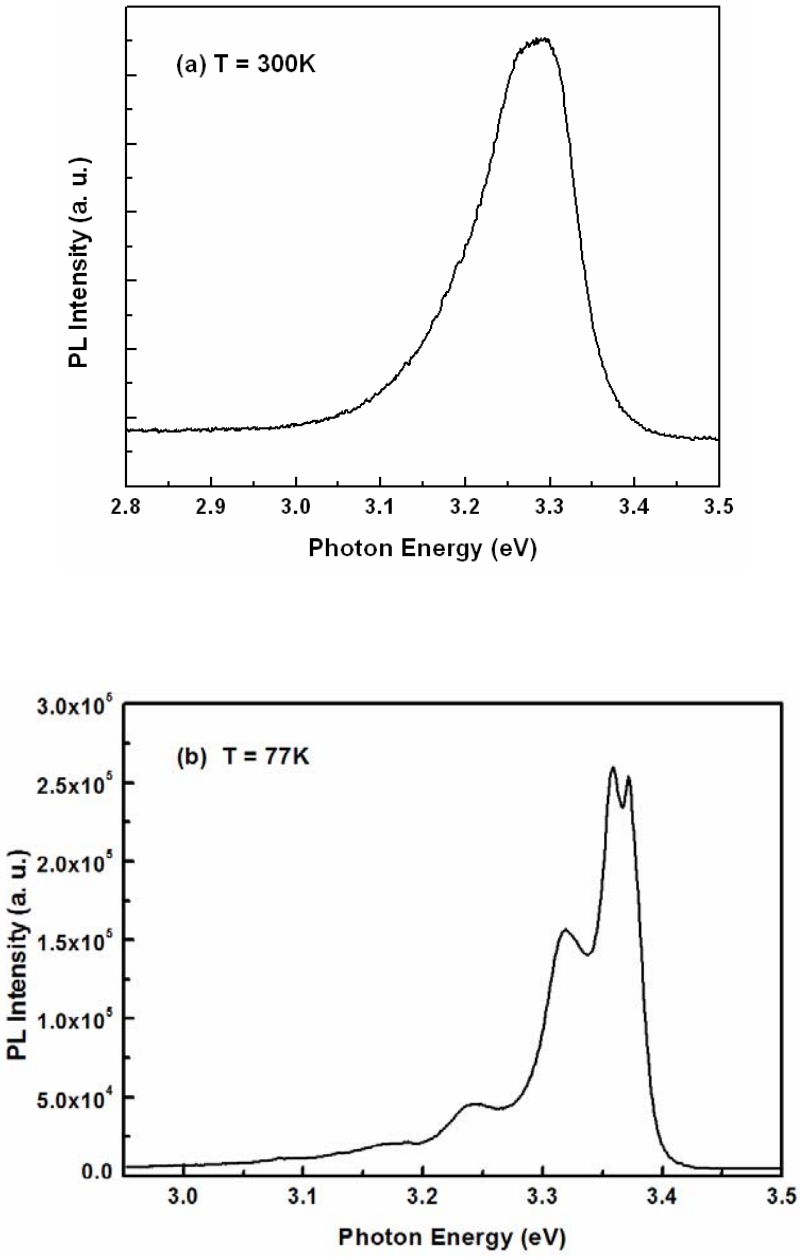

Figure 3.9. (a) Room temperature and (b) 77K PL spectra of ZnO nanotips grown on GaN.

3.2 *In-situ* Ga Doping

3.2.1 Growth and Structural Characterizations

We have grown ZnO nanotips with different Ga doping levels on fused silica substrates using MOCVD. Triethylgallium (TEGa) was used as the Ga metalorganic sources for n-type doping of ZnO. The Ga/Zn mole ratio was altered from 10^{-4} to 10^{-2} during the Ga-doped ZnO film growth. Epitaxial ZnO films were simultaneously grown on $(01\bar{1}2)$ r-sapphire substrates to serve as reference samples for doping information of the ZnO nanotips. The thickness of epi-ZnO film is ~ 360nm. No thickness variation was observed for different Ga doping concentration. The resistivities of the epi-ZnO films were characterized using the four-point-probe method. Figure 3.10 (a) shows the measured resistivities of Ga-doped epitaxial ZnO films versus Ga/Zn mole ratios. Shown in figure 3.10 (b) is a FESEM image of Ga-doped ZnO nanotips grown on fused silica substrate. Inset (c) shows the top view of the ZnO nanotips. The diameter of the bottom of nanotips is in the range of 40-60nm and the height is ~ 850nm, giving an aspect ratio of ~17:1. Shown in figure 3.11 (c) is a dark-field transmission electron microscope image of the Ga-doped ZnO nanotip along the $[2\bar{1}\bar{1}0]$ zone axis. The selected area electron diffraction and the high-resolution images are shown in insets (a) and (b), respectively. The electron microscopy confirms the single crystal quality of the Ga-doped ZnO nanotips. High-resolution lattice images show a single crystalline nanoscale tip. No significant structural change between undoped and Ga-doped ZnO nanotips is observed.

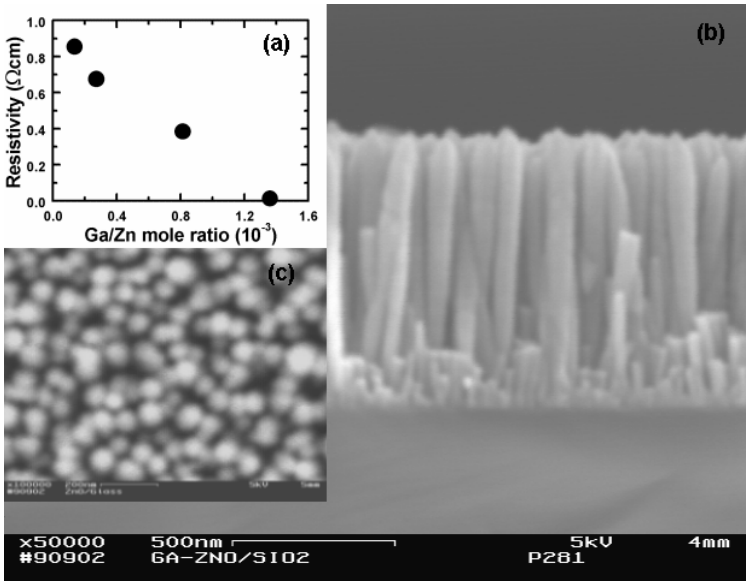

Figure 3.10. (a) Measured resistivity of Ga-doped epitaxial ZnO films versus Ga/Zn mole ratios. FESEM images of Ga-doped ZnO nanotips grown on fused silica substrate (b) cross-sectional view, and (c) top view.

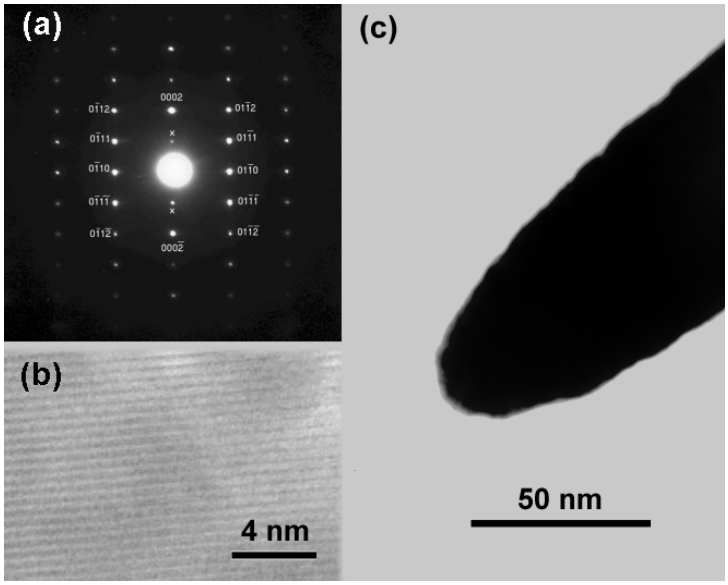

Figure 3.11 (a) Selected area diffraction pattern of a single Ga-doped ZnO nanotip along the [$2\bar{1}\bar{1}0$] zone axis; (b) an image of a single crystalline tip from high-resolution transmission electron microscope (HRTEM); and (c) dark field TEM image of a single Ga-doped ZnO nanotip.

3.2.2 Optical Characterizations

Figure 3.12 (a) shows the room temperature PL spectra of undoped and Ga-doped ZnO nanotips. Curve 1 is for the undoped ZnO nanotips with a reference resistivity, ρ_{ref}, of 40 Ωcm, curves 2, 3 and 4 correspond to Ga-doped ZnO nanotips with ρ_{ref} of 0.58 Ωcm, 4.0×10^{-3} Ωcm and 3.0×10^{-3} Ωcm, respectively. It has been reported that due to excess exciton-impurity and crystalline defect scattering, there exists a deep-level emission around 2.4 eV in the undoped ZnO nanowires or whiskers. The negligible deep-level emission in figure 3.12 (a) suggests good optical quality of the Ga-doped ZnO nanotips grown on the amorphous silica substrates. For ZnO nanotips, the near band-edge recombination monotonically increases with ρ_{ref} is decreased to 4×10^{-3} Ωcm when progressively increasing Ga doping (curves 1, 2 and 3 in figure 3.12 (a)). With a further increase in the Ga doping level, the peak intensity starts to decrease (curve 4 in figure 3.11 (a)). It is also noticed that half-width broadening can be seen in the spectra when ρ_{ref} is at 4×10^{-3} Ωcm or less (curves 3 and 4 in figure 3.12 (a)).

Figure 3.12 (b) shows the 77K PL spectra of the same set of samples. At 77K, undoped ZnO nanotips display a dominant near band-edge emission around 3.36 eV, which is slightly lower than the free exciton emission energy near 3.37 eV, and lies in the spectral range of multiple emission lines associated with neutral donor bound exciton recombination. This near band-edge emission may arise from bound exciton emission involving donor-like complexes. Meanwhile, two weak shoulders appear on the low energy tail of the dominant 3.36 eV peak. These shoulders disappear gradually with Ga incorporation giving rise to a new dominant emission line around 3.35 eV. This 3.35 eV

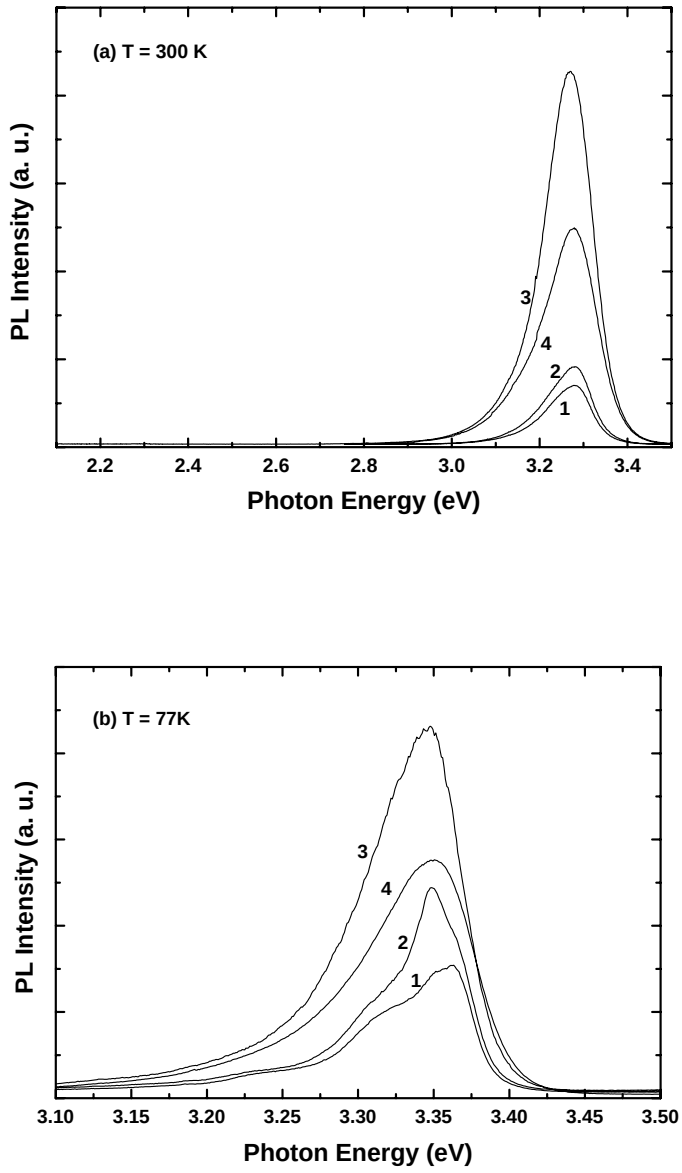

Figure 3.12. (a) Room temperature PL spectra of undoped and Ga-doped ZnO nanotips. (b) 77K PL spectra of undoped and Ga-doped ZnO nanotips. Curve 1 is for the undoped ZnO nanotips with a reference resistivity, ρ_{ref}, of 40 Ωcm, curves 2, 3 and 4 correspond to Ga-doped ZnO nanotips with ρ_{ref} of 0.58 Ωcm, 4.0×10^{-3} Ωcm and 3.0×10^{-3} Ωcm, respectively.

PL line shows the same trend as the main peak at room temperature in terms of the intensity and half-width versus doping. Such doping-related behavior has been reported in low temperature PL spectra of Ga-doped ZnO epitaxial films [109], where a Ga donor bound exciton complex has been proposed to be responsible for the increase of PL intensity from Ga doping. Figure 3.12 (b) suggests the 3.35 eV peak could be related to the Ga donor in view of its contribution to the near band-edge emission.

The integrated PL intensity increases by a factor of 4.5 when the reference doping concentration increases from 5.0×10^{18} to 8.9×10^{19} cm^{-3} and then decreases at the highest reference doping concentration of 3.7×10^{20} cm^{-3}. The luminescence efficiency in Ga doped ZnO is approximately the ratio of radiative to nonradiative recombination rate $\frac{R_r}{R_{nr}}$. The nonradiative recombination rate R_{nr} is proportional to:

$$R_{nr} \propto N_T p \tag{3.1}$$

where R_r and R_{nr} is radiative recombination rate and nonradiative recombination rate, respectively, p is the nonequilibrium minority carrier concentration and N_T is the concentration of nonradiative trap centers.

The radiative recombination rate R_r is proportional to:

$$R_r \propto N_D p \tag{3.2}$$

where N_D is the Ga donor concentration. As a result, the ratio of radiative to nonradiative recombination rate is approximately proportional to N_D/N_T.

At low or moderate Ga doping levels, the increase of PL intensity is primarily caused by the increase of the impurity emission due to an increased Ga dopant concentration, while the trap center concentration does not increase proportionally during

the Ga-doped growth. In heavily Ga-doped ZnO nanotips, the competition between the radiative and nonradiative transitions becomes prominent. Excess Ga atoms can create nonradiative recombination centers, such as impurity complexes likely involving native defects, or impurity-assisted nonradiative transition channels, resulting in a reduction of the near band-edge luminescence. At a further higher Ga concentration ($> 10^{21}$ cm^{-3}), the NBE PL emission is completely quenched, showing nonradiative channels dominate at very high Ga incorporation.

As the 3.35 eV peak introduced by Ga doping follows the same half-width versus doping trend as observed at room temperature, the linewidth broadening in Ga-doped ZnO nanotips might result from potential fluctuations in the nano-structures that arise from random microscopic distribution of the dopants.

To further analyze the optical transition process in Ga-doped ZnO nanotips, we have compared room temperature PL spectra with optical absorption spectra. Figure 3.13 show normalized photoluminescence spectra of Ga-doped ZnO nanotips grown on fused silica substrates with different doping concentration (left-hand side). For comparison, normalized absorption spectra are shown on the right-hand side. Absorption occurs between energy states in valence band and the Fermi level in conduction band, while emission occurs between transitions from a donor band to valence band or an acceptor band. The room temperature PL peak (3.27 eV) in Ga-doped ZnO nanotips grown on glass can be assigned to the recombination of donor-acceptor pair (DAP).

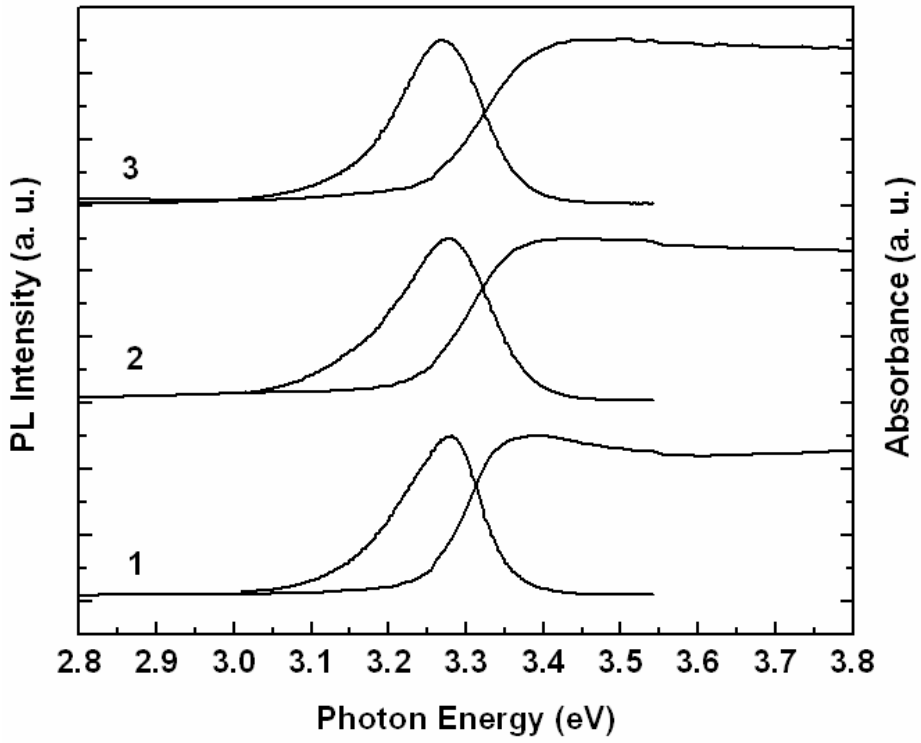

Figure 3.13. Room temperature normalized photoluminescence spectra (left side) and absorption spectra (right side) of Ga-doped ZnO nanotips. Curves 1, 2 and 3 are Ga-doped ZnO nanotips with ρ_{ref} of 0.58 Ωcm, 4.0×10^{-3} Ωcm and 3.0×10^{-3} Ωcm, respectively.

Table 3.1 lists the FWHM of room temperature PL spectra for Ga-doped ZnO nanotips at different doping levels. The reference carrier concentration was measured by Hall-effect measurements in the van de Pauw configuration.

Table 3.1: FWHM of room temperature PL spectra for Ga-doped ZnO nanotips at different doping levels.

Reference Resistivity (Ωcm)	**Reference Doping Concentration (cm^{-3})**	**FWHM of RT PL (meV)**
0.58	5.0×10^{18}	119
4.0×10^{-3}	8.9×10^{19}	139
3.0×10^{-3}	3.7×10^{20}	153

Shown in table 3.1, the reference doping concentration increases from 5.0×10^{18} to 3.7×10^{20} cm^{-3}, and FWHM of NBE PL peak increases from 119 to 153 meV. Slope changes in the absorption edge reflect the Fermi distribution of the carriers after n-type doping. Potential fluctuation is caused by random distribution of the dopant atoms in the material. The photogenerated carriers could be localized under the potential fluctuation. Increased FWHM with doping concentration is due to enhanced localization of with an increase of randomness.

Band-gap shift in n-doped ZnO nanotips is a competition between band-gap widening known as the Burstein-Moss effect and band-gap renormalization due to many-body interactions. In a heavily doped semiconductor, the donor electrons occupy states at

the bottom of the conduction band. Since Pauli exclusion principle prohibits states to be doubly occupied, the lowest states in the conduction band are blocked. The optical transitions between the Fermi level in the conduction band and the valence band shows a shift towards higher energy.

The other process that counteracts the bandgap widening is band-gap renormalization caused by many-body Coulomb effects. The Ga donor electrons are under Coulomb repulsion, and effectively each electron is surrounded by a hole, leading to a lowering of the energy of the electron. In addition, band tailing is introduced by interaction between electrons and impurities. Similarly, the holes in the valence band is attracted by the donor electrons and repelled by the positively charged donor ions, thus an up-shift of the valence band occurs. Since ZnO is a polar semiconductor, anions and cations are spatially displaced in the host atoms. An electron attracts the positively charged cation, and forms a particle pair known as polaron. The band-gap narrowing caused by polaron depends on a variety of parameters such as effective mass, dielectric constants, and phonon interaction.

In our case, band-gap widening Burstein-Moss effect dominates over other effects of band-gap renormalization in the Ga-doped ZnO nanotips. The Mott critical density was reported to be $n_M \sim 7 \times 10^{19}$ cm^{-3} in ZnO film [110, 111], beyond which the Fermi level enters the conduction band. We suggest that band filling takes place in the Ga-doped ZnO nanotips for $n_D > n_M$.

3.2.3 Electrical Characterization

Nanostructure characterization techniques, such as scanning probe microscopy (SPM), have lead to visualization of nanostructures down to an atomic scale. Among these techniques, conductive-tip atomic force microscopy (C-AFM) is a useful method to explore nanoscale electrical characteristics (such as carrier transport) in nanoscale materials. C-AFM operates in the near-field mode, and is sensitive to the variation of the tip-sample separation. The electron tunneling mechanism is utilized to control the distance between sample and tip, where the tunneling current depends exponentially on the tip-sample separation, making it capable of an atomic scale resolution (~ 0.1 nm).

Current-voltage (I-V) spectra were taken at room temperature using a JEOL vacuum scanning tunneling microscope/AFM system that was operated in a conductive tip-AFM mode. Multiple I-V spectra on different ZnO nanotips as well as calibration experiments were performed to ensure reproducibility. Figure 3.17 shows the tunneling I-V spectra for both undoped and Ga-doped ZnO nanotips. Curves 1, 2, and 3 correspond to the spectra of undoped and Ga-doped ZnO nanotips with ρ_{ref} of 40 Ωcm (undoped), 0.58 Ωcm (Ga-doped), 4.0×10^{-3} Ωcm (Ga-doped), respectively.

The asymmetry in the rising slopes of the conduction and valence bands show that the "undoped" ZnO nanotips are intrinsically n-type, in agreement with the observations in the as-grown epitaxial ZnO films. Significantly steeper rising slopes in I-V spectra are clear in Ga-doped ZnO nanotips (curves 2 and 3) in comparison with those in the undoped nanotips (curve 1). These confirm the conductivity enhancement in ZnO nanotips due to Ga doping.

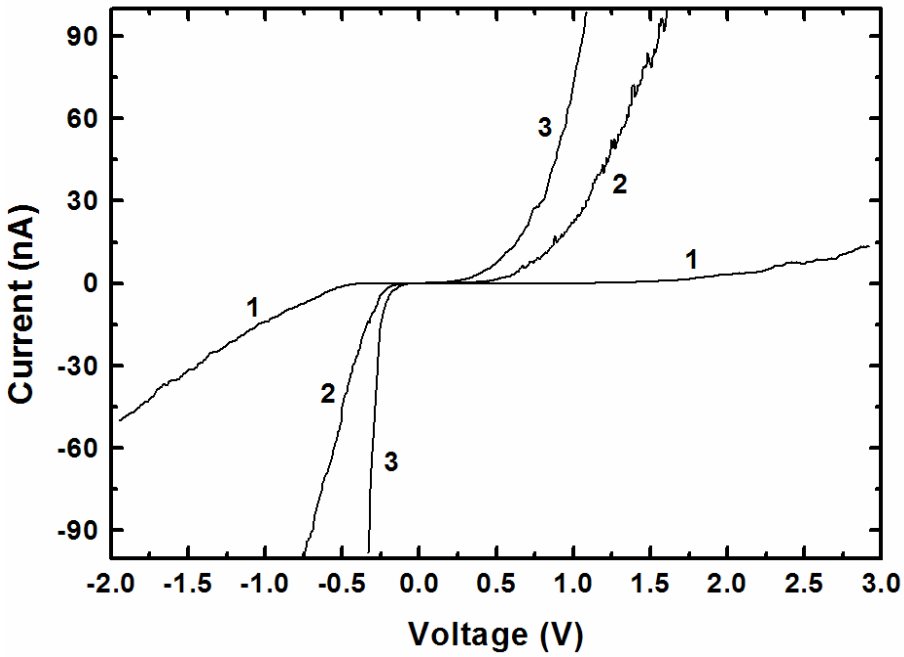

Figure 3.14. Current-voltage spectra for the undoped and Ga-doped ZnO nanotips, where curves 1, 2, and 3 correspond to the spectra of undoped and Ga-doped ZnO nanotips with a reference resistivity of 40 Ωcm (undoped), 0.58 Ωcm (Ga-doped), 4.0×10^{-3} Ωcm (Ga-doped), respectively.

3.3 Summary

Structural and optical properties of ZnO nanotips grown on glass, Si, and GaN substrates were investigated. They are found to be single crystalline and oriented along the c-axis. ZnO nanotips grown on a crystalline GaN substrate follows an epitaxial relationship (0002)ZnO || (0002)GaN and (10-10)ZnO || (10-10)GaN. While on an amorphous glass substrate, ZnO nuclei are formed randomly. PL spectra of ZnO nanotips are dominated by near-band-edge emission with negligible deep-level emission. We do not observe explicit dependence of PL characteristics on the specific substrate. As an example, the excitonic emissions of ZnO nanotips grown on GaN substrates have been studied in more details, which will be described in Chapter 4.

In-situ Ga-doped ZnO nanotips were demonstrated and characterized. Ga-doped ZnO nanotips remain single crystalline. We do not observe any significant structural change between undoped and Ga-doped nanotips. At low or moderate Ga doping levels, the increase of PL intensity is caused by the increase of the impurity emission due to an increased Ga dopant concentration. In heavily Ga-doped ZnO nanotips, excess Ga atoms create nonradiative recombination centers, resulting in a reduction of the near band-edge luminescence. Increased half-width of PL spectrum is observed with an increased doping level, primarily due to doping induced potential fluctuation in the material. At a high Ga doping level, Burstein-Moss effect dominates, leading to blueshift of the absorption edge. Current-voltage characteristics of the ZnO nanotips are measured by conductive-tip atomic force microscopy, which show the conductivity enhancement due to Ga doping.

Chapter 4. Temperature Dependent Photoluminescence Studies of ZnO Nanotips

Photoluminescence (PL) is a nondestructive and powerful tool to characterize optical properties of semiconductor. PL is widely used to study fundamental recombination process in the material, such as impurity levels and radiative and nonradiative defect dynamics, and to characterize crystalline quality. The nanostructured materials possess interesting unique optical and electrical properties, which differ from those of corresponding bulk materials. ZnO nanotips are considered as a subwavelength assembly consisting of ZnO and air gaps. The substantial ionic character and polar nature of Zn-O bond produce long-range polarization fields in the lattice vibrations, and strong optical phonon-photon interaction is observed. Due to a large surface to volume ratio, surface states of ZnO nanowires grown by the VLS technique generate surface excitonic features at low temperature (~ 3.366eV at 7K), and act as nonradiative recombination centers via ionization of the surface states [112]. Knowledge of intrinsic and extrinsic optical transitions, carrier recombination lifetime in ZnO nanotips is critical for development of ZnO nanostructure based novel electrical and optical devices.

4.1 Temperature Dependent Steady-state Photoluminescence

Optical properties of ZnO nanotips have been characterized by a temperature dependent steady-state PL spectroscopy. The temperature dependent steady-state PL setup consists of a 325nm continuous-wave (CW) Cd-He laser, a SPEX 0.5m grating spectrometer with a 1200 grooves/mm grating blazed at 330nm, and a photon counting unit with a photomultiplier (PMT). The operation voltage of the PMT is 1360V. A

continuous-flow liquid He optical cryostat is used to vary the sample temperature from 4K to room temperature. Figure 4.1 illustrates a schematic diagram of a UV temperature-dependent steady-state PL system. The laser beam is focused on the sample at a spot size of <1mm. The incident light is at an angle of ~ 45° from the surface normal to reduce the reflection. The luminescence emitted from the sample is collected and collimated by a 2" diameter biconvex lens. Another 2" diameter biconvex lens is used to focus the collimated light onto the slits of the spectrometer, where the F number is designed to match that of the spectrometer. The matched F number is required to reduce spurious luminescence and improve the collection efficiency. The wavelength reading of the spectrometer is calibrated by the multi-lines (5460.7A, 5769.6A, 5790.7A, etc.) of a mercury calibration lamp. For low temperature measurements, a continuous-flow liquid He optical cryostat was used to cool the samples. The optical cryostat is connected to a two-stage pump system, which consists of a turbo-molecule pump and a backed rough mechanical pump, to achieve a vacuum level of 10^{-5} - 10^{-6} Torr. The spectral resolution of the CW PL setup was better than 0.5meV.

Shown in figure 4.2 is the 4.4 K PL spectrum of ZnO nanotips grown on GaN. We observe two strong and sharp bound exciton peaks at 3.369 eV (denoted by D^0X1) and 3.364 eV (denoted by D^0X2). These emissions can be assigned to excitons bound to neutral donors or neutral donor-like defect complexes [113]. The strongest peak at 3.364 eV has a full width at half maximum of ~ 2 meV, comparable to the value obtained from ZnO epitaxial films grown on GaN by plasma assisted MBE [114]. Another prominent excitonic peak is seen at 3.380 eV, which is identified as the free A exciton emission

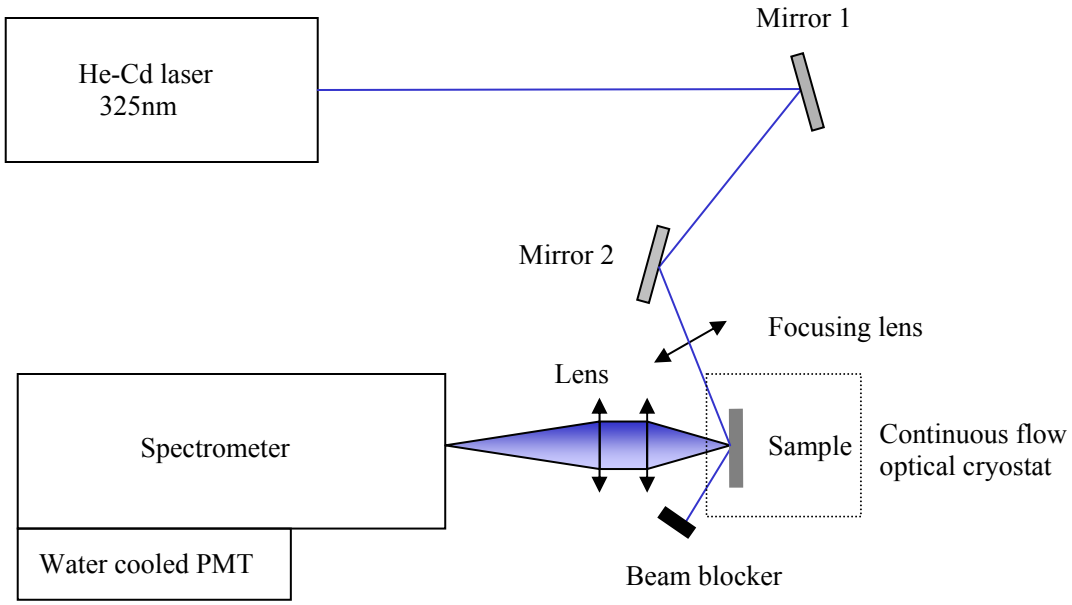

Figure 4.1. Schematic diagram of a UV temperature dependent PL setup.

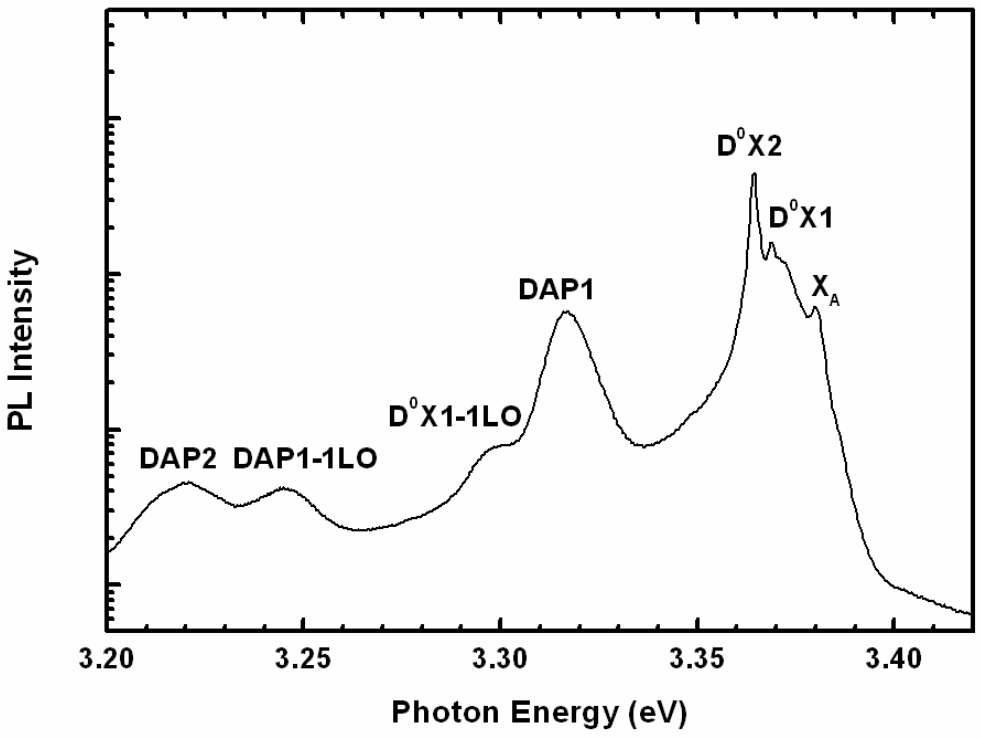

Figure 4.2. PL spectrum of ZnO nanotips measured at 4.4K in logarithmic scale. The free exciton emission is clearly seen at 3.380 eV (X_A). Two sharp bound exciton emissions are observed at 3.369 eV (D^0X1) and 3.364 eV (D^0X2), respectively.

(denoted by X_A). Below 10K, the free exciton peaks may not be observed due to localization of the free excitons by defects and impurities. The free exciton emission in figure 4.2 indicates a low defect and impurity density in these nanotips. A weak shoulder is also resolved at ~ 3.370 eV, which could be attributed to the emission from donor associated bound exciton, though no specific donor has been identified. In addition to free and bound excitons, the PL lines observed at 3.317 and 3.221 eV can be presumably assigned to zero phonon lines of donor-acceptor-pair (DAP) emissions [87], denoted by DAP1 and DAP2, respectively. The DAP1 emission is followed by LO phonon replicas (denoted by DAP1-1LO) with an energy separation of 72 meV. A deep level emission band (~ 2.4 eV) is not observed in these ZnO nanotips.

Temperature dependent PL spectra from 4.4 to 300K are shown in figure 4.3. It is noted that when temperature increases from 18 to 300K, the emissions show a red shift. Above 50K, the free exciton emission becomes the strongest compared to the relative intensities of D^0X1 and D^0X2. D^0X1 emission accompanied by an LO phonon replica (denoted by D^0X1-LO) is thermally annihilated above 100K, while D^0X2 emission is quenched above 150K. This infers that thermal ionization of D^0X1 and D^0X2 could lead to creation of free excitons and neutral donors. Despite thermal broadening and strong exciton-LO-phonon coupling, free exciton transition is dominant up to 300K when the PL spectra between 200-300K are compared. This indicates high purity and a low background carrier concentration of the ZnO nanotips. The high optical quality of ZnO nanotips grown on (0001)GaN substrates can be attributed to a low defect density in the 1-D grown nanotips, where close lattice-match and stacking order match between ZnO and GaN would lead to a lower dislocation density at the ZnO/GaN interface.

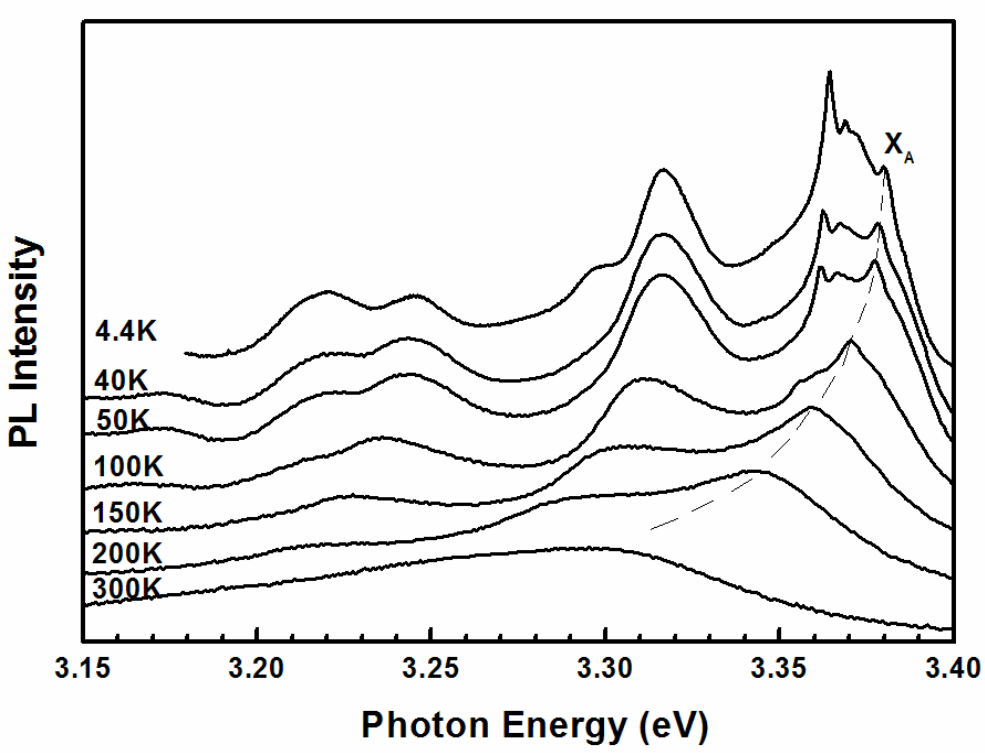

Figure 4.3. Temperature dependent PL spectra of ZnO nanotips. The PL intensity of each curve is plotted in logarithmic scale.

To analyze the excitonic emissions from ZnO nanotips grown on GaN, the Arrhenius plots for D^0X1, D^0X2, and X_A are shown in figure 4.4. The intensities of D^0X1 and D^0X2 drop independently when temperature increases, suggesting that they originate from different neutral donors.

The temperature dependent excitonic emission quenching observed can be described using a simplified model based on the rate equation, in which up to N nonradiative channels are considered:

$$\frac{\partial n}{\partial t} = G - \frac{n}{\tau_R} - \sum_{i=1}^{N} \frac{n}{\tau_{NR_i}} \tag{4.1}$$

where n is the density of photoexcited excitons, G is the generation rate of photoexcited excitons, τ_R is the radiative lifetime of the excitons, and τ_{NRi} is the nonradiative lifetime corresponding to the ith nonradiative recombination channel. Assuming the nonradiative recombination process is thermally activated, the nonradiative lifetime of the ith nonradiative recombination channel can be expressed by:

$$\tau_{NR_i} = \tau_0 e^{\frac{E_{Ai}}{kT}} \tag{4.2}$$

where E_{Ai} denotes the activation energy of the ith nonradiative recombination channel, τ_0 is a characteristic time constant. The thermal activated nonradiative recombination processes could include Fermi-Dirac distribution of carriers, and thermal activation of nonradiative centers, etc.

In a steady state, $\frac{\partial n}{\partial t} = 0$, PL intensity is proportional to $\frac{n}{\tau_R}$. The Arrhenius plots of PL emission intensity can be fitted with multiple nonradiative decay channels as:

$$I(T) = \frac{I(0)}{1 + \sum_i B_i e^{-\frac{E_{Ai}}{kT}}} \qquad (4.3)$$

where I(0) and I(T) are the PL intensity at 0 K and T (> 0K), respectively, B_i is a fitting constant corresponding to the *i*th nonradiative channel, which is inversely proportional to the radiative transition rate, and E_{Ai} is the thermal activation energy in the *i*th channel of nonradiative decay.

As shown in figure 4.4, the temperature dependence of PL intensities for D^0X1, D^0X2, and X_A emissions are well described with the two-channel dissociation model of Eq. (4.3). From energy separations between D^0X1 and X_A, and D^0X2 and X_A lines, the exciton localization energies, i. e. the energy required to remove the exciton from the specific neutral donor, for D^0X1 and D^0X2, can be deduced to be 11 and 16 meV, respectively. These agree well with the thermal activation energies of D^0X1 (11 meV) and D^0X2 (15 meV) obtained in the second region of the bound exciton thermal dissociation process.

A bound exciton complex (BEC) is formed via excitons bound to various types of point defects, such as an ionized donor, a neutral donor, and a neutral acceptor. The binding energy of an exciton to a neutral donor is proportional to the binding energy of an electron to the specific donor, known as Haynes rule:

$$E^b_{D^oX} = \alpha E^b_D + \beta \qquad (4.4)$$

where $E^b_{D^oX}$ is the exciton binding energy, E^b_D is the donor binding energy, and α, β are proportionality constants. According to an empirical Haynes' relationship in ZnO [81], α is 0.3, and β is 0.46. The donor binding energies, i. e. the energy binding the electron to the impurity donor, for D^0X1 and D^0X2 are calculated to be ~41 and 54 meV,

respectively. The chemical origins of these shallow donors have not been identified in ZnO nanotips.

Small activation energies of 3, 4, and 5meV have been obtained for X_A, D^0X1, and D^0X2 in the first region of the bound exciton thermal dissociation process. A rapid decay of luminescence intensity with increasing temperature (T < 100K) shows that temperature activated nonradiative processes could be dominated in these ZnO nanotips. We suspect that small activation energy (3, 4, and 5meV for X_A, D^0X1, and D^0X2, respectively) may indicate surface mediated nonradiative recombination process in the ZnO nanotips, such as surface traps due to a large surface-to-volume ratio. A surface exciton has small characteristic activation energy of 5meV [112].

We have compared temperature dependent peak intensities of X_A, D^0X1, and D^0X2 lines. When temperature increases from 4.4K to 50K, the peak intensity ratio of X_A to D^0X1 increases from 0.39 to 1.39, whereas the ratio of X_A to D^0X2 increases from 0.14 to 2.32. This suggests that D^0X1 and D^0X2 dissociate into free excitons and neutral donors due to thermal release of free excitons in the ZnO nanotips:

$$D^0X1 - D^01 + X \quad (4.5)$$

$$D^0X2 - D^02 + X \quad (4.6)$$

The 3.364 eV (D^0X2) peak in bulk ZnO has been attributed to the bound exciton emission from a neutral donor defect doublet [114]. Thermal dissociation of the 3.364 eV bound exciton leads to the creation of a free exciton and a neutral-donor-like defect-pair complex at elevated temperatures.

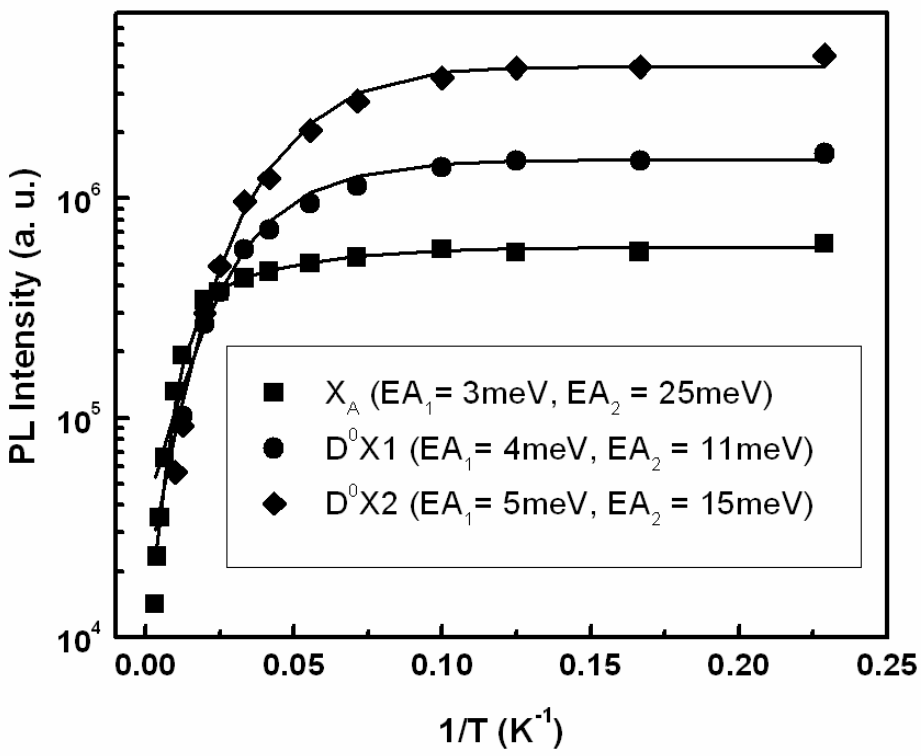

Figure 4.4. Arrhenius plots of PL intensities as a function of inverse temperature for D^0X1, D^0X2, and X_A emissions. The solid lines show the curve fitting results from Eq. (4.3).

The temperature dependence peak position of free A exciton emission is fitted to the Varshni's equation from 4.4K to 300K, giving the variation of energy bandgap versus temperature as:

$$E\,(T) = E\,(0) - \frac{\alpha T^2}{\beta + T} \tag{4.7}$$

where *E (T)*, *E(0)* are the free exciton transition energy at temperature T and 0K, respectively, α is the Varshni's thermal coefficient in eV/K, and β is approximately the Debye temperature in ZnO. The solid line in figure 5 shows the least-square fitting to Eq. (4.7). We obtain the best-fit values of *E (0)* = 3.380eV, $\alpha = 11 \times 10^{-4}$ eV/K, and $\beta = 910 \pm 15$ K. Our fitting value of β agrees well with the reported Debye temperature for ZnO (920K) [115]. The fitting result also suggests the excitonic nature of the PL transitions in these nanotips. Also shown in figure 4.6, is free and bound exciton peak position versus temperature, where peaks P1, P2, P3, P4, P5, P6, P7, P8, P9 denote emissions of X_A, D^0X1, D^0X2, DAP1, D^0X1-1LO, DAP1-1LO, DAP2, DAP1-2LO, and DAP2-1LO, respectively.

Internal quantum efficiency of ZnO nanotips is deduced based on temperature variable PL measurements. The internal quantum efficiency η_i is given by:

$$\eta_i(T) = \frac{I_R(T)}{I_0} = \frac{\frac{1}{\tau_R(T)}}{\frac{1}{\tau(T)}} \tag{4.8}$$

$$\frac{1}{\tau(T)} = \frac{1}{\tau_R(T)} + \frac{1}{\tau_{NR}(T)} \tag{4.9}$$

therefore

$$\eta_i(T) = \frac{1}{1 + \frac{\tau_R(T)}{\tau_{NR}(T)}} \tag{4.10}$$

where $I_R(T)$ is the integrated PL intensity at temperature T, I_0 is the excitation power, τ is the carrier recombination lifetime, τ_R and τ_{NR} are the radiative and nonradiative recombination lifetime, respectively.

Figure 4.7 shows the relative internal quantum efficiency (IQE) of ZnO nanotips grown on GaN measured by temperature-dependent steady-state PL. Carrier recombination processes in ZnO nanotips are quite different at low temperature and near room temperature. At low temperature (< 50K), a much sharper drop in IQE is observed; at high temperature (> 100K), IQE is almost kept as a constant. If IQE is assumed to be 100% at 6K, IQE at room temperature (300K) is ~ 3.7% for ZnO nanotips grown on GaN.

4.2 Time-resolved Photoluminescence

Time-resolved photoluminescence (TRPL) is used to characterize carrier recombination dynamics in semiconductor. The carrier recombination lifetime of ZnO has been measured by TRPL. A TRPL measurement system consists of a femtosecond (fs) Ti:sapphire laser and a frequency triple. To achieve a piecosecond temporal resolution, a time correlated single photon counting unit and a microchannel plate photomultiplier were used. The fundamental wavelength of the Ti:sapphire laser at 800nm was frequency tripled to 266nm, and used as a pulsed excitation source. The instrumental response function (IRF) of the overall TRPL system was ~9 ps. Figure 4.8 shows the room

temperature TRPL spectrum of ZnO nanotips grown on GaN measured at the near band edge emission peak of 3.29eV.

A biexponential decay function fits well with the measured PL decay profile (figure 4.8 (b)). It has a significantly reduced chi square value χ^2 of 1877 than that of a single exponential fit with χ^2 of 22160. Two time constants can be deducted to be 192 ps and 47 ps. The biexponential decay behavior suggests that two different carrier capture processes dominate, though the exact mechanisms are still unknown. A radiative lifetime of free exciton in ZnO has been calculated [116]:

$$\tau_R = \frac{2\pi\varepsilon_0 m_0 c^3}{ne^2\omega^2 f} \tag{4.11}$$

where n is the refractive index, f is the oscillator strength, ε_0, m_0, c, and e are fundamental physical constants. By using $\omega = 4.95\times10^{15}$ s^{-1} and n ~ 2.4 for ZnO, τ_R is ~ 0.91/f ns [116]. Free exciton is estimated to have a radiative lifetime >1 ns. A luminescence decay time is determined by radiative and nonraditive recombination processes following Eq. (4.9). Due to the competition between the nonradiative and radiative recombination processes, the measured PL lifetime is much shorter than the radiative lifetime. From Eqs. (4.9) and (4.10), the radiative lifetime and nonradiative lifetime are given by:

$$\tau_{NR} = \frac{\tau}{1-\eta_i} \tag{4.12}$$

$$\tau_R = \frac{\tau_{NR}(1-\eta_i)}{\eta_i} \tag{4.13}$$

By using the PL lifetime τ = 192 ps and internal quantum efficiency η_i = 3.7%, τ_R is calculated to be ~ 5.2ns, and τ_{NR} is ~ 199 ps.

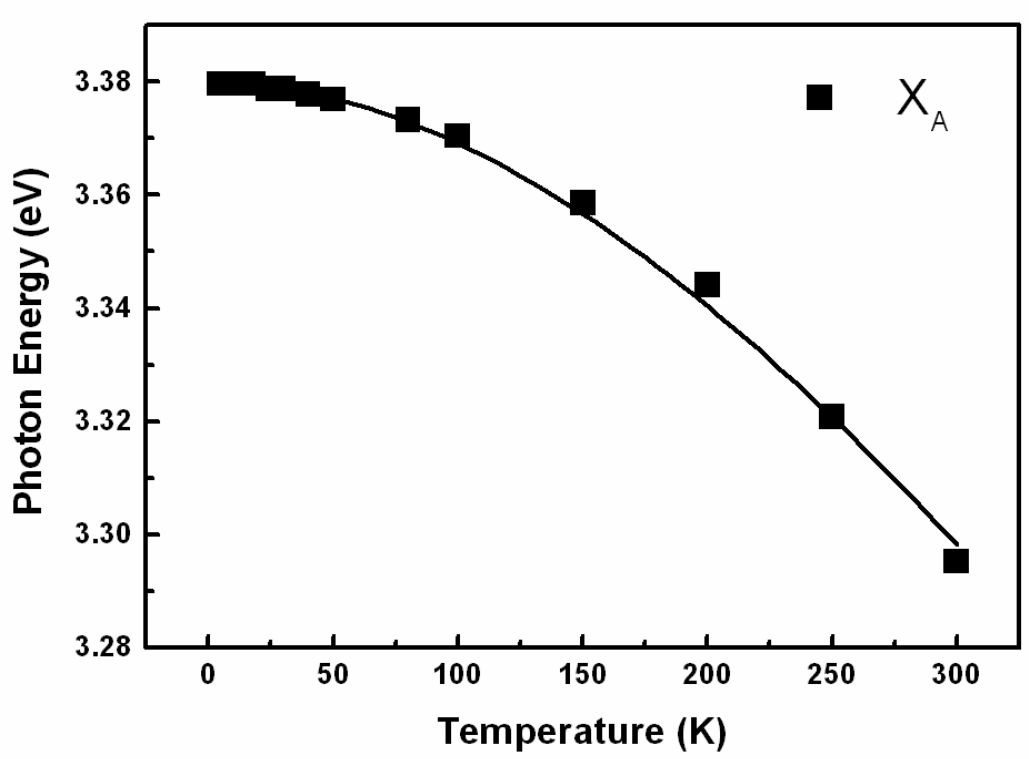

Figure 4.5. Plot of PL peak position of free A excitonic emission (X_A) as a function of temperature. The solid line is the curve fitting result according to Eq. (4.7).

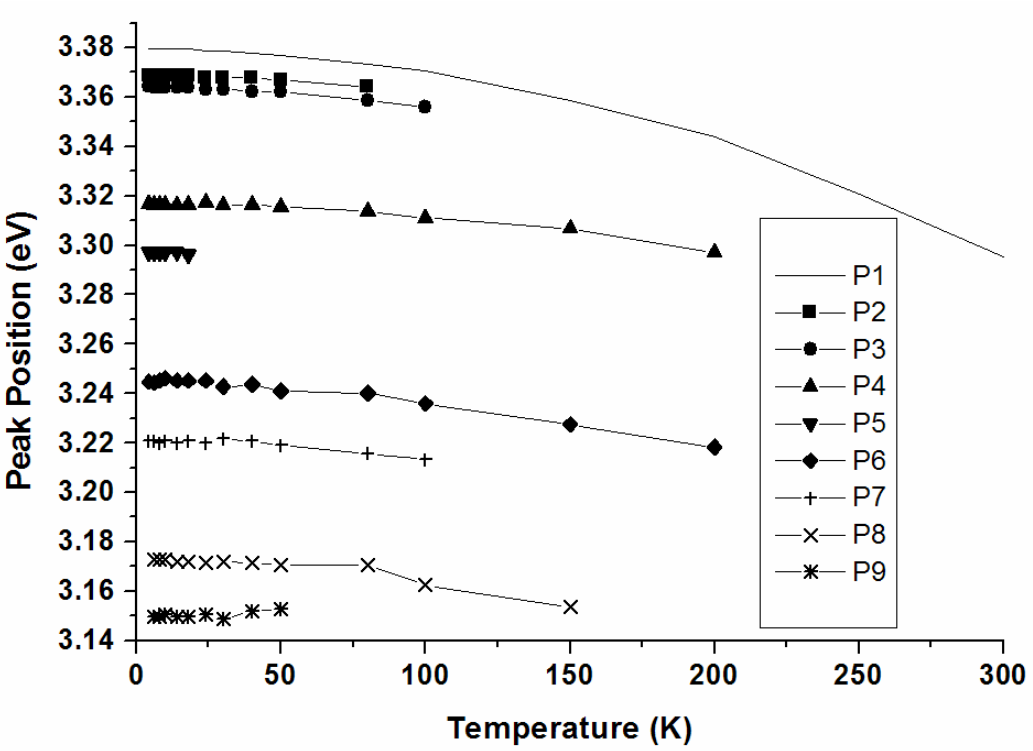

Figure 4.6. Plot of free and bound exciton peak position versus temperature.

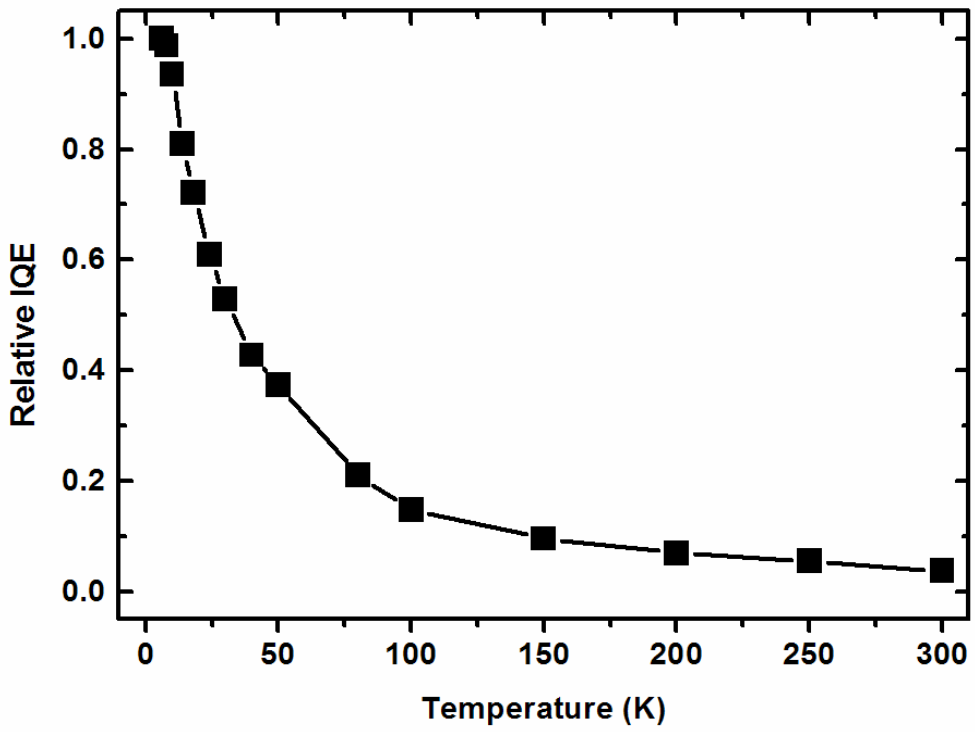

Figure 4.7. Relative internal quantum efficiency versus temperature, assuming internal quantum efficiency is 100% at 6 K.

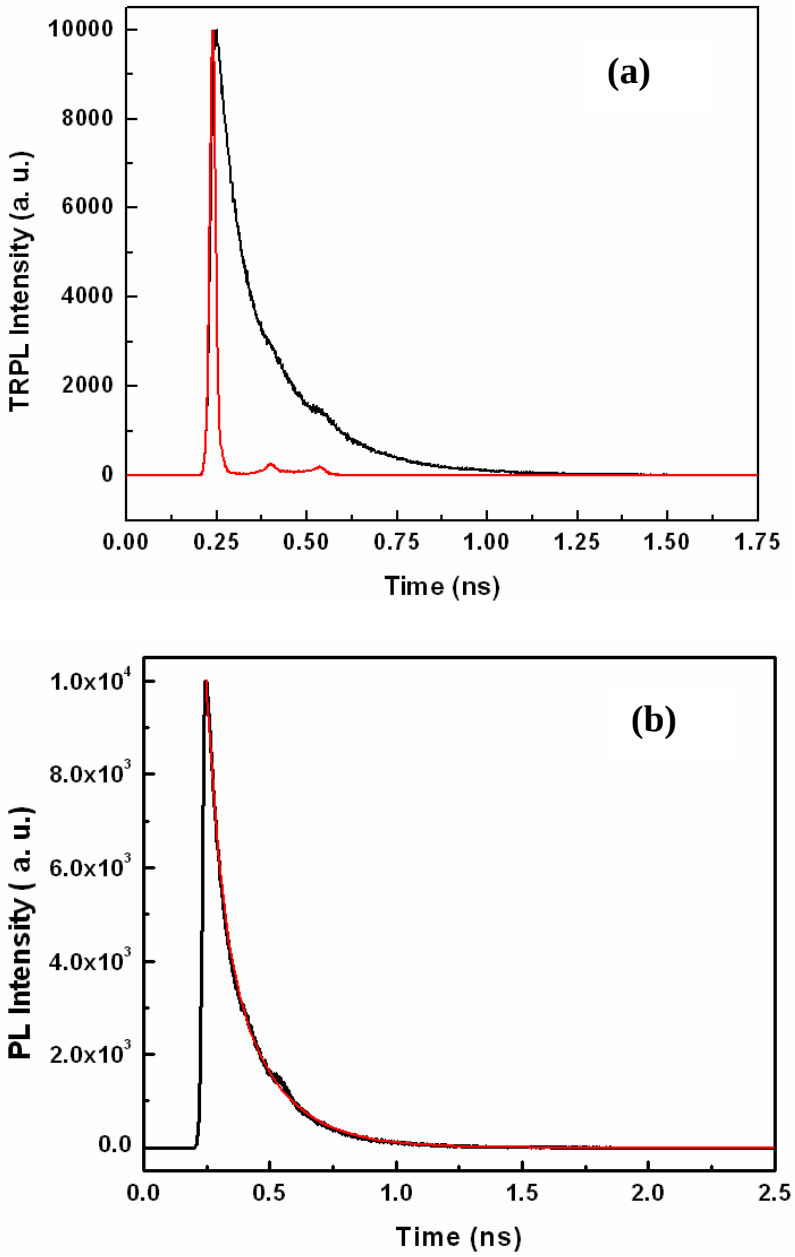

Figure 4.8. (a) Room temperature time resolved photoluminescence spectrum of ZnO nanotips grown on GaN. The red curve in (a) is the instrumental response function (IRF) of the TRPL system. The red curve in (b) shows the curve fitting result based on a biexponential decay function.

4.3 Summary

Temperature dependent PL spectra have been measured on ZnO nanotips grown on a GaN/c-sapphire template. Sharp free exciton and donor-bound exciton peaks are observed at 4.4K with photon energies of 3.380, 3.369, and 3.364 eV, confirming high optical quality of ZnO nanotips. Free exciton emission dominates at temperatures above 50K upto room temperature. The thermal dissociation of these bound excitons forms free excitons and neutral donors. The thermal activation energies of the bound excitons at 3.369 and 3.364 eV are 11 and 16 meV, respectively. Temperature-dependent free A exciton peak emission is fitted to the Varshni's equation to study the variation of energy bandgap versus temperature. Based on the temperature dependent integrated PL intensity, the internal quantum efficiency for the ZnO nanotips is estimated. Time resolved PL spectrum shows a biexponential decay profile with time constants of 192 ps and 47 ps, respectively, suggesting that two different carrier capture mechanisms dominate the carrier recombination process.

Chapter 5. Vertical n-ZnO Nanotips/p-GaN Heterojunction Light Emitting Diodes

5.1 Introduction

ZnO and GaN are similar in many physical properties. They have the same wurtzite-type structure and a small in-plane mismatch (lattice mismatch ~2%). Table 5.1 lists the crystal structure and lattice parameters of ZnO, GaN, and sapphire.

Table 5.1: Crystal structure and lattice parameters of ZnO, GaN, and sapphire.

Crystal	Structure	Space Group	Lattice Parameters (Å)
ZnO	Wurtzite (hexagonal)	$P6_3mc$	$a = 3.249$ $c = 5.206$
GaN	Wurtzite (hexagonal)	$P6_3mc$	$a = 3.186$ $c = 5.178$
Al_2O_3	Corundum (rhombohedral, hexagonal packing of oxygen ions)	$R\bar{3}c$	$a = 4.758$ $c = 12.992$

Initial research focused on using ZnO buffer layers for GaN growth on sapphire [117-121]. Ga-O and Zn-O bonds are stronger as compared to Ga-N bonds [122]. Thus a Ga-terminated GaN surface forms Ga-O-Zn bonds on the introduction of oxygen into the growth chamber, in which monoclinic Ga_2O_3 is presumably formed on the surface, followed by ZnO growth. A schematic of idea atomic arrangement at the ZnO/GaN

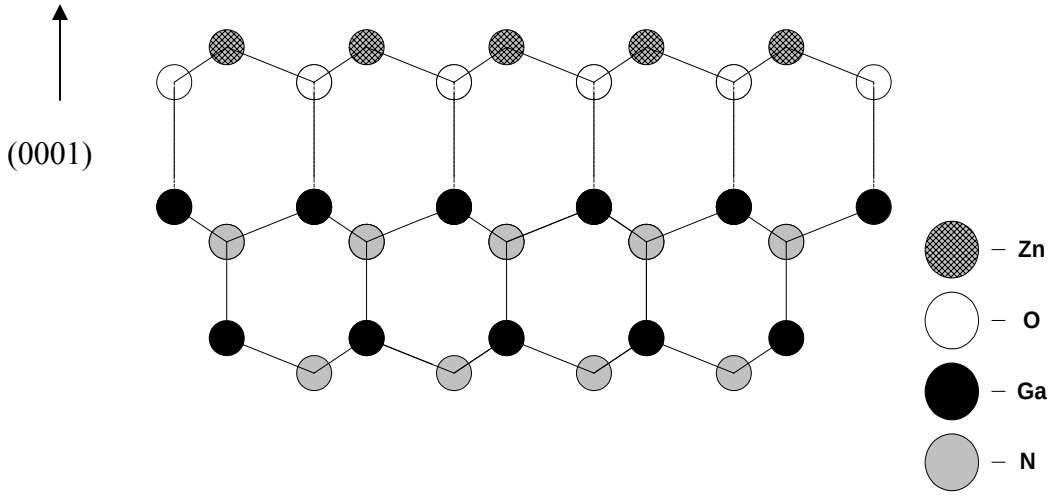

Figure 5.1. Schematic diagram of ideal atomic arrangement at the ZnO/GaN interface.

interface is shown in figure 5.1. ZnO growth on GaN films has been investigated for hybrid optoelectronic devices. ZnO has been used as a transparent conductive oxide electrode for p-GaN [123], and n-ZnO/p-GaN heterojunction LEDs are fabricated [102, 103]. In the ZnO/GaN heterostructure, a Type-II band alignment was reported. In a Type II heterostructure, electrons and holes are spatially separated, which benefit certain devices.

In a hybrid n-ZnO nanotips/p-GaN heterojunction light emitting diode, ZnO nanotips are used as an active layer, which is directly grown on p-GaN substrate. Such LED structure could have several advantages. In a nanotips LED, the active region utilizes nanostructure promising for higher light extraction efficiency. The 1-D growth, unlike the 2-D epitaxial growth, is a natural growth process governed by the growth habit of the semiconductor. This completely different growth mechanism results in essentially dislocation-free in the nanorods that is critical to achieve high internal quantum efficiency. With such a 2-D physically confined nanostructure, 1-D carrier transportation and thus a more efficient current injection can be realized. Controlled localized states due to a reduced dimension are also possibly in these nanorods, leading to carrier localization and improved gain efficiency.

5.2 Processing Development Based on n-ZnO Nanotips/p-Si Heterostructure

The issues in the processing development of vertical ZnO nanotips-based devices include nanoscale fill-in and isolation, planarization, and metallization for electrodes. A prototype n-ZnO nanotips/p-Si heterojunction device that has similar structure of an n-

ZnO nanotips/p-GaN heterojunction device is made and serves for processing development.

To achieve good electrical properties of n-ZnO nanotips/p-Si heterojunction diode, the SiO_2 at ZnO/Si interface is undesirable. To remove the native SiO_2, Si substrate is dipped into 10% HF solution before loading it into the MOCVD chamber. The diluted HF treatment protects the Si surface from further oxidation by terminating the Si with hydrogen atoms at room temperature [124]. Since the growth of ZnO nanotips is carried out in an oxygen ambience, the pre-exposure to oxygen would lead to surface oxidization of Si substrates. To further reduce the interfacial SiO_2 thickness, it is important to minimize the exposure time of Si substrates to oxygen before the growth process. To investigate the effects of HF surface treatment and oxygen exposure on interfacial SiO_2, four ZnO nanotip samples are grown on Si substrate under similar growth conditions. Sample A1 and A2 are grown without reduction of oxygen pre-exposure time. Samples B1 and B2 are grown with minimized oxygen pre-exposure time before the growth. The Si substrates for sample A1 and B1 have native SiO_2, while the Si substrates for A2 and B2 are pre-treated with diluted HF solution. The growth time for all four samples is ~2 minutes. After the growth, the samples are loaded into a XPS vacuum chamber. The ZnO layers then are continuously sputtered away by Ar plasma with a beam tilt angle of 45^o. The intensities of Zn, O, and Si peaks along the ZnO/Si interface are monitored by XPS scan. Figure 6.2 shows the XPS spectra of the sample B2, which undergoes HF pre-treatment of substrate and minimized oxygen pre-exposure. The peak at binding energy of 91 eV and the shoulder at ~93 eV correspond to Zn $3p_{3/2}$ and Zn $3p_{1/2}$, respectively. The peak at binding energy of 101 eV is attributed to Si_{2p} (for single crystal Si). The

intensity of Si_{2p} peak (associated with SiO_2) at binding energy of ~104.5 eV is very weak. The peak SiO_2 atomic percentages of the four samples near the ZnO/Si interface are summarized in table 5.2.

Table 5.2: Peak atomic percentage of SiO_2 at the ZnO/Si interface by XPS depth profile.

Sample #	Si substrate treatment	Pre-growth oxygen exposure	Peak SiO_2 atomic percentage
A1	Without HF treatment	Without oxygen exposure control	7.5%
A2	With HF treatment	Without oxygen exposure control	6.3%
B1	Without HF treatment	Minimized oxygen exposure	5.5%
B2	With HF treatment	Minimized oxygen exposure	3.2%

Sample A1, which does not have Si substrate treatment and minimized oxygen pre-exposure, has a high peak SiO_2 atomic percentage of 7.5%. By HF substrate pre-treatment only (sample A2) and minimized oxygen pre-exposure only (sample B1), the peak SiO_2 atomic percentage is reduced to 6.3% and 5.5%, respectively. Sample B2, with both HF substrate treatment and minimized oxygen pre-exposure, has the lowest SiO_2 atomic percentage of 3.2%. No fluorine residues from HF substrate treatment, which may act as donors in ZnO [125], are detected at the ZnO/Si interface. Hence, Si substrate

treatment by diluted HF and minimized oxygen pre-exposure can significantly reduce the thickness of interfacial SiO_2 for ZnO nanotips grown on Si.

Figure 5.3 shows a schematic of a cross-sectional diagram of a hybrid n-ZnO nanotips/p-Si heterojunction p-n diode. The ZnO nanotips (~ 400nm in height) are grown on p-Si (100) substrates (ρ = 0.001-0.005 Ω·cm) with light Ga doping under optimized growth conditions. ZnO nanotips are grown on HF-treated Si (100) substrate at ~480^{o}C with minimized oxygen exposure prior to initial growth. The hole concentration in p-Si was estimated in an order of 1.0×10^{19} cm^{-3}, and the electron concentration in ZnO film was approximately 10^{18} cm^{-3}.

After the growth of ZnO nanotips on p-Si, the sample was cleaned in acetone, methanol and DI water. An n-ZnO nanotips/p-Si heterojunction diode is then fabricated with a circular pattern. To prevent the top-contact metal particles from reaching the bottom of the ZnO nanotip, which leads to short of the junction, the interstices between ZnO nanotips are filled in using an insulator. The fill-in process can be carried out either by a solid-liquid phase or by a gas phase. Compared with the gas phase process, the solid-liquid fill-in offers low cost and simplicity for demonstrating prototype devices. The two critical factors to be considered in a solid-liquid fill-in process are surface wettability and viscosity of the fill-in solution. Under most growth conditions, the surface of ZnO nanotips behaves as hydrophilic, making it suitable for using the solid-liquid fill-in solution.

A diluted photoresist (PR) AZ5214E is chosen as the solid-liquid fill-in insulator. Fill-in multilayer PR was first spin-on coating on the ZnO nanotips/Si samples, followed by hard baking at 120°C for 10 minutes. Oxygen plasma was used to etch away the PR

and expose the nanotips top for metallization. The PR etching rate is 2 Å/s. The p-n diodes were fabricated using photolithography and lift-off techniques.

The first photolithography step defined the etching mesas, then the sample was dipped into a diluted HCl solution, and a series of circular mesas made of ZnO nanotips were formed by wet etching ZnO nanotip layer down to the conductive p-Si substrate. These mesas have variable diameters of 85, 110, 160, 210, and 260μm, respectively. After the ZnO mesa formation, the second photolithography step defined the ohmic contact patterns on p-Si. The Al bottom electrode was deposited by electron beam (e-beam) evaporation and lift-off, followed by thermal annealing at a N_2 flow. By heating the Al-Si system to a temperature close or slightly higher than the eutectic temperature (~ 580°C), a thin p^+-Si layer is formed at Al/Si interface for Ohmic contact, as shown in figure 5.4 (a).

A top Al electrode was fabricated on ZnO nanotips using the third photolithography step followed by e-beam deposition and lift-off. Aluminum is chosen as the ohmic contact metal for n-type ZnO, as Al has a low barrier height on ZnO, and it is also a shallow donor to ZnO. Al reacts strongly with chalcogenides (O in ZnO). By forming a thin n^+-ZnO layer at Al/ZnO interface, a low specific contact resistance can be achieved [126]. Shown in figure 5.4 (b) is the Ohmic contact at ZnO nanotips. In this step, the top electrodes consist of dots with diameters of 75, 100, 150, 200, and 250μm, respectively. 100 nm Al is deposited by E-beam evaporation to form ohmic contact at ZnO nanotips and p-Si substrate, respectively. The top view of the n-ZnO nanotips/p-Si diode is shown in figure 5.5.

Figure 5.6 shows the I-V characteristic of an n-ZnO nanotips/p-Si heterojunction diode. For a diode with diameter of 200 μm, the forward threshold voltage is below 2.0 volts. The forward current at 3.0 volts is 5.64 mA, and the reverse leakage current at 10 volts is 15 μA. The breakdown voltage of the diode is ~17 volts.

An energy band diagram of the n-ZnO/p-Si heterojunction based on Anderson model in an ideal case without considering spontaneous and piezoelectric polarizations at the interface is shown in figure 5.7. The conduction band (CB) offset $\Delta E_c = \chi_{ZnO} - \chi_{Si} =$ 0.3 eV, where χ_{Si} (4.05eV) [127] and χ_{ZnO} (4.35 eV) [128] is the electron affinity of Si and of ZnO, respectively. The valence band (VB) offset $\Delta E_v = \Delta E_g + \Delta E_c = 2.55$ eV, where ΔE_g is the bandgap difference between ZnO (= 3.37 eV) and Si (= 1.12 eV). Therefore, the diode current is mainly contributed by electron transport over the barrier height at low and moderate forward biases. Since the ideality factor of the I-V characteristics is much large than 2, defect-mediated nonthermionic current transport dominates, such as minority carrier traps and interface states.

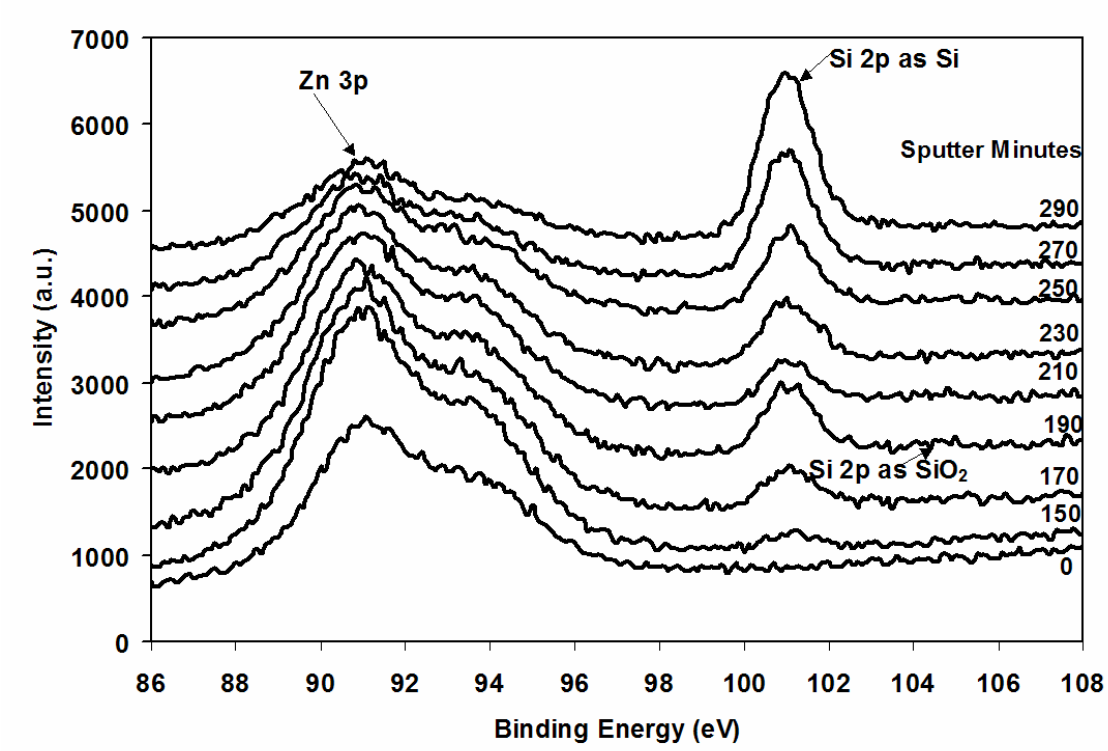

Figure 5.2. X-ray photoelectron spectroscopy (XPS) spectra of ZnO nanotips/Si interface (sample B2). With HF surface treatment and minimized oxygen pre-exposure, sample B2 has minimized interfacial SiO_2 thickness.

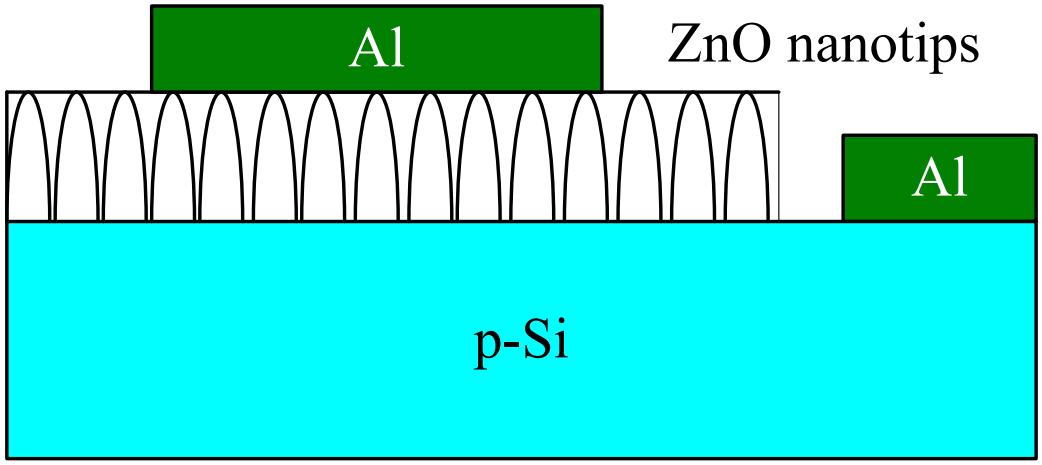

Figure 5.3. Schematic diagram of a hybrid n-ZnO nanotips/p-Si heterojunction p-n diode.

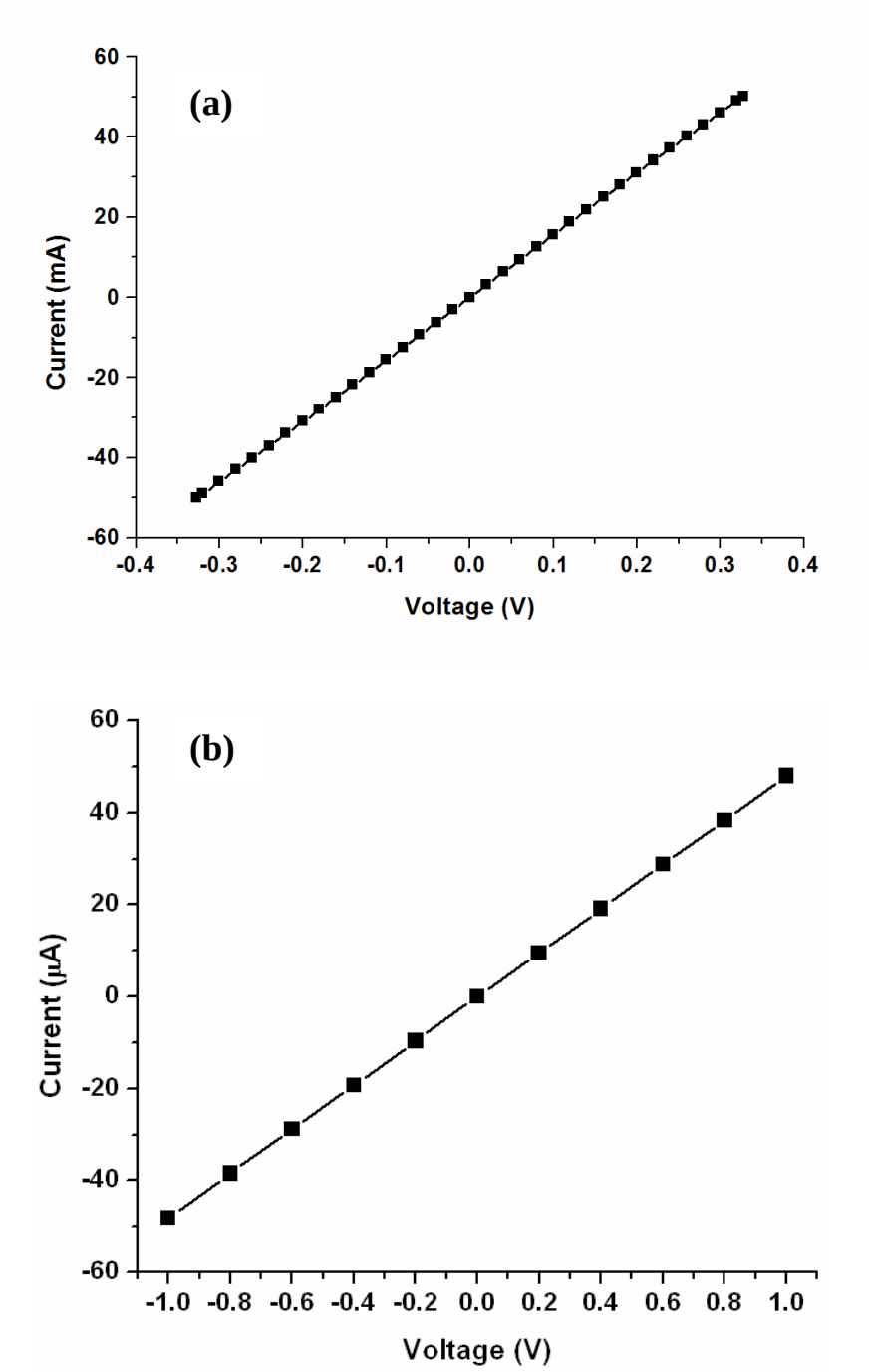

Figure 5.4. I-V characteristics of Al contact to (a) p-Si and (b) undoped ZnO nanotips.

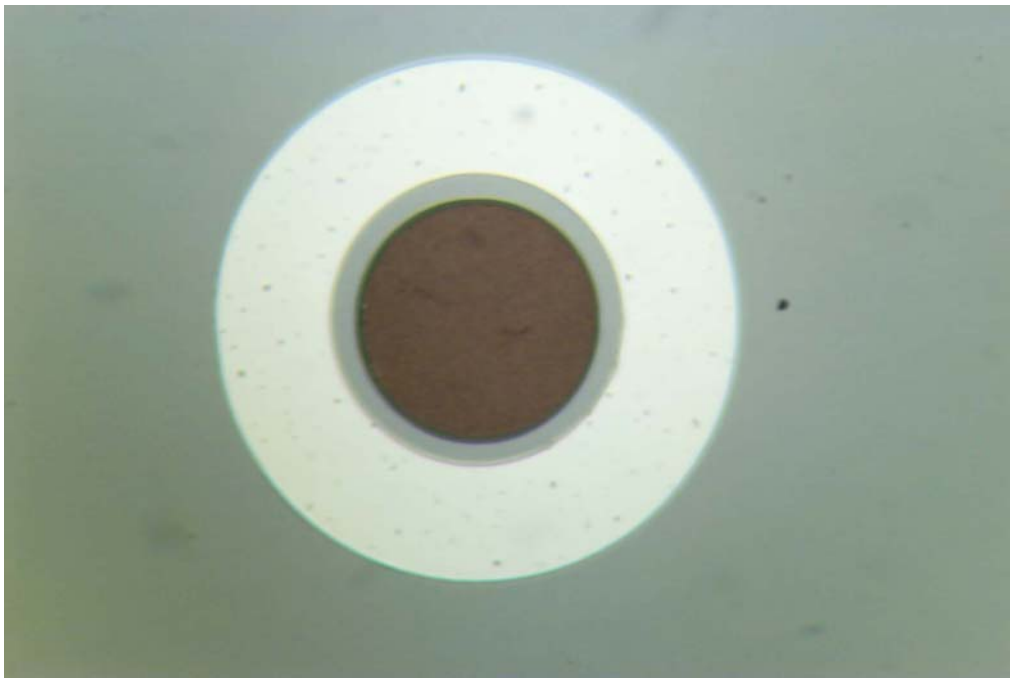

Figure 5.5. Top view of an n-ZnO nanotips/p-Si heterojunction diode under an optical microscope.

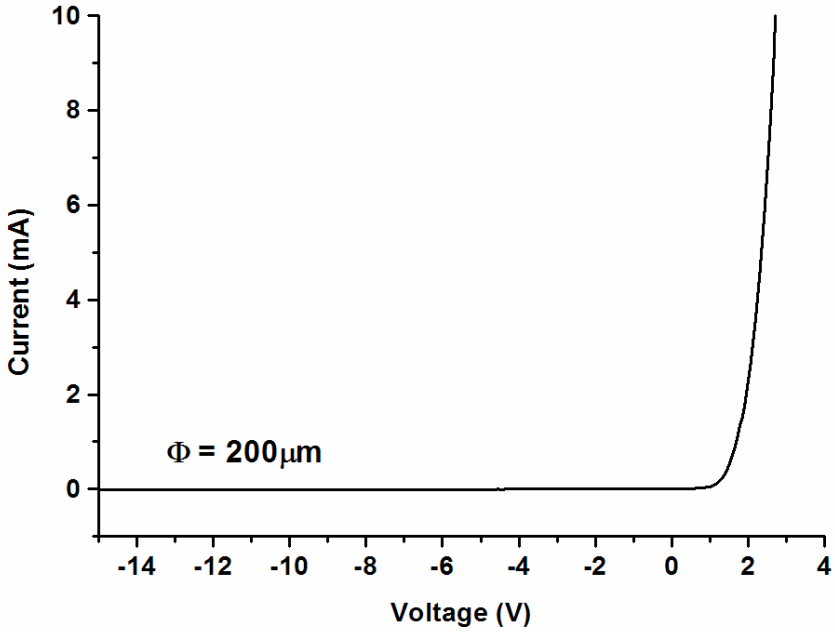

Figure 5.6. I-V characteristic of an n-ZnO nanotips/p-Si heterojunction diode with minimized SiO_2 layer thickness at the ZnO/Si interface.

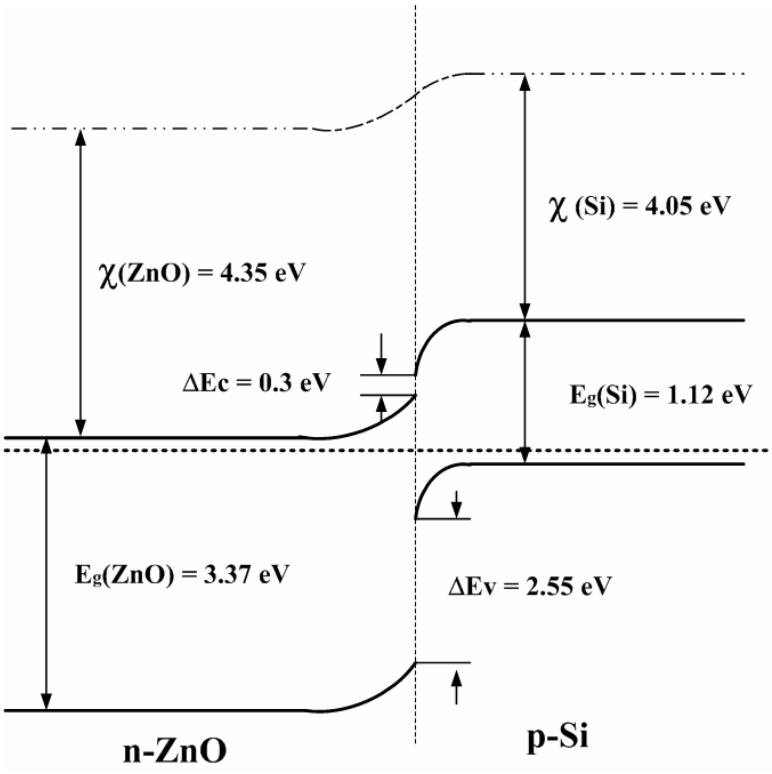

Figure 5.7. Energy band diagram of n-ZnO nanotips/p-Si heterostructure in an ideal case without considering spontaneous and piezoelectric polarizations at the interface.

5.3 Hybrid n-ZnO Nanotips/p-GaN Heterojunction Light Emitting Diode

The basic processing technology developed in the n-ZnO nanotips/p-Si heterojunction is used for fabrication of an n-ZnO nanotips/p-GaN heterojunction LED. Figure 5.8 shows a schematic diagram of the n-ZnO nanotips/p-GaN heterojunction LED. p-type doped GaN templates were grown on c-plane sapphire by MOCVD. The p-GaN substrates consist of 1.9 μm-thick undoped GaN base layers, followed by about 1 μm-thick Mg-doped p-type layers. The electrical properties of p-GaN films were measured at room temperature by Hall effect using the van der Pauw configuration. The free hole concentration and mobility were found to be $p = 3.0\times10^{17}$ cm^{-3} and $\mu_p = 9.7$ $cm^2V^{-1}s^{-1}$, respectively. A layer of lightly Ga doped ZnO nanotips (~ 400nm thick) were grown on the p-GaN film/c-sapphire by MOCVD. The reference Ga concentration for ZnO was in an order of 5×10^{18} cm^{-3}.

Prior to the ZnO nanotip growth, the GaN template was ultrasonically cleaned in acetone, methanol and a diluted 1:1 HCl solution, and then rinsed with deionized water. The oxygen gas exposure time is reduced before ZnO growth in order to minimize the surface oxidation at the ZnO/GaN interface. After the growth of ZnO nanotips on p-GaN, the sample was cleaned in acetone, methanol and DI water. An n-ZnO nanotips/p-GaN heterojunction light emitting diode is fabricated with a circular pattern. Similar as the fill-in and planarization process for fabricating n-ZnO nanotips/p-Si p-n diode, the interstices between ZnO nanotips were filled in using a diluted photoresist. Fill-in multilayer PR was first spin-on coating on the samples, followed by hard baking. Oxygen plasma was used to etch away the PR and expose the nanotips top for metallization.

The p-n diodes were fabricated using photolithography and lift-off techniques. After masking the ZnO nanotips surface with a diameter of 200μm, the sample was dipped into a 1:100 diluted HCl solution to etch way the top ZnO layer down to the p-GaN layer. The etching rate for ZnO nanotips is ~ 10nm/s. A thin layer of Al/Au (5 nm/5 nm) was deposited on ZnO nanotips, serving as a transparent conductive layer for current spreading and an optically transparent window for the light emission from the heterojunction LED. Al (300nm) was then used for top ohmic contact to n-type ZnO nanotips, while Ni/Au (20 nm/180 nm) was used for bottom ohmic contact to p-GaN. Prior to the e-beam deposition of Ni/Au, the p-GaN layer was etched in a 1:7 diluted buffered oxide etching (BOE) solution, and was compared with the p-GaN sample without BOE treatment. Figure 5.9 shows top view of an n-ZnO nanotips/p-GaN heterostructure LED under an optical microscope. I-V characteristics of the heterostructures and point-to-point metal contacts were measured by a HP 4165C semiconductor parameter analyzer. Electroluminescence (EL) spectra were recorded at different injection current by a computer-controlled PMT and a photon counting unit.

Optical properties of ZnO and GaN films were characterized by room temperature PL spectroscopy. Shown in figure 5.10 are the PL spectra of ZnO nanotips and p-GaN layers, respectively. The PL spectrum of ZnO nanotips is dominated by a strong NBE UV emission with a maximum of 3.32 eV and FWHM of ~140 meV. No significant defect-related deep level emission band is observed from these nanotips. Broadband emission from p-GaN film consists of two main peaks at 2.88 eV and 2.79 eV in the blue wavelength. This is usually attributed to radiative transitions from conduction band or shallow donors to Mg acceptor level in the mid bandgap of GaN.

The I-V characteristics of Ni/Au contacts to p-GaN are shown in figure 5.11. For comparison, rapid thermal annealing (RTA) was performed on the samples at 550°C for 1 minute in nitrogen ambient. Near linear I-V behaviors were observed for as-deposited Ni/Au contact (black curve) and for the sample after RTA treatment (red curve), indicating formation of Ohmic-like contacts. By annealing the Ni-Au-GaN system to a higher temperature around 550°C, a thin NiO layer is formed at the metal/p-GaN interface, while Ga vacancies are generated below the contact [129]. The red curve in figure 5.11 has a sharper slope, showing an improved specific contact resistance to p-GaN achieved after RTA treatment. The I-V characteristics of Ni/Au contact to p-GaN without surface treatment using BOE were also measured. In contrast, a nonlinear Schottky-like behavior was obtained. BOE could remove the native oxide and increase the carrier concentration near the surface of p-GaN layer [130].

The specific contact resistance R_{sc} for Ni/Au contact to p-GaN with BOE treatment is estimated by the definition:

$$R_{SC} = \left.\frac{\partial V}{\partial J}\right|_{V \to 0} \qquad (5.1)$$

where R_{SC} is the specific contact resistance (Ωcm^2), V is the voltage (V), and J is the current density (A/cm^2). A specific contact resistance of 1.2×10^{-3} Ωcm^2 is deduced for as-deposited Ni/Au contact to p-GaN in figure 5.11. After RTA treatment, the specific contact resistance is reduced to 6.4×10^{-4} Ωcm^2.

Shown in figure 5.12, are the I-V characteristics of the n-ZnO nanotips/p-GaN heterostructure. We observe junction rectifying properties, indicating a p-n diode is formed between n-ZnO nanotips and p-GaN layers. The built-in voltage under forward bias is ~3V. A reverse breakdown occurs at a voltage of ~ - 8V. The diode has a leakage

current of ~ 54 μA at -5V. The I-V characteristics follows an approximately $I - V^2$ relationship. However, the physical origin of $I - V^2$ is unclear and still in controversy. It might be attributed to space charge limited current due to unipolar carrier injection in wide band gap materials, such as ZnO, GaN, and SiC [102, 131, 132]. We suspect that the current transport in the ZnO/GaN heterojunction could be dominated by defect-mediated nonthermionic processes, such as minority carrier traps and interface states.

Blue light emission was observed in the n-ZnO nanotips/p-GaN heterostructure LED under forward biases, shown in figure 5.13. EL spectra of the heterojunction LED under different forward current injection were measured, and the results are shown in figure 5.14. When the forward current increases from 0.6 mA to 4.2 mA, broad EL emission is observed with a significant tail on the long wavelength side. The shape of the EL spectrum does not show significant change at various injection current levels measured. It has a peak wavelength of 406 nm. At 4.2mA, the EL FWHM is 62 nm. The EL spectrum of the n-ZnO nanotips/p-GaN heterojunction LED is compared with PL spectra of ZnO nanotips and GaN, suggesting luminescence primarily from radiative recombination due to electron injection from ZnO nanotips into the p-GaN side. The light output power shows a near linear dependence on the injection current from the spontaneous emission.

The band alignment of n-ZnO nanotips/p-GaN heterojunction can be determined using the Anderson model in an ideal case without considering piezoelectric and spontaneous polarizations at the interface (figure 5.15). The electron affinity values for GaN and ZnO have been taken as 4.2 and 4.35 eV [128]. The conduction band offset ΔE_c is calculated by the difference between electron affinities of ZnO and GaN:

$$\Delta E_c = \chi_{ZnO} - \chi_{GaN} = 0.15 \text{ eV} \quad (5.2)$$

The valence band offset ΔE_v is calculated by:

$$\Delta E_v = \Delta E_c + \Delta E_g = 0.13 \text{ eV} \quad (5.3)$$

where ΔE_g is the energy band gap difference between ZnO (3.37 eV) and GaN (3.39 eV): -0.02 eV. Therefore, the energy barrier for holes is slightly lower than that for electrons. However, since the electron concentration in ZnO nanotips is one order higher than the hole concentration in p-GaN, electron injection from n-ZnO nanotips to p-GaN is more likely than hole injection from p-GaN to n-ZnO nanotips. This also suggests that EL primarily from radiative recombination due to electron injection from ZnO nanotips into the p-GaN side.

5.4 Summary

A prototype an n-ZnO nanotips/p-GaN heterojunction p-n diode and blue LED is demonstrated. Lightly Ga doped ZnO nanotips are directly grown on top of a p-GaN layer using MOCVD, and a p-n junction is formed between ZnO nanotips and p-GaN. The p-n diode has a turn-on voltage of 3V, and a breakdown voltage of ~ 8V. The forward current at 5V is 2.5 mA, and the reverse leakage current at –5V is 54 μA. A blue light emission with a peak wavelength at 406 nm is observed under the forward current injection. EL spectra have been compared with PL. The electroluminescence is primarily due to radiative recombination from electron injection into p-type GaN.

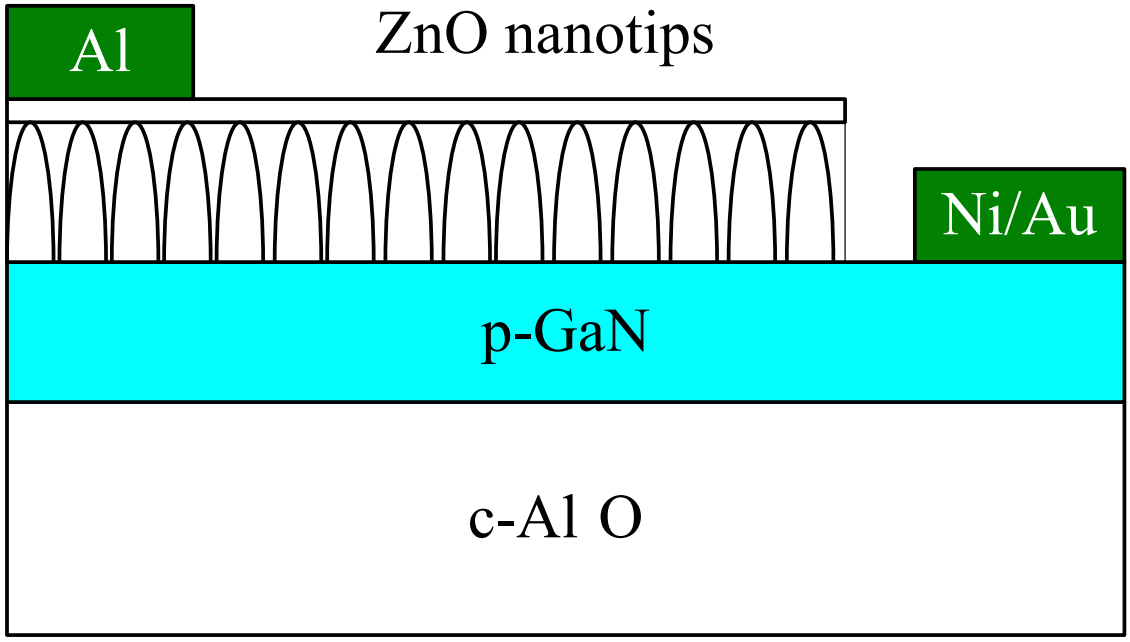

Figure 5.8. Schematic diagram of an n-ZnO nanotips/p-GaN heterojunction LED.

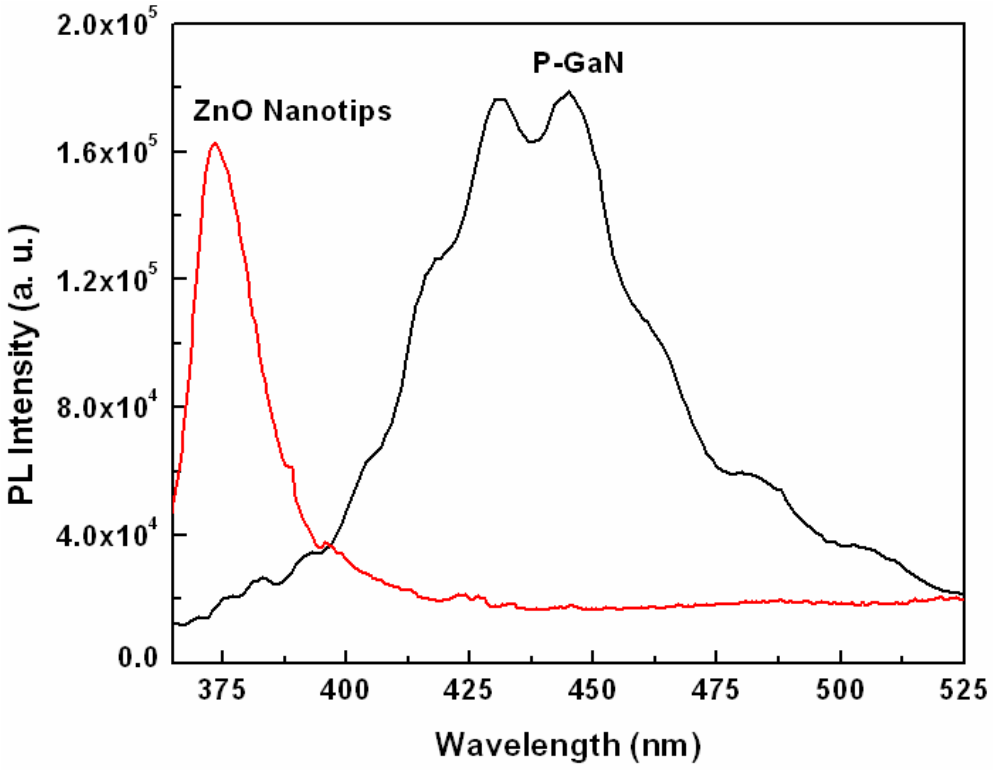

Figure 5.9. Room temperature PL spectra of p-GaN (black curve) and ZnO nanotips (red curve).

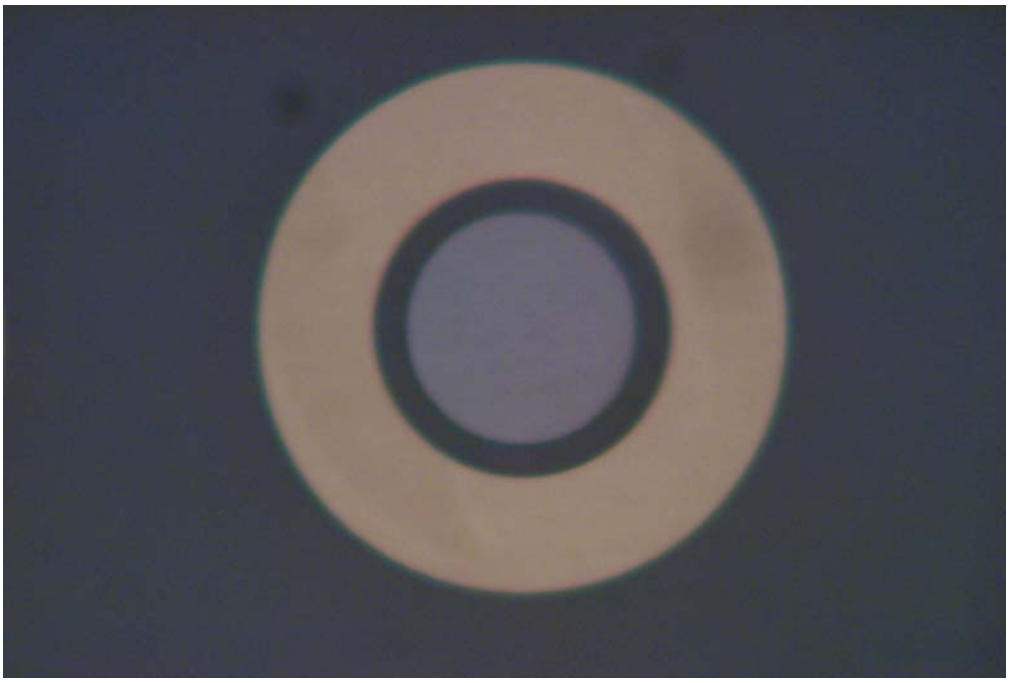

Figure 5.10. Top view of an n-ZnO nanotips/p-GaN heterojunction diode under an optical microscope.

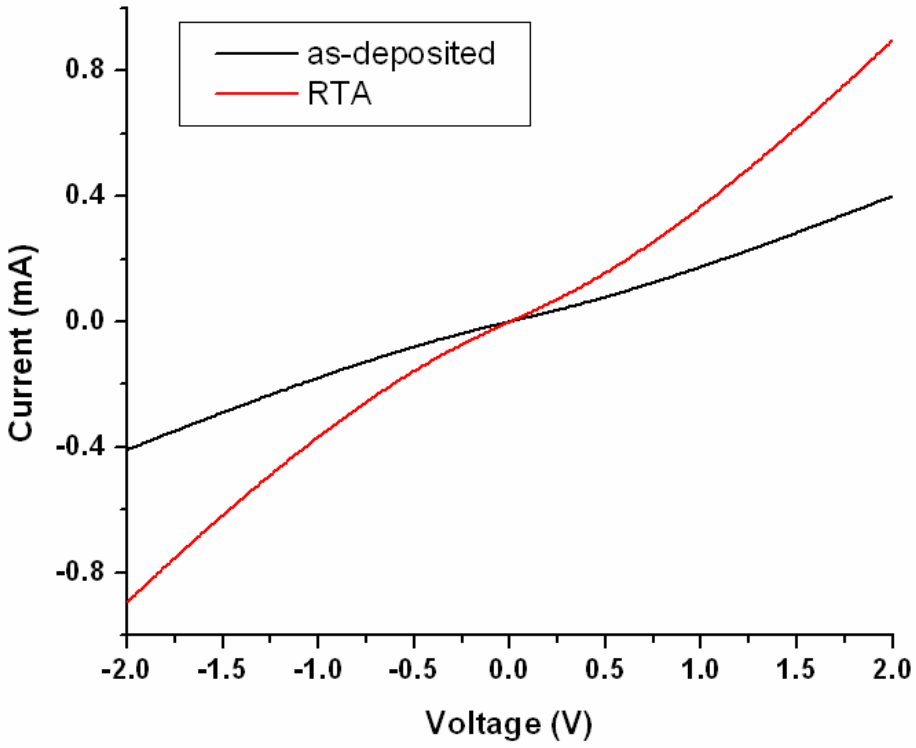

Figure 5.11. I-V characteristics of Ni/Au contact to p-GaN.

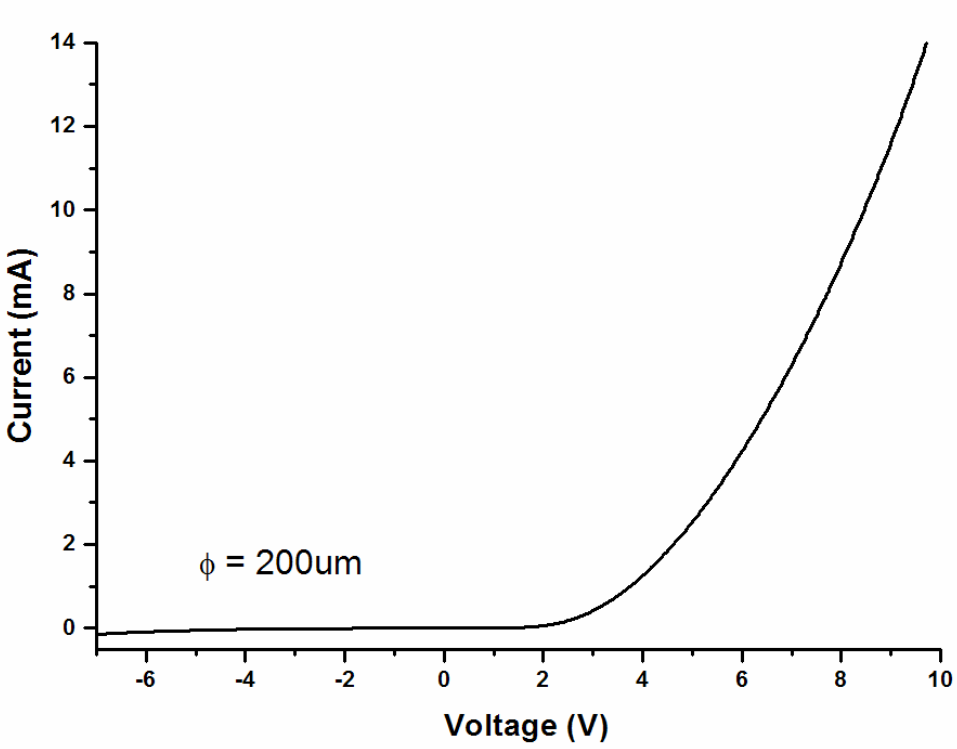

Figure 5.12. I-V characteristic of an n-ZnO nanotips/p-GaN heterostructure.

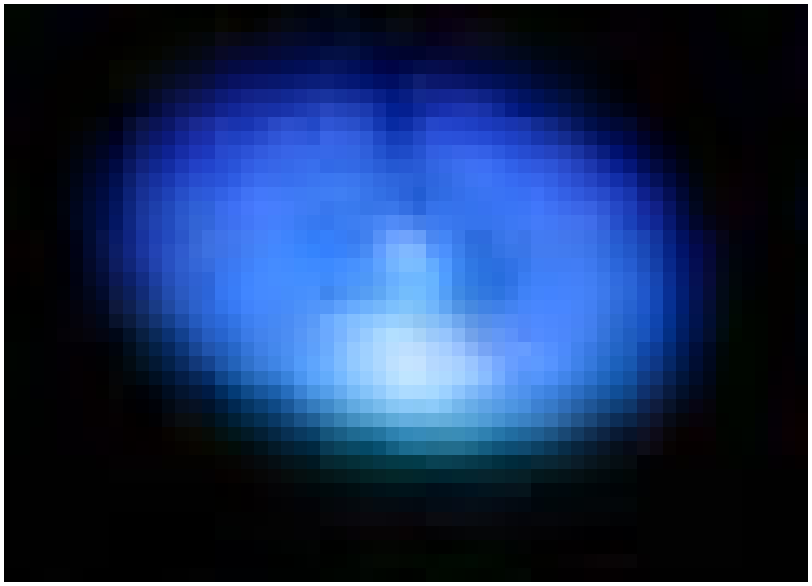

Figure 5.13. Blue light emission from an n-ZnO nanotips/p-GaN heterojunction LED under a forward current injection.

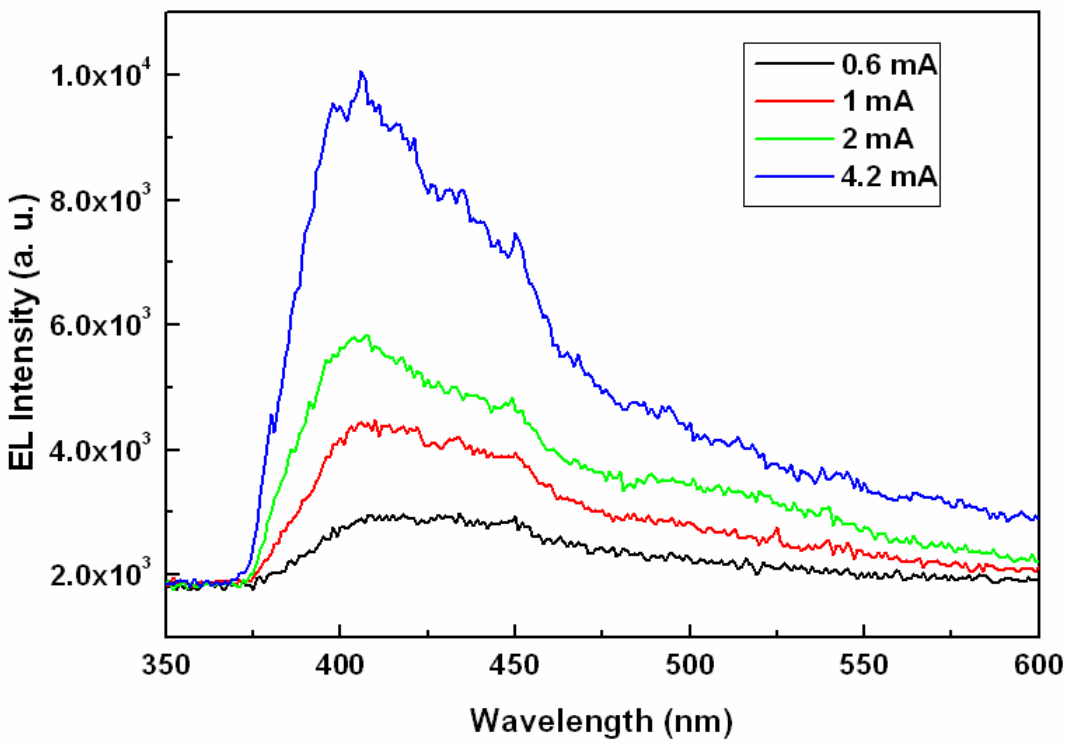

Figure 5.14. Electroluminescence spectra of an n-ZnO nanotips/p-GaN heterostructure light emitting diode under different forward injection current.

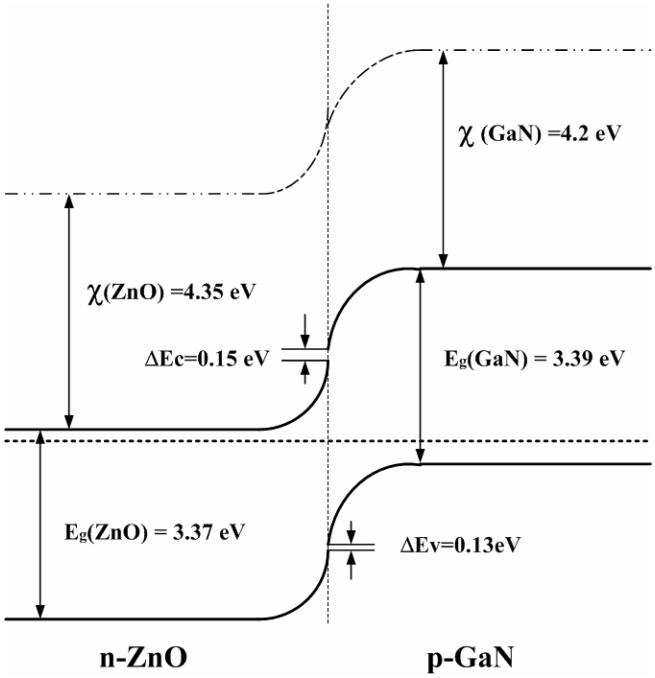

Figure 5.15. Energy band diagram of n-ZnO nanotips/p-GaN heterostructure in an idea case without considering piezoelectric and spontaneous polarizations at the interface.

Chapter 6. Integration of ZnO Nanotips and GaN Light Emitting Diodes for Enhanced Emission Efficiency

6.1 Introduction

One of the major technical issues for nitride light emitting diodes (LEDs) is low external quantum efficiency, even with much higher internal quantum efficiency. GaN has a high refractive index n ~ 2.5. Emission incident at the GaN-air interface at an angle greater than 23.6° is trapped by the total internal reflection. The light out coupling efficiency from a flat semiconductor surface is approximately given by

$$\frac{P_{escape}}{P_{source}} = \frac{1}{4}\left(\frac{1}{n}\right)^2\left[1-\left(\frac{n-1}{n+1}\right)^2\right] \qquad (6.1)$$

where P_{escape} is the optical power emitted into free space, P_{source} is the optical power generated in the LED cavity, and n is the refractive index of the semiconductor. From Eq. (6.1), only ~3.3% of internal generated light can be extracted from a GaN LED. Due to the narrow escape cone, the parasitic nonradiative losses during photon recycling degrade the external quantum efficiency. Extensive research efforts have been made to improve the light extraction from GaN LEDs, such as surface roughening and forming photonic crystals on the top layer [133, 134]. The light extraction dynamics has been discussed in regard to modifying the spontaneous emission by the microcavity effect [135]. Other techniques include light output coupling through surface plasmons, corrugated Bragg gratings, or using random surface texturing [136-140], to convert wave-guided modes into free-space modes. Typical GaN LEDs have p-side-up structures, in which a thick p-GaN is undesirable due to the high resistivity. Manipulation such as dry etching is often difficult in a thin layer without degrading the electrical properties. Flip-chip bonding and

laser lift-off technologies have been used in the LED fabrication [133]. These approaches significantly complicate the GaN LED fabrication.

6.2 Integrated ZnO nanotips/GZO/GaN LED

An integrated ZnO nanotips/GaN LED is fabricated by directly growing ZnO nanotips on top of a GaN LED using MOCVD, to achieve enhanced light emission efficiency. In this structure, a Ga doped ZnO (GZO) layer is first deposited on top of a conventional GaN LED, which is used as a transparent conductive layer to p-GaN. ZnO nanotips are then grown on GZO coated GaN as a light extraction layer for the LED. Unlike other technologies used to enhance light extraction, such as using rough surfaces and photonic crystals, this approach does not require e-beam lithography or etching, making it suitable for low cost and large scale fabrication. The results promise the integration of ZnO nanotips with GaN based optoelectronic devices using epitaxial growth technology.

Figure 6.1 shows a schematic of a cross-sectional diagram of an integrated ZnO nanotips/GZO/GaN LED. InGaN/GaN multiple quantum well (MQW) LED templates were grown on c-plane sapphire by MOCVD. The GaN LEDs consist of undoped and Si-doped n-type GaN base layers, InGaN/GaN MQW active region, followed by Mg-doped p-type layers. A vertical flow rotating disk MOCVD reactor is used for growth of the GZO film and ZnO nanotips. The chamber pressure is kept at 50 torr. The growth temperature for ZnO ranges from 400 to 500°C with a growth rate of 1-2 μm/hr. Diethylzinc (DEZn) and oxygen were used as the Zn metalorganic source and oxidizer, respectively. Triethylgallium (TEGa) was used as the n-type doping source for growth of

GZO films. Exposure of samples to the oxygen gas before the growth was minimized in order to reduce the oxidation at the ZnO/GaN interface.

By suppressing the fast growth rate along ZnO c-axis direction, GZO film with thickness 150nm is first grown on GaN. Four-point probe measurements show that the GZO film has a resistivity of ~5×10^{-3} Ωcm. The subsequent growth of ZnO nanotips is governed by a self-assembling process. ZnO columnar structures are formed due to the highest growth rate along the c-axis from the difference in surface relaxation energies between (0001) and (000-1) planes. The columnar growth has an epitaxial relationship between ZnO and GaN: (0002) ZnO || (0002) GaN and (10-10) ZnO || (10-10) GaN. FESEM pictures of ZnO nanotips grown on a GZO coated GaN LED are shown in figure 6.2 and figure 6.3. Figure 6.2 is a perspective view, showing that ZnO nanotips are grown and distributed over the entire GZO/GaN template surface. They were found to be vertically aligned with the c-axis, normal to the basal plane of the GZO/GaN/c-sapphire template. The nanotips have an average diameter of 60 nm at the bottom and ~10 nm at the top, and a height of ~400 nm. Figure 6.3 is a top view of ZnO nanotips grown on GZO/GaN.

XRD θ-2θ measurements were used to determine the structural relationship between the ZnO nanotips, the GZO and the GaN. Figure 6.4 shows a θ-2θ scan of ZnO nanotips grown on GZO/GaN/c-Al_2O_3. Only ZnO (0002) and GaN (0002) peaks are observed, indicating that these nanotips are preferentially oriented along the c-axis (denoted by the *z* direction), normal to the basal plane of the GZO/GaN/c-sapphire template (denoted by the *x*-*y* plane). It was difficult to separate the possible peaks of (0002) oriented GZO film from (0002) ZnO nanotips. This was expected, as the crystal

structure of GZO film is similar to ZnO nanotips due to the similar atomic radii of Ga and Zn. Since no other ZnO peaks are observed, the GZO film must be oriented in the (0002) orientation, maintaining an epitaxial relationship with the GaN template.

Optical properties of ZnO nanotips/GZO/GaN were investigated by PL. Figure 6.5 is the room temperature PL spectrum of ZnO nanotips grown on GZO/GaN. A strong near band edge PL peak is seen at 3.29 eV with a full width half maximum of 135 meV, while deep level emission is negligible. We have noted that PL is quenched in the heavily doped Ga doped GZO film due to impurity-assisted nonradiative recombination centers created by excess Ga atoms. The dominant free excitonic emission indicates high optical quality of ZnO nanotips.

To fabricate an integrated ZnO nanotips/GZO/GaN LED, the ZnO nanotips/GZO layer was selectively etched using a diluted nitric acid and a subsequent dry etching on the wet-etched area was performed to expose the n-type GaN layer for its n-electrode contact. Ti/Ni/Al and Ti/Au contacts were deposited on the exposed n-type GaN and ZnO for n- and p- electrodes, respectively. A conventional p-metal layer of Ni/Au was also deposited on a GaN LED wafer, serving as a reference. For comparison, a GZO (~150nm)/GaN LED without top nanotips layer was fabricated. Light output power of LED chips was measured by CAS 140B LED tester at various current injection. Figure 6.6 shows light output power of an integrated ZnO nanotips/GZO/GaN LED as a function of forward injection current. Emission from a Ni/Au p-contacting GaN LED is also plotted in figure 6.6. The EL intensity from a ZnO nanotips/GZO/GaN LED has increased by a factor of 1.7 at a forward current of 20 mA, in comparison to the Ni/Au contact GaN LED with the same size. The light output power of a ZnO

nanotips/GZO/GaN LED is also compared with the reference GZO/GaN LED without ZnO nanotips, showing significantly increased light extraction efficiency due to ZnO nanotips. Shown in the inset of figure 6.6 are the EL spectra of a ZnO nanotips/GZO/GaN LED and of a conventional Ni/Au GaN LED at a current of 20 mA. The two EL spectra have essentially identical normalized spectra shape and line width.

The external quantum efficiency of a p-n junction LED is defined as the ratio of the rate of photons emitted into free space to the rate of electrons injection:

$$\eta_{ext} = \eta_{\text{int}} \eta_{extraction} = P(h\nu)^{-1} eI^{-1} \qquad (6.2)$$

where η_{int} is the internal quantum efficiency, $\eta_{extraction}$ is the light extraction efficiency, P is the optical power emitted into free space, and I is the injection current. An optical power of 6mW is measured at a current of 20mA for a conventional Ni/Au p-contact GaN LED, corresponding to an external quantum efficiency of 7%. The external quantum efficiency is increased to 11.4% in a ZnO nanotips/GZO/GaN LED.

6.3 Light Extraction Analysis

The enhancement in light extraction efficiency can be explained by the interaction between the spontaneous emission from the GaN LED and ZnO nanostructures. To analyze the light extraction properties of ZnO nanotips, we performed a two-dimensional Fourier transform on the top view shown in figure 6.7. No distinguishing non-zero spatial frequency has been observed, indicating that the nanotips are randomly oriented in the basal plane of the GZO/GaN template, *i.e.*, the *x*-*y* plane. The absence of spatial periodicity suggests that no photonic crystal is formed that contributes to the light extraction enhancement.

At the dominant EL wavelength of 452 nm the refractive index of ZnO is ~2.0, while that of GaN is ~2.5. The area density of as-grown nanotips is estimated to be on the order of 10^{10} cm^{-2}. As the first approximation, we consider the nanotips layer as a disordered subwavelength assembly of ZnO and air. Effective medium theory [141] then gives the effective refractive index of the nanotip layer as

$$n_{eff} = \left[n_1^2 f + n_2^2 (1 - f) \right]^{1/2} \tag{6.3}$$

where f is the filling factor, and n_1 and n_2 are the refractive indices of ZnO and air, respectively. Note that f here is a function of z. The effective refractive index of the nanotip layer along the z direction is gradually reduced from 1.57 at the bottom, (corresponding to a filling factor of ~0.49) to 1.0 at the top (figure 6.8(a)). The numerical results show that an increase of ~20% in light extraction can be attributed to enhanced optical transmission, in comparison with a GaN layer without ZnO nanotips.

The ZnO nanotips also introduce surface roughness in the LED. As can be seen in figure 6.2, height variation exists among the nanotips. The nanotips surface has a correlation length around 100 nm. It has been shown that light scattering occurs from a random rough surface in the case of correlation length smaller than the wavelength, leading to an increase of transmitted evanescent waves beyond the critical angle [142]. In addition, our FESEM photographs indicate that there is a ~5 nm deviation in an average diameter of 60 nm for the ZnO nanotip bases. This diameter fluctuation gives rise to ±7% variation in the effective refractive index in the x-y plane of the nanotip region (figure 6.8(b)). The combination of surface roughening and non-uniform distribution of dielectric presumably disperses the angular distribution of spontaneous emission in the optical phase space, leading to a larger escape cone in the nanotips layer over the planar structure

(figure 6.8(c)). Numerical simulation indicates that most of the spontaneous emission from the GaN layer within a cone of θ_1= 23.6 ^{o} will escape to the air. The emission outside a cone of θ_2= 38.9 ^{o} will not escape the ZnO layer at all. For emission within 23.6 ^{o} to 38.9 ^{o}, it gradually bends within the ZnO nanotip region until it propagates parallel to the surface.

A Monte Carlo simulation has been developed to calculate the variation in the effective refractive index of the nanotip layer [143, 144]. We have assumed Gaussian distribution for the diameters of ZnO nanotips with an average diameter of 60nm at the bottom. Average effective refractive index is thus numerically calculated. It is found that the diameter fluctuation gives rise to ±7% variation in the effective refractive index in the *x*-*y* plane of the nanotip region (figure 6.8(b)).

We have deduced the fraction of light scattering out in the ZnO nanotip layer based on a simplified light scattering model. The first assumption is for each scattering event in the nanotip layer, 50% of the photons go down to the lower hemisphere, which is almost lost. The other 50% go up to the upper hemisphere. Among this up part, the emission within the critical angle will escape to the air. The second assumption is that the rest part of light remains in the nanotip layer and is repeated scattered by the variation in the effective refractive index in the *x*-*y* plane.

The fraction of light within the critical angle without the scattering is given as

$$\frac{P_{escape(0)}}{P_{source}} = \frac{1}{2}(1-\cos\theta_C) = \frac{A}{2} \qquad (6.4)$$

where P_{escape} is the optical power emitted into free space, P_{source} is the optical power in the GaN LED cavity, θ_c is the critical angle.

After the first scattering event, the fraction of remained light within the critical angle becomes

$$\frac{P_{escape(1)}}{P_{source}} = \frac{A}{2}\frac{(1-A)}{2} \tag{6.5}$$

By adding up all the scattering events, the total fraction of light scattering out the nanotip layer is calculated by

$$\eta_{out} = \frac{\sum_{n=0}^{\infty} P_{escape(n)}}{P_{source}} = \frac{A}{2} + \frac{A}{2}\frac{(1-A)}{2} + \frac{A}{2}\left(\frac{1-A}{2}\right)^2 + \ldots + \frac{A}{2}\left(\frac{1-A}{2}\right)^n + \ldots$$

$$= \frac{A}{1+A} \tag{6.6}$$

Finally, we estimate that ~30% will escape upward averagely. Shown in figure 6.9, is the simulated angular dependent of transmitted light with ZnO nanotips grown on top of a GaN layer. An effective refractive of 1.57 is used in the calculation. For comparison, the optical transmission for standard GaN sample without top ZnO nanotips is also plot.

Combining all effects, an enhancement factor of 1.8 in light output power is deduced, compared to the standard uncoated GaN structure. In our case, a significantly increased light output from a ZnO nanotips/GZO/GaN LED, in comparison with a GZO/GaN LED reference, suggests that out coupling enhancement results from the nanostructure morphology. Comparing the numerical analysis with the LED measurement results, we conclude that enhanced light extraction efficiency in a ZnO nanotips/TCO/GaN LED results from increased light transmission and light scattering in the ZnO/GaN multilayer.

6.4 Summary

Enhancement of light extraction from an integrated ZnO nanotips/GaN light emitting diode (LED) is demonstrated. The device is composed of a GaN LED with a Ga doped ZnO (GZO) transparent conductive layer, and ZnO nanotips grown on GZO for light extraction. The light output power of a ZnO nanotips/GZO/GaN LED exhibits 1.7 times enhancement, in comparison with a conventional Ni/Au p-metal LED. The higher emission efficiency is attributed to the enhanced light transmission and scattering in the ZnO/GaN multilayer. With an optimized GZO layer on p-GaN, significantly higher light emission efficiency is expected to be achieved from the integrated ZnO nanotips/GZO/GaN LED structure. The integration of ZnO nanotips with GaN shows a promising potential for UV/blue optoelectronics.

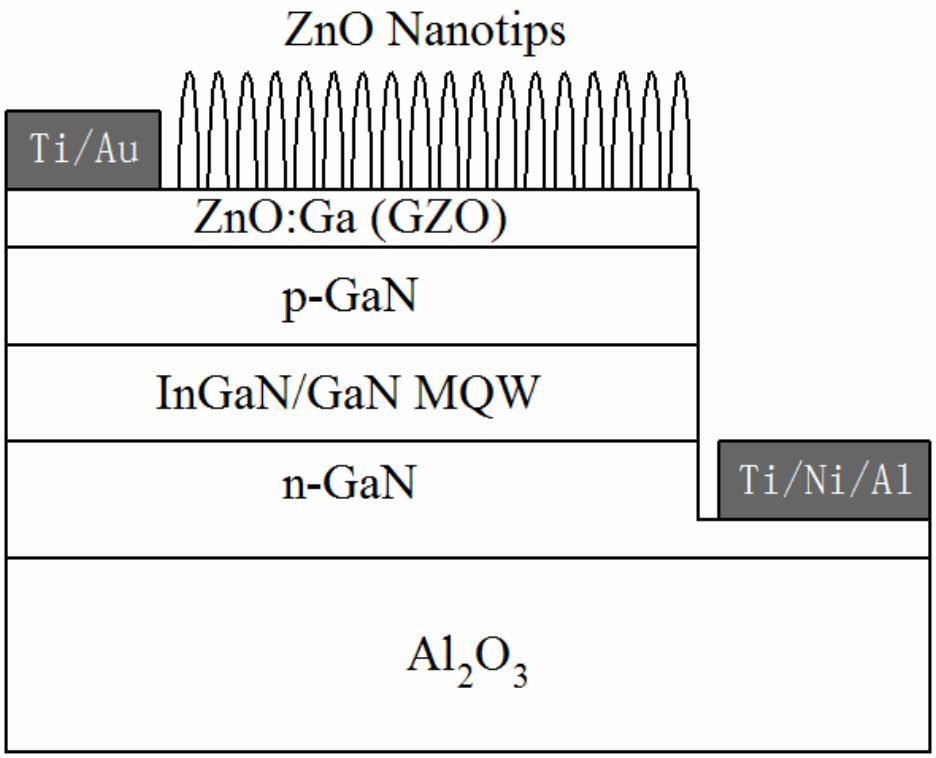

Figure 6.1. Schematic cross-sectional diagram of an integrated ZnO nanotips/GZO/GaN LED.

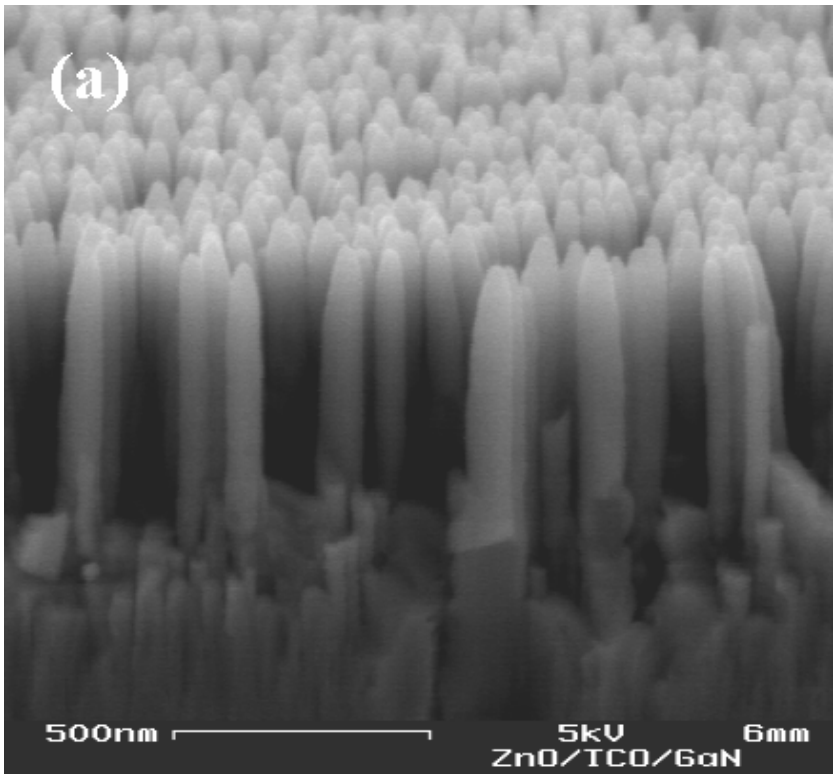

Figure 6.2. FESEM image of ZnO nanotips/GZO/GaN (perspective view).

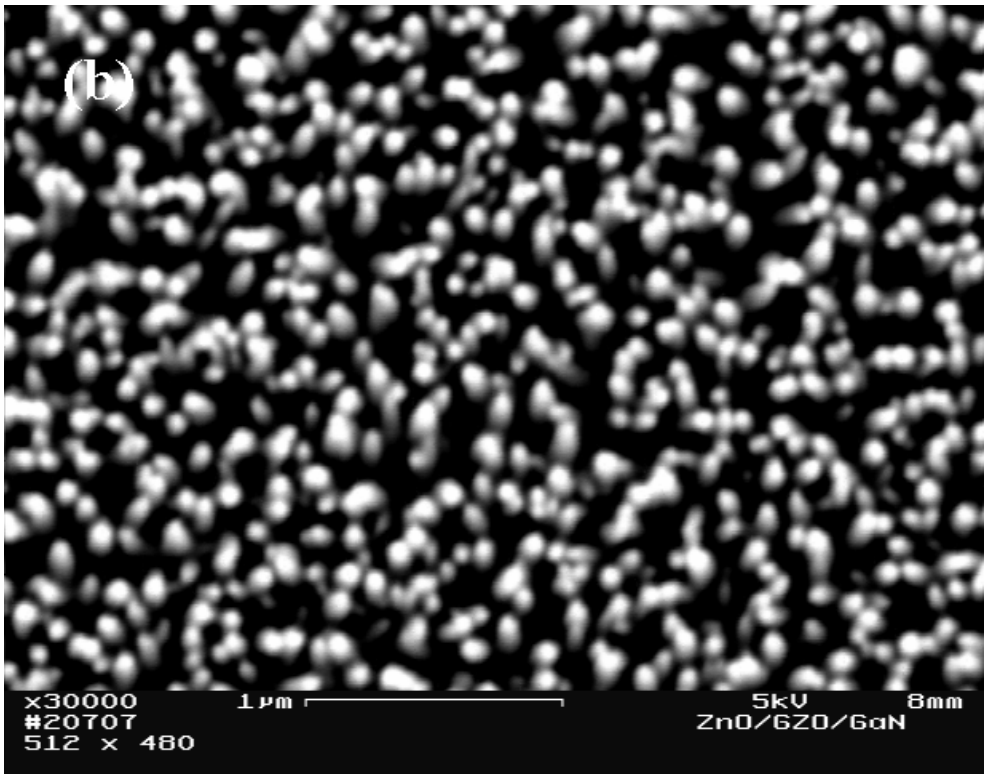

Figure 6.3. FESEM image of ZnO nanotips/GZO/GaN (top view).

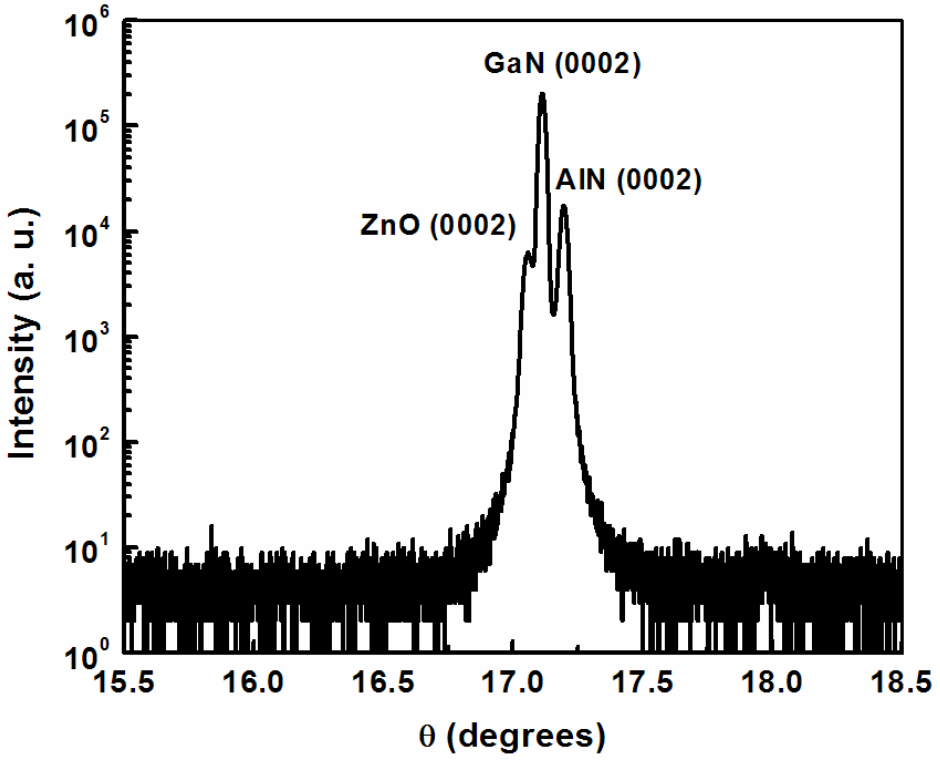

Figure 6.4. XRD θ-2θ scan of ZnO nanotips grown on GZO/GaN/c-Al_2O_3.

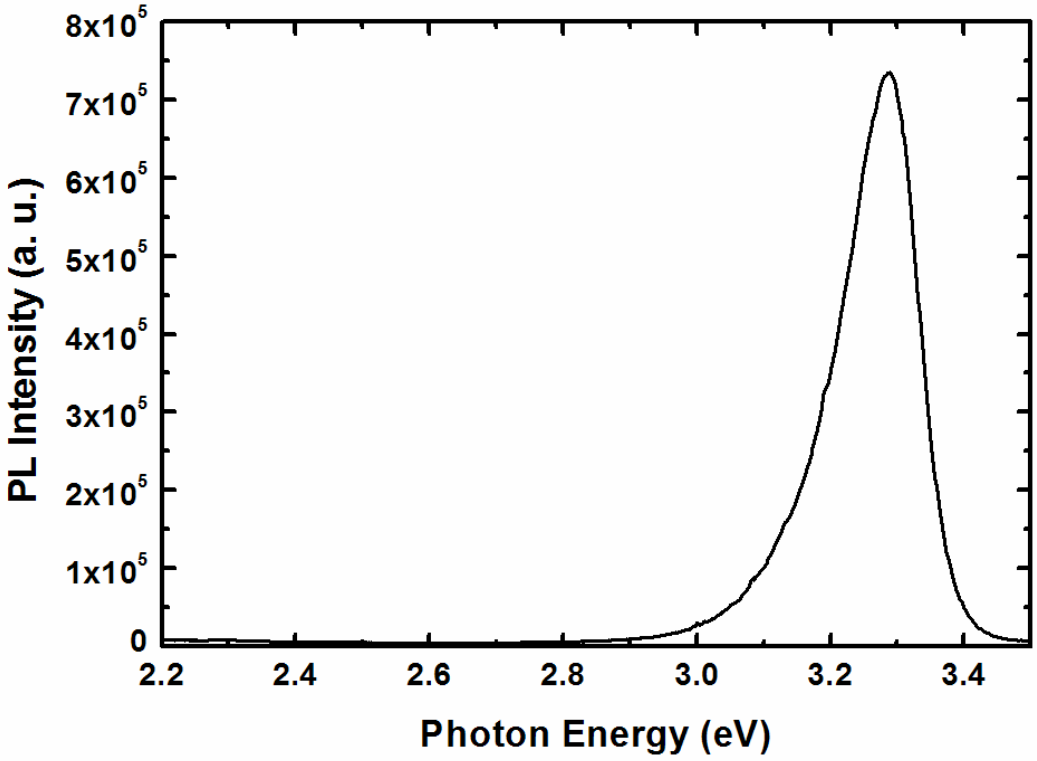

Figure 6.5. Room temperature PL spectrum of ZnO nanotips/GZO/GaN.

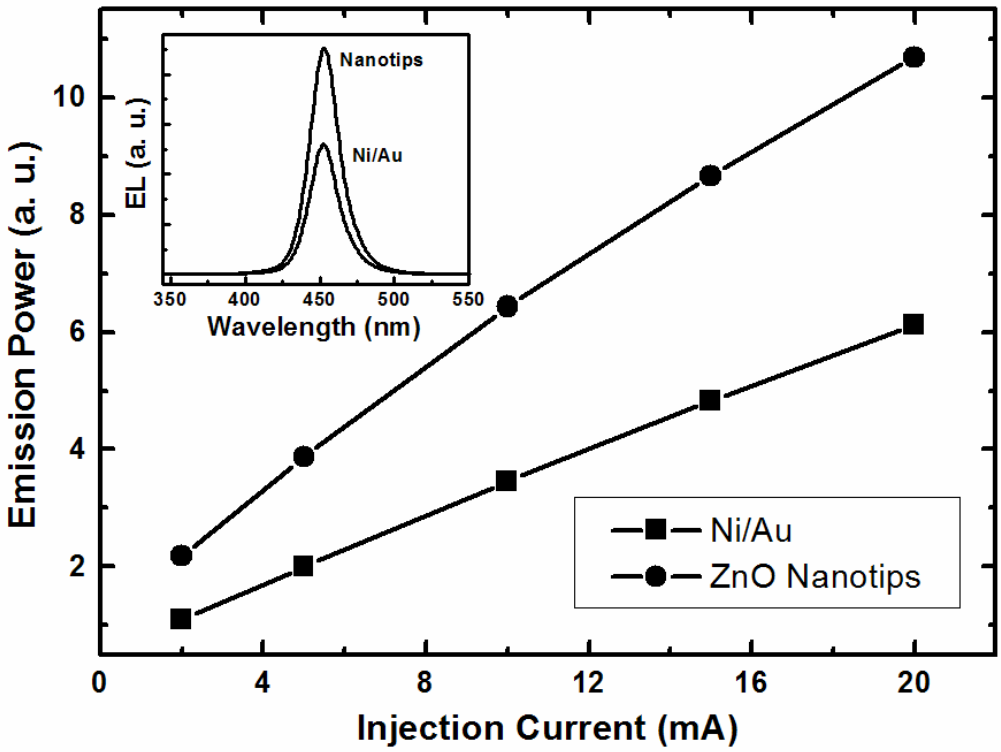

Figure 6.6. Light output power versus forward injection current for Ni/Au and ZnO nanotips/GZO/GaN LED; inset is EL spectra of Ni/Au p-contact GaN LED and ZnO nanotips/GZO/GaN LED at a forward current of 20mA.

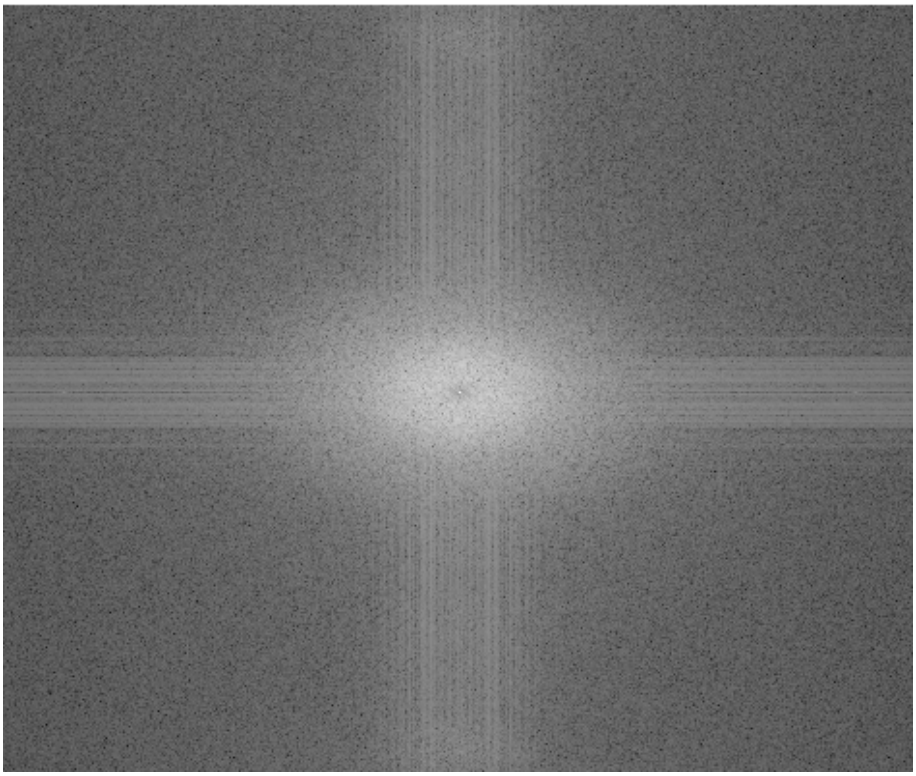

Figure 6.7. Two-dimensional Fourier transformation of top view of ZnO nanotips grown on s GZO/GaN template (shown in figure 6.3).

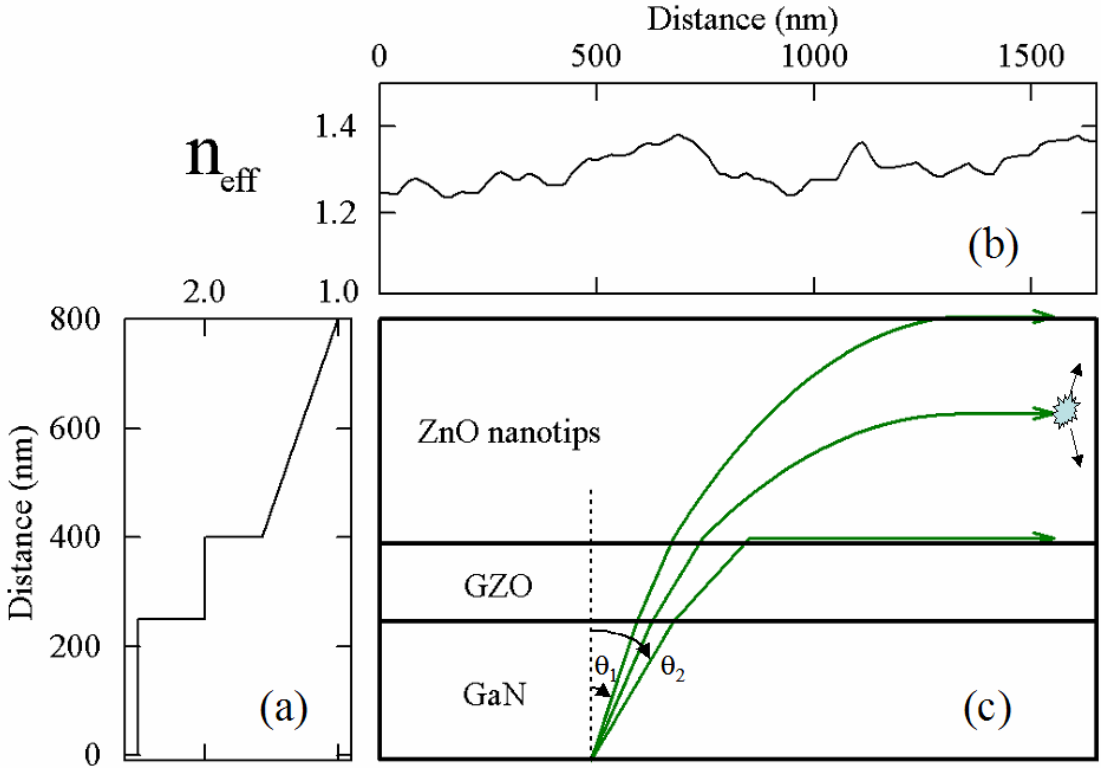

Figure 6.8. (a) Effective refractive index for ZnO nanotips/GZO/GaN LED structure, assuming a uniformly distributed nanotip layer; (b) illustration of the variation of effective refractive index in a randomly distributed ZnO nanotips layer 50nm away from the interface; (c) photon trajectories in a ZnO nanotips structure. Light extraction is enhanced by surface roughening (not shown) and scattering events caused by non-uniform dielectric.

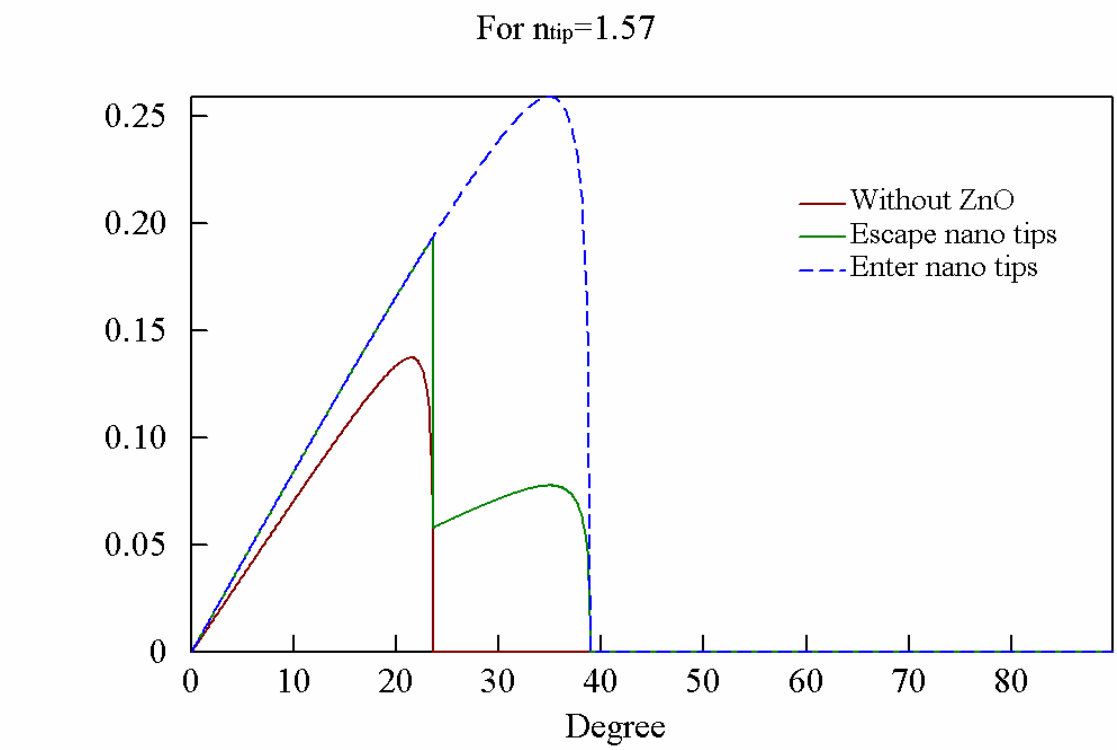

Figure 6.9. Simulated angular distribution of transmitted light with ZnO nanotips on top of GaN. For comparison, optical transmission of a standard GaN layer without top ZnO nanotips layer is also shown in red curve.

Chapter 7. Conclusions and Future Work

7.1 Conclusions

Single crystalline ZnO nanotips can be grown by MOCVD on various substrates (Si, GaN, etc) at relatively low deposition temperature, giving it a unique advantage over many other semiconductor nanostructures, such as carbon nanotubes, GaN and SiC nanowires. These ZnO nanotips possess superior optical properties with free excitonic emission at room temperature. It is compatible with the existing semiconductor processing technology. This forms a solid basis for ZnO nanotips based device integration, such as with Si based mainstream microelectronics, and with GaN based mainstream UV/blue optoelectronics.

In this dissertation work, *in-situ* n-type doping of ZnO nanotips during MOCVD is studied, including the doping effects on optical properties and electrical conductivity. Current-voltage characteristics of the ZnO nanotips show the conductivity enhancement due to Ga doping at the proper doping concentration. At low or moderate doping levels, the increase in PL intensity from Ga doping has been attributed to the increase of Ga donor related impurity emission. Nonradiative recombination channels dominate at very heavily Ga doping, leading to PL quenching.

The details of excitonic emissions of ZnO nanotips are investigated using temperature-dependent PL spectroscopy. Sharp free exciton and donor-bound exciton peaks are observed at 4.4K with photon energies of 3.380, 3.369, and 3.364 eV, confirming high optical quality of ZnO nanotips. Free exciton emission dominates at temperatures above 50K. The thermal dissociation of these bound excitons forms free excitons and neutral donors. Temperature-dependent free A exciton peak emission is

fitted to the Varshni's equation to study the variation of energy bandgap versus temperature. Time resolved PL spectrum shows a biexponential decay profile, suggesting that two different carrier capture mechanisms dominate the carrier recombination process.

A prototype of hybrid ZnO nanotips/GaN light emitting devices has been demonstrated using an n-ZnO nanotips/p-GaN heterostructure. p-n junction is formed between ZnO nanotips and p-GaN. The p-n diode has a turn-on voltage of 3V, and a breakdown voltage of ~ 8V. The forward current at 5V is 2.5 mA, and the reverse leakage current at –5V is 54 μA. The electroluminescence with a peak wavelength of 406nm is primarily due to radiative recombination from electron injection into p-type GaN.

An integrated ZnO nanotips/GaN LED has been demonstrated for enhanced light emission efficiency. A Ga-doped ZnO transparent conductive oxide (GZO) film and ZnO nanotips are directly grown on top of a GaN LED, serving as transparent electrode and light extraction layer, respectively. Compared with the conventional Ni/Au p-metal LED, light output power from the ZnO nanotips/GZO/GaN LED is improved by 1.7 times. The enhanced light extraction is attributed to increased light scattering and transmission in the ZnO/GaN multilayer.

7.2 Suggestions for Future Work

Even with extensive research effort on ZnO based devices in recent years, this field is still in the early stage of development. In order to understand various physical mechanisms behind therefore to provide guideline for improving device performance and extending their applications, the following work is recommended for the future research and development of novel ZnO nanotips devices based on the present progress:

1. For the Ga-doped ZnO nanotips, the proper characterizations of the carrier concentration and mobility in the nanoscale geometry are necessary. This information will be helpful to improve the understanding of observed conductivity enhancement and PL signal changes in the Ga-doped ZnO nanotips, which is particularly useful to design the devices. In addition, the current transportation mechanism in the doped-ZnO nanotips will also be studied.
2. For the hybrid n-ZnO nanotips/p-GaN heterojunction devices, only initial feasibility work has been tried. A reliable processing technology, including dielectric fill-in and isolation followed by planarization, needs to be developed for these vertical nano-devices. Advanced gas-phase fill-in technology is preferred to fabricate the ZnO nanotips based junction devices. The growth technology also needs to be improved to achieve higher internal quantum efficiency of ZnO nanotips for optical device applications.
3. The advanced solid state lighting technology needs even higher light extraction efficiency (~ 90%). In such a case, the nano-scale surface roughness treatment may be insufficient. The promising way is to design of the low cost photonic crystal (PC) in conjunction with the nano-scale surface treatment using ZnO nanotips to further enhance the external quantum efficiency of a GaN LED. Important parameters for ZnO nanotips may include the fill-in factor and graded effective refractive index. The critical issue to be studied includes artificially index matching with GaN, to minimize the reflection at the interface.
4. The energy band alignment needs to be calculated with the piezoelectric and spontaneous polarization induced interface charges for the c-axis oriented GaN

and ZnO nanotips. Understanding of strain/stress relaxation in columnar structure ZnO nanotips will be helpful to calculate the piezoelectric polarization effect at the interface. In such a band alignment, localized well will be formed for electrons and holes at the polar ZnO/GaN interface, leading to a higher carrier density at the interface for the Type-II band alignment with polarization charge. It effects on the ZnO nanotips-based optical device performance need to be studied.

References

1. C. W. Bunn, Proc. Phys. Soc. London, **47**, 835 (1935).

2. E. Mollwo, Z. Angew. Phys. **6**, 257 (1954).

3. D. C. Reynolds and T. C. Collins, Phys. Rev. **185**, 1099 (1969).

4. D. C. Look, Mater. Sci. Eng. B **80**, 381 (2001).

5. J. D. Albrecht, P.P.R., S. Limpijumnong, W. R. L. Lambrecht, K. F. Brennan, J. Appl. Phys. **86** (1999).

6. Y. Liu, C. R.Gorla., S. Liang, N. Emanetoglu, Y. Lu, H. Shen, and M. Wraback, J. Electron. Mater. **29**, 69(2000).

7. S. Liang, H. Sheng., Y. Liu, Z. Huo, Y. Lu, and H. Shen, J. Crys. Growth. **225**, 110(2001).

8. H. C. Liu, M. Gao, J. McCaffrey, Z. R. Wasilewski, and S. Fafard, Appl. Phys. Lett. **78**, 79 (2001).

9. A. K. Sharma, S. H. Zaidi, G. Liecthy, S. R. Brueck, Proceedings 1st IEEE Conference on Nanotechnology (IEEE-NANO'2001), pp. 368-373, Piscataway, NJ, USA.

10. B. Gil and A. V. Kavokin, Appl. Phys. Lett. **81** (4), 748 (2002).

11. E. M. Wong and P. C. Searson, Appl. Phys. Lett. **74**, 2939 (1999).

12. R. T. Senger and K. K. Bajaj, Phys. Rev. B **68**, 045313 (2003).

13. A. Ohtomo, M. Kawasaki, I. Ohkubo, H. Koinuma, T. Yasuda, and Y. Segawa, Appl. Phys. Lett. **75** (7), 980 (1999).

14. W. I. Park, G. Yi, M. Kim, and S. J. Pennycook, Adv. Mater. **15** (6), 526 (2003).

15. K. Maejima, M. Ueda, S. Fujita, and S. Fujita, Jpn. J. Appl. Phys. Part.1, **42** (5A), p. 2600-2604.

16. M. Zamfirescu, A. K., B. Gil, G. Malpuech, and M. Kaliteevski, Phys. Rev. B. **65**, 161205(2002).

17. V. A. L. Roy, A. B. Djurisic, W. K. Chan, J. Gao, H. F. Lui, and C. Surya, Appl. Phys. Lett. **83**(1), 141 (2003).

18. Y. B. Li, Y. Bando, T. Sato, and K. Kurashima, Appl. Phys. Lett. **81**(1), 144 (2002).

19. Z. W. Pan, Z. R. Dai, and Z. W. Wang, Science **291**, 1947 (2001).

20. S. Muthukumar, H. Sheng, J. Zhong, Z. Zhang, N. W. Emanaetoglu, Y. Lu, IEEE Trans. Nanotech 2 (1), 50(2003).

21. J. Zhong, G. Saraf, S. Muthukumar, H. Chen, Y. Chen, and Y. Lu, TMS & IEEE J. Electron. Mater. **33** (6), 654 (2004).

22. M. Yan, H. T. Zhang, E. J. Widjaja, and R. P. H. Chang, J. of Appl. Phys. **94** (8), 5240 (2003).

23. J. Park, H. Choi, K. Siebein and R. K. Singh, J. of Crys. Growth, **258** (3-4), 342 (2003).

24. Y. W. Heo, V. Varadarajan, M. Kaufman, K. Kim, and D. P. Norton, F. Ren, P. H. Fleming, Appl. Phys. Lett. **81**(16), 3046 (2002).

25. M. Haupt, A. Ladenburger, R. Sauer, K. Thonke, R. Glass, W. Roos, J. P. Spatz, H. Rauscher, S. Riethmüller, and M. Möller, J. Appl. Phys. **93** (10), 6252 (2003).

26. S. C. Lyu, Y. Zhang, H. Ruh, H. Lee, H. Shim, E. Suh, and C. J. Lee, Chem. Phys. Lett. **363**, 134(2002).

27. Y. Li, G. W. Meng, L. D. Zhang, and F. Phillipp, Appl. Phys. Lett. **76**(15), 2011 (2000).

28. Lion Vayssieres, Adv. Mater. **15**(5), 464 (2003).

29. Lion Vayssieres, N. Beermann, S. E. Lindquist, and A. Hagfeldt, Chem. Mater. **13**, 233 (2001).

30. K. Govender, D. S. Boyle, P. O'Brien, D. Binks, D. West, and D. Coleman, Adv. Mater. **14** (17), 1221 (2002).

31. J. P. Suchet, Chemical Physics of Semiconductors, Van Nostrand, New York, 1965.

32. Y. Wang, L. Zhang, C. Liang, G. Wang and X. Peng, Chem. Phys. Lett. **357**(3-4), 314 (2002).

33. X. Duan and C. M. Lieber, Adv. Mater. **12**(4), 298 (2000).

34. F. C. Frank, Discovery Faraday Soc. 1949, **5**, 48.

35. C. M. Drum and J. W. Mitchell, Appl. Phys. Lett. **4** (9), 164 (1964).

36. J. Wu and S. Liu, J. Phys. Chem. B **106**, 9546 (2002).

37. Y. Xia, P. Yang, Y. Sun, Y. Wu, B. Mayers, B. Gates, Y. Yin, F. Kim and H. Yan, Adv. Mater. **15**(5), 353 (2003).

38. W. J. Li, E. W. Shi, W. Z. Zhong and Z. W. Yen, J. of Crys. Growth **203**(1-2), 186 (1999).

39. Y. Dai, Y. Zhang, Q. K. Li and C. W. Nan, Chem. Phys. Lett. **358**(1-2), 83 (2002).

40. Z. W. Pan, Z. R. Dai, and Z. W. Wang, Science **291**, 1947 (2001).

41. Y. Zhang, H. Jia, X. Luo, X. Chen, D. Yu, and R. Wang, J. Phys. Chem. B **107** (33), 8289 (2003).

42. M. H. Huang, S. Mao, H. Feick, H. Yan, Y. Wu, H. Kind, E. Weber, R. Russo, P. Yang, Science, **292** (5523), 1897 (2001).

43. M. H. Huang, Y. Wu, H. Feick, N. Tran, E. Weber, and P. Yang, Adv. Mater. **13** (2), 113 (2001).

44. P. Yang, H. Yan, S. Mao, R. Russo, J. Johnson, R. Saykally, N. Morris, J. Pham, R. He, H. J. Choi, Adv. Func. Mater. **12**(5), 323 (2002).

45. Z. W. Pan, Z. R. Dai, and Z. W. Wang, Science **291**, 1947(2001).

46. B. D. Yao, Y. F. Chan, and N. Wang, Appl. Phys. Lett. **81**(4), 757 (2002).

47. J. G. Wen, J. Y. Lao, D. Z. Wang, T. M. Kyaw, Y. L. Foo, and Z. F. Ren, Chem. Phys. Lett. **372**, 717 (2003).

48. Y. C. Kong, D. P. Yu, B. Zhang, W. Fang, and S. Q. Feng, Appl. Phys. Lett. **78**(4), 407 (2001).

49. W. I. Park, D. H. Kim, S. W. Jung, and G. Yi, Appl. Phys. Lett. **80** (22), 4232 (2002).

50. U. Rössler, Physical Review **184**, 733 (1969).

51. Manuel Cardona and F. H. Pollak J. E. Rowe, Solid State Communications, **6**(4), 239 (1968).

52. G. F. Koster, J. O. Dimmock, R. G. Wheeler, and H. Statz, *Properties of thirty-two point groups*, Cambridge, USA: MIT Press, 1963.

53. A. Mang, K. Reimann, St. Rübenacke, Solid State Communication **94** (4), 251

(1995).

54. B. K. Meyer, H. Alves, D. M. Hofmann, W. Kriegseis, D. Forster, F. Bertram, J. Christen, A. Hoffmann, M. Strapburg, M. Dworzak, U. Haboeck, and A. V. Rodina, Phys. Stat. Sol. (b), **241** (2), 231 (2004).

55. D. G. Thomas, J. Phys. Chem. Solids **15**, 86 (1960).

56. Y. S. Park, C. W. Litton, T. C. Collins, D. C. Reynolds, Phys. Rev. **143**(2), Mar. 1966.

57. D. C. Reynolds, D. C. Look, B. Jogai, C. W. Litton, G. Cantwell, W. C. Harsch, Phys. Rev. **60** (4), 15 July 1999.

58. W. R. L. Lambrecht, A. V. Rodina, S. Limpijumnong, B. Segall, B. K. Meyer, Phys. Rev. B **65**, 075207, 2002.

59. H. Yoshikawa, S. Adachi, Jpn. J. Appl. Phys. **36** (10), part 1, 6237 (1997).

60. J. Wrzesinski, D. Fröhlich, J. Crystal Growth **184/185**, 686 (1998).

61. R. L. Weiher and W. C. Tait, Phys. Rev. **183**(3), 1114 (1969).

62. Lijun Wang and N. C. Giles, J. Appl. Phys. **94**(2), 973 (2003).

63. D. C. Reynolds, D. C. Look, B. Jogai, J. E. Hoelscher, R. E. Sherriff, M. T. Harris and M. J. Callahan, J. Appl. Phys. **88**(4), 2152 (2000).

64. U. Ozgur, Ya. I. Alivov, C. Liu, A. Teke, M. A. Reshchikov, S. Dogan, V. Avrutin, S. J. Cho, and H. Morkoc, J. Appl. Phys. **98**, 041301 (2005).

65. R. E. Sherriff, D. C. Reynolds, D. C. Look, B. Jogai, J. E. Hoelscher, T. C. Collins, G. Cantwell and W. C. Harsch, J. Appl. Phys. **88**(6), 3454 (2000).

66. S. F. Chichibu, T. Sota, G. Cantwell, D. B. Eason and C. W. Litton, J. Appl. Phys. **93**(1), 756 (2003).

67. C. F. Klingshirn, *Semiconductor Optics*, Springer, 1997.

68. A. Teke, U. Ozgur, S. Dogan, X. Gu, H. Morkoc, B. Nemeth, J. Nause, and H. O. Everitt, Phys. Rev. B **70**, 195207 (2004).

69. H. D. Sun, T. Makino, Y. Segawa, A. Ohtomo, R. Shiroki, K. Tamura, T. Tamura, and H. Koinuma, J. Appl. Phys. **91**, 1993 (2002).

70. Lijun Wang and N. C. Giles, Appl. Phys. Lett. **84**(16), 3049 (2004).

71. G. Martinez-Criado, C. R. Miskys, A. Cros, O. Ambacher, A. Cantarero, and M. Stutzmann, J. Appl. Phys. **90**(11), 5627 (2001).

72. M. Leroux, N. Grandiean, B. Beaumont, G. Nataf, F. Semond, J. Massies, and P. Gibart, J. Appl. Phys. **86**(7), 3721 (1999).

73. A. Tsukazaki, A. Ohtomo, M. Kawasaki, T. Makino, C. H. Chia, Y. Segawa and H. Koinuma, Appl. Phys. Lett. **84**(19), 3858 (2004).

74. T. Makino, K. Tamura, C. H. Chia, Y. Segawa, M. Kawasaki, A. Ohtomo, H. Koinuma, Appl. Phys. Lett. **81**(12), 2172 (2002).

75. Aishi Yamamoto, Kensuke Miyajima, Takenari Goto, Hang Ju Ko and Takafumi Yao, J. Appl. Phys. **90**(10), 4973 (2001).

76. M. Watanabe, M. Sakai, H. Shibata, H. Tampo, P. Fons, K. Iwata, A. Yamada, K. Matsubara, K. Sakurai, S. Ishizuka, S. Niki, K. Nakahara and H. Takasu, Appl. Phys. Lett. **86**, 221907 (2005).

77. N. Y. Garces, Lijun Wang, N. C. Giles, L. E. Hallibutton, G. Cantwell, and D. B. Eason, J. Appl. Phys. **94** (1), 519 (2003).

78. K. Thonke, Th. Gruber, N. Teofilov, R. Schonfeld, A. Waag, and R. Sauer, Physica B **308-310**, 945 (2001).

79. G. Xiong, K. B. Ucer, R. T. Williams, J. Lee, D.Bhattacharyya, J. Metson and P. Evans, J. Appl. Phys. **97**, 043528 (2005).

80. Q. X. Zhao, M. Willander, R. E. Morjan, Q-H. Hu and E. E. B. Campbell, Appl. Phys. Lett. **83**(1), 165 (2003).

81. B. K. Meyer, J. Sann, D. M. Hofmann, C. Neumann, and A. Zeuner, Semicond. Sci. Technol. **20**, S62-65 (2005).

82. F. Reuss, C. Kirchner, Th. Gruber, R. Kling, S. Maschek, W. Limmer, A. Waag, and P. Ziemann, J. Appl. Phys. **95** (7), 3385 (2004).

83. T. Makino, K. Tamura, C. H. Chia, Y. Segawa, M. Kawasaki, A. Ohtomo, and H. Koinuma, J. Appl. Phys. **92** (12), 7157 (2002).

84. W. I. Park, Y. H. Jun, S. W. Jung and Gyu-Chul Yi, Appl. Phys. Lett. **82** (6), 964 (2003).

85. Bing Guo, Z. R. Qiu, and K. S. Wong, Appl. Phys. Lett. **82** (14), 2290 (2003).

86. B. P. Zhang, N. T. Binh, Y. Segawa, Y. Kashiwaba and K. Haga, Appl. Phys. Lett. **84**(4), 586 (2004).

87. B. P. Zhang, N. T. Binh, Y. Segawa, K. Wakatsuki and N. Usami, Appl. Phys. Lett. **83**(8), 1635 (2003).

88. Y. Gu, I. L. Kuskovsky, M. Yin, S. O'Brien, and G. F. Neumark, Appl. Phys. Lett. **85**, 3833 (2004).

89. M. H. Huang, S. Mao, H. Feick, H. Yan, Y. Wu, H. Kind, E. Weber, R. Russo, P. Yang, Science, **292**(5523), 1897 (2001).

90. H. Yan, R. He, J. Johnson, M. Law, R. J. Saykally, and P. Yang, J. Am. Chem. Soc. **125** (16), 4728 (2003).

91. J. C. Johnson, H. Yan, R. D. Schaller, L. H. Haber, R. J. Saykally, and P. Yang, J. Phys. Chem. B **105** (46), 11387 (2001).

92. S. F. Yu, C. Yuen, S. P. Lau, W. I. Park, and G. Yi, Appl. Phys. Lett. **84** (17), 3241 (2004).

93. D. M. Bagnall, Y. F. Chen, Z. Zhu, T. Yao, S. Koyama, M. Y. Shen, and T. Goto, Appl. Phys. Lett. **70** (17), 2230 (1997).

94. J. C. Johnson, H. Yan, R. D. Schaller, L. H. Haber, R. J. Saykally, and P. Yang, The Journal of Physical Chemistry B **105** (46), 2001, 11387-11390.

95. K. Keem, H. Kim, G. Kim, J. S. Lee, B. Min, K. Cho, M. Sung, and S. Kim, Appl. Phys. Lett. **84** (22), 4376 (2004).

96. Y. W. Heo, L. C. Tien, D. P. Norton, S. J. Pearton, B. S. Kang, F. Ren, and J. R. LaRoche, Appl. Phys. Lett. **85** (15), 3107 (2004).

97. S. E. Ahnm J. S. Lee, H. Kim, S. Kim, B. H. Kang, K. H. Kim, and G. T. Kim, Appl. Phys. Lett. **84** (24), 5022 (2004).

98. H. Kind, H. Yan, B. Messer, M. Law, and P. Yang, Adv. Mater. **14** (2), 158-160 (2002).

99. Z. Fan, P. Chang, J. G. Lu, E. C. Walter, R. M. Penner, C. Lin, and H. P. Lee, Appl. Phys. Lett. **85**, 6128 (2004).

100. R. Konenkamp, R. C. Word, and C. Schlegel, Appl. Phys. Lett. **85**, 6004 (2004).

101. H. Y. Ng, J. Han, T. Yamada, P. Nguyen, Y. P. Chen, and M. Meyyappan, Nano Lett. **4** (7), 1247 (2004).

102. Ya. I. Alivov, J. E. Van Nostrand, D. C. Look, M. V. Chukichev, and B. M. Ataev, Appl. Phys. Lett. **83** (14), 2943 (2003).

103. Ya. I. Alivov, E. V. Kalinina, A. E. Cherenkov, D. C. Look, B. M. Ataev, A. K. Omaev, M. V. Chukichev, and D. M. Bagnall, Appl. Phys. Lett. **83** (23), 4719 (2003).

104. C. H. Park, I. S. Jeong, J. H. Kim, and S. Im, Appl. Phys. Lett. **82** (22), 3973 (2004).

105. D. C. Look, J. W. Hemsky, and J. R. Sizelove, Phys. Rev. Lett. **82**, 2552 (1999).

106. C. G. Van de Walle, Phys. Rev. Lett. **85**, 1012 (2000).

107. S. F. J. Cox et al., Phys. Rev. Lett. **86**, 2601 (2001).

108. V. A. Nikitenko, J. Appl. Spectrosc. **57**, 783 (1993).

109. H. J. Ko, Y. F. Chen, T. Yao, K. Miyajima, A.Yamamoto, and T. Goto, Appl. Phys. Lett. **77**, 537 (2000).

110. B. E. Sernelius, K. F. Berggren, Z.C. Jin, I. Hamberg, and C.G. Granqvist, Phys. Rev. B **37**, 10244 (1988).

111. T. Makino, Y. Segawa, S. Yoshida, A. Tsukazaki, A. Ohtomo, and M. Kawasaki, Appl. Phys. Lett. **85**, 759 (2004).

112. J. Grabowska, A. Meaney, K. K. Nanda, J. P. Mosnier, M. O. Henry, J. R. Duclere, and E. McGlynn, Phys. Rev. B **71**, 115439 (2005).

113. D. C. Reynolds, D. C. Look, B. Jogai, C. W. Litton, T. C. Collins, W. Harsch, and G. Cantwell, Phys. Rev. B **57**, 12151 (1998).

114. Y. Chen, H, J. Ko, S, K. Hong, and T. Yao, Appl. Phys. Lett. **76**, 559 (2000).

115. A. R. Huston, J. Phys. Chem. Solids 1959, **8,** 467.

116. Gyu-Chul Yi, Won I1 Park, Sug Woo Jung, Sangsu Hong, and Taiha Joo, Proceeding of SPIE, **4992**, 75 (2003).

117. T. Detchprohm, K. Hiramatsu, H. Amano, I. Akasaki, Appl. Phys. Lett. **61** (22), 2688 (1992).

118. W. Götz, L.T. Romano, J. Walker, N.M. Johnson, R.J. Molnar, Appl. Phys. Lett. **72** (10), 1214 (1998).

119. S. Gu, R. Zhang, J. Sun, L. Zhang, T.F. Kuech, Appl. Phys. Lett., **76** (23), 3454 (2000).

120. R.D. Vispute, V. Talyansky, S. Choopun, R.P. Sharma, T. Venkatesan, M. He, X. Tang, J.B. Halpern, M.G. Spencer, Y.X. Li L.G. Salamanca-Riba, A.A. Iliadis, K. A. Jones, Appl. Phys. Lett. 73 (3), 348 (1998).

121. H.J. Ko, Y.F. Chen, S.K. Hong, H. Wenisch, T. Yao, D.C. Look, Appl. Phys. Lett. **77** (23), 3761 (2000).

122. S.-K. Hong, T. Hanada, H.-J. Ko, Y. Chen, T. Yao, D. Imai, K. Araki, M. Shinohara, Appl. Phys. Lett. **77** (22), 3571 (2000).

123. J.O. Song, K.-K. Kim, S.-J. Park, T.-Y. Seong, Appl. Phys. Lett. **83** (3), 479 (2003).

124. M. Quik, J. Serda, *Semiconductor Manufacturing Technology*, Prentice-Hall, Inc., Upper Saddle River, New Jersey (2001)

125. A. Guillén-Santiago, M. de la L. Olvera, A. Maldonado, R. Asomoza, and D. R. Acosta, Phys. Stat. Sol. 201, 5, 952 (2004)

126. H. Sheng, N. W. Emanetoglu, S. Muthukumar, Y. Lu, J. Electronic Materials, **31** (7), 811 (2002).

127. S.M. Sze, *Physics of Semiconductor Devices*, 2nd Edition, John Wiley & Sons, Inc., New York (1981).

128. J. A. Aranovich, D. G. Golmayo, A. L. Fahrenbruch, and R. H. Bube, J. Appl. Phys. **51**, 4260 (1980).

129. Ho Won Jang, Soo Young Kim, and Jong-Lam Lee, J. Appl. Phys. **94** (3), 1748 (2003).

130. Ja-Soon Jang, Seong-Ju Park, and Tae-Yeon Seong, J. Vac. Sci. Technol. B **17** (6), 2667, Nov/Dec 1999.

131. J.A. Edmond, K. Das, and R. F. Davis, J. Appl. Phys. **63**, 922 (1988).

132. Ya. I. Alivov, U. Ozgur, S. Dogan, D. Johnstone, V. Avrutin, N. Onojima, C. Liu, J. Xie,Q. Fan, and H. Morkoc, Appl. Phys. Lett. **86**, 241108 (2005).

133. T. Fujii, Y. Gao, R. Sharma, E. L. Hu, S. P. DenBaars, and S. Nakamura, Appl. Phys. Lett. **84**, 855 (2004).

134. T. N. Oder, K. H. Kim, J. Y. Lin, and H. X. Jiang, Appl. Phys. Lett. **84**, 466 (2004).

135.E. F. Schubert, Y. H. Wang, A. Y. Cho, L. W. Tu, and G. J. Zydzik, Appl. Phys. Lett. **60**, 921 (1992).

136.W. L. Barnes, J. Lightwave Technol. **17**, 2170 (1999).

137.B. J. Matterson, J. M. Lupton, A. F. Safonov, M. G. Salt, W. L. Barnes, and I. D. W. Samul, Adv. Mater. **13**, 123 (2001).

138.H. J. Peng, Y. L. Ho, X. J. Xu, and H. S. Kwok, J. Appl. Phys. **96** (3), 1649 (2004).

139.I. Schnitzer, E. Yablonovitch, C. Caneau, T. J. Gmitter, and A. Scherer, Appl. Phys. Lett. **63**, 2174 (1993).

140.R. Windisch, C. Rooman, S. Meinlschmidt, P. Kiesel, D. Zipperer, G. H. Döhler, B. Dutta, M. Kuijk, G. Borghs, and P. Heremans, Appl. Phys. Lett. **79**, 2315 (2001).

141.Y. Ono, Y. Kimura, Y. Ohta, and N. Nishida, Appl. Optics **26** (6), 1142 (1987).

142.M. Nieto-Vesperinas and J. A. Sánchez-Gil, J. Opt. Soc. Am. A **9** (3), 424 (1992).

143.Private communication with Dr. H. Shen.

144.J.N. Mait, D.W. Prather, and M.K. Mirotznik, Optics Lett. **23** (17), 1343 (1998).

Curriculum Vita

Jian Zhong

Education

July 1992	Bachelor of Science in Electronic Engineering Tsinghua University, Beijing, China
July 1995	Master of Science in Electronic Engineering Tsinghua University, Beijing, China
October 2007	Doctor of Philosophy in Electrical and Computer Engineering, Rutgers University, New Brunswick, New Jersey

Related Publications

Journals

1. "Growth and Structural Analysis of Metalorganic Chemical Vapor Deposited $(11\bar{2}0)$ $Mg_xZn_{1-x}O$ ($0<x<0.33$) Films on $(01\bar{1}2)$ R-plane Al_2O_3 Substrates", S. Muthukumar, J. Zhong, Y. Chen, Y. Lu, T. Siegrist, *Applied Physics Letters*, vol. 82, no.5, pp.742-744, Feb. 2003.
2. "Selective MOCVD Growth of ZnO Nanotips", S. Muthukumar, H. Sheng, J. Zhong, Z. Zhang, N. W. Emanaetoglu, Y. Lu, *IEEE Trans. Nanotech*, vol.2, n.1, pp.50-54, 2003.
3. "Ga-doped ZnO Single-crystal Nanotips Grown on Fused Silica by Metalorganic Chemical Vapor Deposition", J. Zhong, S. Muthukumar, Y. Chen, Y. Lu, H. M. Ng, W. Jiang and E. L. Garfunkel, *Applied Physics Letters*, 83 (16), pp. 3401-3403, 2003.
4. "ZnO Nanotips Grown on Silicon Substrates by Metalorganic Chemical Vapor Deposition", J. Zhong, G. Saraf, S. Muthukumar, H. Chen, Y. Chen, and Y. Lu. *TMS & IEEE Journal of Electronic Materials*, vol.33, no.6, pp.654-657, June 2004.
5. "Metalorganic Chemical Vapor Deposition and Characterizations of Epitaxial $Mg_xZn_{1-x}O$ ($0\leq x \leq 0.33$) Films on r-sapphire Substrates", S. Muthukumar, Y. Chen, J. Zhong, F. Cosandey, Y. Lu, T. Siegrist, *Journal of Crystal Growth*, **261** (2004), pp. 316-323.
6. "Li Diffusion on Epitaxial (112-0) ZnO Film on r-sapphire", P. Wu, J. Zhong, N. W. Emanetoglu, S. Muthukumar, Y. Chen, Y. Lu. *TMS & IEEE Journal of Electronics Materials*, 33 (6), pp. 596-599, June, 2004.
7. "Surface Acoustic Wave Ultraviolet Photodetectors Using Epitaxial ZnO Multilayers Grown on r-plane Sapphire", Nuri W. Emanetoglu, Jun Zhu, Ying Chen, Jian Zhong, Yimin Chen, and Y. Lu, *Applied Physics Letters,* 85, 3702, 2004.
8. "DNA Immobilization and SAW Response in ZnO Nanotips Grown on $LiNbO_3$ Substrates"**,** Z. Zhang, N. W. Emanetoglu, G. Saraf, Y. Chen, P. Wu, J. Zhong and Y. Lu, J. Chen, O. Mirochnitchenko, M. Inouye, *IEEE Trans. on Ultrasonics,*

ferroelectrics and frequency control, 2005.

9. "Interface Properties of ZnO Nanotips Grown on Si Substrates", H. Chen, J. Zhong, G. Saraf, Y. Lu, D.H. Hill, S. T. Hsu, and Y. Ono, *TMS & IEEE Journal of Electronic Materials,* vol. 35, No. 6, pp.1241-1245, 2006.
10. "$SiCl_4$-based Reactive Ion Etching of $Mg_xZn_{1-x}O$ and ZnO", J. Zhu, H. F. Sheng, G. Saraf, J. Zhong, and Y. Lu, *TMS & IEEE Journal of Electrical Material*, vol. 35, No. 6, 2006.
11. "Structural and Optical Properties of ZnO Nanotips Grown on GaN Using Metalorganic Chemical Vapor Deposition", Jian Zhong, Gaurav Saraf, Hanhong Chen, Yicheng Lu, Hock M. Ng, Theo Siegrist, A. Parekh, D. Lee, and Eric A. Armour, *JEM web Published online*, May 2007.
12. "Fast and Reversible Wettability Transitions on ZnO Nanostructures", Z. Zhang, H. Chen, J. Zhong, G. Saraf and Y. Lu, *JEM web Published online*, 10 May 2007.
13. "Surface and Interface Properties of MOCVD Grown a-plane $Mg_xZn_{1-x}O$ ($0 <= x <= 0.3$) films", G. Saraf, J. Zhong, O. Dulub, U. Diebold, T. Siegrist and Y. Lu, to appear in *Journal of Electronic Materials*, 2007.
14. "Integrated ZnO Nanotips on GaN Light Emitting Diodes for Enhanced Emission Efficiency", J. Zhong, H. Chen, G. Saraf, Y. Lu, C.K. Choi, J.J. Song, D.M. Mackie, and H. Shen, *Applied Physics Letters,* 90, 203515 (2007).

Conference Proceedings and Presentations:

1. "In-plane Optical Anisotropy of $Mg_xZn_{1-x}O$ Films Grown on R-plane Sapphire by MOCVD", J. Zhong, S. Muthukumar, Y. Chen, Y. Lu, *The 2002 U.S. Workshop on the Physics and Chemistry of II-VI Materials*, San Diego, CA, Nov.13-15, 2002.
2. "Properties of ZnO Nanotips Selectively Grown by MOCVD", Hanhong Chen, Jian Zhong, Gaurav Saraf, Zheng Zhang, Yicheng Lu, Linus A. Fetter, Chien S. Pai, Pro*ceedings of SPIE*, Volume: 5592-31, 2005.
3. "Structural and Optical Properties of ZnO Nanotips Grown on GaN", J. Zhong, G. Saraf, H. Chen, Y. Lu, H. M. Ng, T. Siegrist, A. Parekh, D. Lee, E. A. Armour, Proceeding of *47th Electronic Materials Conference*, 3, p.34, 8, June 22 - 24, 2005, Santa Barbara, CA
4. "Photoluminescence and Electroluminescence Properties of ZnO Nanotips Grown on p-type GaN", J. Zhong, H. Chen, G. Saraf, Y. Lu, H. M. Ng, C. K. Choi, and J. J. Song, Proceeding *of 48th TMS Electronic Materials Conference*, p.89, Pennsylvania State University, University Park, PA, June 28-30, 2006.
5. "Surface and Interface Characterization of a-plane ZnO and $Mg_xZn_{1-x}O$ Films", Gaurav Saraf, Jian Zhong, Yicheng Lu, Olga Dulub, Ulrike Diebold, and Theo Siegrist, Proceeding *of 48th TMS Electronic Materials Conference*, p.71, Pennsylvania State University, University Park, PA, June 28-30, 2006.
6. "The Fast and Reversible Wettability Transitions of ZnO Nanostructures", Z. Zhang,

H. Chen, J. Zhong, Y. Lu, S. Rivillon, Y. J. Chabal, A. Nuber, T. Madey, *II-VI Workshop*, Newport Beach, California, Oct.10-12, 2006.

7. "ZnO Nanotip-based QCM Biosensors", Zheng Zhang, Hanhong Chen, Jian Zhong, Ying Chen, Yicheng Lu, *Proceeding of IEEE UFFC Frequency Control,* Miami, Florida, Jun. 2006
8. "Integrated ZnO Nanotips on GaN Light Emitting Diodes for Enhanced Emission Efficiency", J. Zhong, H. Chen, G. Saraf, C. K. Choi, J. J. Song, D. M. Mackie, and H. Shen, Proceeding *of 49th TMS Electronic Materials Conference*, p.70-71, University of Notre Dame, Notre Dame, IN, Jun. 20-22, 2007.

Book Chapter:

"ZnO-based Nanostructures", Y. Lu and J. Zhong, Chapter 6, *Semiconductor Nanostructures* (editor S. Todd), *Artech House* (2004).

Patents:

"Fabrication of Ag Schottky Contacts on $(11\bar{2}0)$ $Mg_xZn_{1-x}O$", Y. Lu, H. F. Sheng, S. Muthukumar, N. W. Emanetoglu, and J. Zhong, U.S. Patent No. 11,042,533. (July 7, 2005).

"Novel ZnO Nanostructure-based Light Emitting Diodes", Y. Lu and J. Zhong (pending).